

University of Alberta

Numerical study of ionospheric response to perturbations and interaction
with spacecraft instruments

by

Nadia Imtiaz

A thesis submitted to the Faculty of Graduate Studies and Research
in partial fulfillment of the requirements for the degree of

Doctor of Philosophy

Department of Physics

© Nadia Imtiaz
Spring 2014
Edmonton, Alberta

Permission is hereby granted to the University of Alberta Libraries to reproduce single copies of this thesis and to lend or sell such copies for private, scholarly or scientific research purposes only. Where the thesis is converted to, or otherwise made available in digital form, the University of Alberta will advise potential users of the thesis of these terms.

The author reserves all other publication and other rights in association with the copyright in the thesis and, except as herein before provided, neither the thesis nor any substantial portion thereof may be printed or otherwise reproduced in any material form whatsoever without the authors prior written permission.

“To my Daughter, Daniya”

Abstract

This PhD thesis presents numerical studies of the ionosphere dynamics and of the interaction between ionospheric plasma and spacecraft instruments. The main results of my research are the following: A first study presents a simple model to account for magnetic field perturbations in response to geophysical phenomena such as earthquakes. Following an earthquake, large neutral density and velocity perturbations reach altitudes of 150 – 350 km, where significant coupling between the neutral atmosphere and the ionosphere occurs. Photoionization and collisional friction between plasma and the neutral exosphere then results in a rapid variation in ionospheric plasma parameters. This in turn leads to the generation of two types of waves: shear Alfvén and the compressional modes. Variations in the total electron content (TEC) are also computed for the ion acoustic mode and the compressional mode by considering density perturbations along and transverse to the magnetic field. The second part of my work considers the interaction between ionospheric plasma and spacecraft instruments under different plasma conditions. This is achieved by simulating space plasma interaction with two different particle sensors; namely, DEMETER's Segmented Langmuir probe (SLP) and JOULEII Suprathermal Ion imager (SII). The current characteristics of the SLP are computed with particle in cell (PIC) code, under different plasma conditions. The current collected by each segment varies with the orientation of the plasma flow velocity, the plasma composition and with the orientation of the magnetic field. For validation of the simulations, the computed characteristics are compared with DEMETER in situ measurements. Simulation results are found to be in good agreement with measurements. Finally, the impact of plasma flow on ion velocity distributions in the vicinity of the SII sensor aperture is numerically investigated. It is

observed that the plasma flow modifies the electrostatic sheath and affects the velocity distributions of NO^+ and O_2^+ ions at the aperture of the SII sensor. The velocity distribution functions at the SII aperture are used to compute ion fluxes on the SII micro channel plate (MCP) and computed fluxes are compared with JOULEII measurements.

Acknowledgements

First and the foremost, I would like to express deepest gratitude to my supervisor, Prof. Richard Marchand who has continually and convincingly conveyed a spirit of the adventure in regard to research in the field of Space Physics. He guided my work with endless patience and enthusiasm. I would like to thank my thesis committee members, Professors. F. Fenrich and C. Krauss, for their insightful comments and very pertinent questions regarding my research which helped me to think out of the box. I wish to acknowledge Dr. J. Pierre Lebreton from CNRS France and J. Burchill from University of Calgary for their collaboration during this work. I am greatly indebted to my parents and have no words that justify your efforts. To me you are the best parents in this world. A very special thank to my husband, Jamil who always show concern when things got stressful. I am immensely grateful to my colleagues of the space physics group at the University of Alberta from whom I have learned a lot during my stay here. I also wish to extend my thanks to my sisters, brother and all my friends. Last but not the least, I express my profound thanks and love for my daughter for being so supportive in hard times. I gratefully acknowledge the financial support of the National Science and Engineering Council Canada (NSERC) and from the Pakistan Institute of Nuclear Science and Technology (PINSTECH), Pakistan.

Contents

1	Introduction	1
1.1	Background	1
1.2	Debye shielding	1
1.3	Plasma Oscillations	2
1.4	Occurrence of Plasma	3
1.5	Earth's ionosphere	4
1.5.1	Formation and composition of the Ionosphere	5
1.5.2	Variability of the Ionosphere	7
1.6	Ionospheric Plasma Modeling	7
1.6.1	Fluid model	8
1.6.2	MHD model	9
1.6.3	MHD Waves	10
1.6.4	Kinetic Theory	12
1.6.5	Computational Aspects	13
1.7	Objectives	15
1.7.1	Thesis Outline	15
2	Modeling of ionospheric Magnetic field perturbations	18
2.1	Introduction	18
2.1.1	Motivation	20
2.2	Model	22
2.2.1	Acoustic gravity wave model	22

2.2.2	Ionospheric model	25
2.2.3	Linear MHD model for compressional and shear Alfvén waves	25
2.2.4	Numerical Approach	27
2.3	Results and Discussion	29
2.3.1	TEC perturbations associated with the ion acoustic mode	30
2.3.2	Magnetic field perturbations	31
2.3.3	TEC perturbations associated with the compressional mode	33
2.4	Summary	33
3	Modeling of in situ Langmuir Probe measurements	45
3.1	Langmuir Probe Technique	45
3.1.1	Sheath impact on Langmuir probe measurements	48
3.2	Background Studies	50
3.2.1	Goal of this Study	53
3.3	The DEMETER Segmented Langmuir Probe (SLP)	54
3.4	Numerical Approach	55
3.5	Results and Discussion	58
3.5.1	Reference case	59
3.5.2	Sensitivity to the Plasma flow velocity	60
3.5.3	Ion mass and composition	63
3.5.4	Sensitivity to the magnetic field	65
3.6	Summary	67
4	Test Particle modeling of the JOULEII Suprathermal Ion imager	70
4.1	Introduction	70
4.1.1	Motivation	72
4.2	The Suprathermal Ion Imager: SII	74
4.3	Model Description	75

4.3.1	PIC Modeling	75
4.3.2	Test particle Modeling	78
4.3.3	Results and Discussion	79
4.3.4	Electrostatic Sheath and Plasma Density	80
4.3.5	Modeling of velocity distribution functions	81
4.3.6	Calculation of particle fluxes on the micro channel plate	86
4.4	Summary	92
5	Summary and Conclusions	96

List of Tables

1.1	Description of computational resources used in the PTetra code. These simulations made use of the Westgrid computing facilities. . . .	14
2.1	Physical parameters used in SAMI2 model that also accounts for the acoustic impulse	29
2.2	Comparison between numerical and observational TEC perturbations, [35, 21, 16]	34
3.1	Physical parameters assumed in the reference simulation, corresponding to DEMETER orbit 06911-0 at 8:16 UT	57
4.1	Plasma parameters assumed in the simulation, corresponding to altitude $150km$	75
4.2	Plasma flow velocity (\vec{V}_o) components for different angles (θ) with respect to the boom used in the simulations	77

List of Figures

1.1	Plot of Debye potential ϕ_D and Coloumb potential ϕ_c as a function of distance r from a spherical charge q [2].	3
1.2	Illustration of the Earth's ionosphere inside the magnetosphere [11].	4
1.3	Day and night side variation of electron density in D, E and F layers of the ionosphere (top) [2]. The electron and ion densities as a function of altitude in the ionosphere (bottom) [6].	16
1.4	Aurora green and red lines corresponding to the atomic Oxygen [1].	17
1.5	Vector illustration of shear Alfvén mode (left) and the compressional mode(right).	17
2.1	Profiles of the relative neutral density perturbation (solid line) and velocity perturbation (dotted) associated with acoustic impulse P_1 (top) and P_2 (bottom).	36
2.2	Profiles of the ambient magnetic field B_o (T) (top) and unperturbed plasma density (m^{-3}) (bottom) in the simulations. This equilibrium is used as starting point to model linear perturbations that are presented in this chapter.	37
2.3	Profiles of the $\log_{10}\nu_{in}$ (top) and Alfvén speed (bottom). This equilibrium is used as starting point to model linear perturbations that are presented in this chapter	38

2.4	TEC perturbations as a function of geographic latitudes for the ion acoustic mode associated with pulses P_1 (top) and P_2 (bottom).	39
2.5	2D profiles of magnetic perturbations $b1(T)$ associated with P_1 (top) and P_2 (bottom), 20 min after arrival of pulse at 250km. .	40
2.6	2D profiles of the velocity perturbations v_1m/s (shear Alfvén mode) induced by pulses P_1 (top) and P_2 (bottom), 20 min after arrival of pulse at 250km.	41
2.7	2D profiles of the magnetic perturbations $b2(T)$ associated with P_1 (top) and P_2 (bottom), shortly after the arrival of pulse at 250km.	42
2.8	2D profiles of $v_2(m/s)$ (compressional mode) induced by the acoustic impulse P_1 (top) and P_2 (bottom), shortly after the arrival of pulse at 250km.	43
2.9	TEC perturbations as a function of geographic latitude ($glat$) associated with the compressional mode for pulses P_1 (top) and P_2 (bottom).	44
3.1	Typical I-V curve of a Langmuir probe illustrating the ion current, electron retardation and electron saturation current regions. In the figure V_f is the probe floating potential and V_P , the plasma potential, corresponds to the inflection point in the I-V curve. Reprinted from Lebreton, J.P., 2009 [57].	46
3.2	Illustration of the ion density (top left), electron density (top right) and the sheath potential (bottom) around a Langmuir probe.	49
3.3	Illustration of different trajectories of the ions in thick sheath. .	51
3.4	Segmented Langmuir probe (top) and illustration of the various segments (bottom). Reprinted from Lebreton, J.P., 2006 [57]. . .	55

3.5	Comparison between the simulated and measured I-V curves for segments $S_1, S_2, S_3, S_4, S_5, S_6$ and the guard electrode. The thicker lines show the characteristics for the fast scan and thinner lines show the characteristics for the slow scan. In both cases the solid lines are for the up scan (negative to positive) and dashed lines for the down scan (positive to negative). Circles show the characteristics obtained from the reference case.	61
3.6	Profiles of the sheath potential (left) for weakly biased ($\sim +2V$) and strongly biased ($\sim +5V$) probe, and the corresponding wake in ion density behind the probe (right). Plasma is drifting in Z direction, whereas the orbital velocity of the satellite is in -Z direction.	62
3.7	Comparison between the simulated and measured I-V curves for segments $S_1, S_2, S_3, S_4, S_5, S_6$ and the guard electrode. The measured characteristics and the reference case are the same as in Figure 3.5. Circles show the characteristics obtained from the reference case and Squares represent the characteristics obtained from the stationary plasma case.	64
3.8	Comparison between the measured and simulated I-V curves for segments $S_1, S_2, S_3, S_4, S_5, S_6$ and the guard electrode, showing the effect of the ion composition. The measured characteristics and the reference case are the same as in Figure 3.5. Circles represent the characteristic obtained with the reference case and squares show the characteristics computed with 100% O^+ ions. .	66

3.9	Simulated I-V curves for segments $S_1, S_2, S_3, S_4, S_5, S_6$ and the guard electrode, showing the effect of the magnitude and the orientation of the magnetic field. Circles show the reference case and triangles represent the characteristics obtained with the magnetic field (B') at an angle of 45° with respect to the surface of the top segment. Squares show the characteristics computed without magnetic field.	68
4.1	Illustration of the ion flux on MCP at $T = 294.36s$. The inner and outer circle represent the kinetic energies $2eV$ and $5eV$ respectively. The signal peak is outside the inner circle. Reprinted from Burchill et al., 2012 [70].	73
4.2	Joule payload (top) and illustration of Suprathermal Ion Imager SII (bottom). Reprinted from Burchill et al., 2012 [70].	76
4.3	Illustration of the angle (θ) between the boom and the plasma flow velocity as seen in the spacecraft rest frame. In this illustration zenith is mainly in the \hat{y} direction.	82
4.4	Plasma sheath potential profiles in the $X = 0$ (top) and $Z = 0$ (bottom) plane for $\theta = 90^\circ$	83
4.5	Illustration of ion density profile for $\theta = 0^\circ$	84
4.6	Illustration of ion density profile for $\theta = 90^\circ$	85
4.7	Illustration of NO^+ velocity distribution functions in the $v_z = 0$ plane for $\theta = 0^\circ$. Velocities are normalized with respect to the thermal velocity of NO^+ ($575m/s$).	87
4.8	Illustration of NO^+ velocity distribution functions in the $v_z = 0$ plane for $\theta = 90^\circ$. Velocities are normalized with respect to the thermal velocity of NO^+ ($575m/s$).	88
4.9	Illustration of NO^+ velocity distribution functions in the $v_z = 0$ plane for $\theta = -90^\circ$. Velocities are normalized with respect to the thermal velocity of NO^+ ($575m/s$).	89

4.10	Illustration of fluxes on the MCP in the XY plane for various angles θ . Fluxes are shown as seen from the tip of the boom looking in the $-Z$ direction, toward the spacecraft main body. .	91
4.11	Simulation results illustrating the variation in the computed ion fluxes on the MCP as a function of time which is estimated from the spin angle (top). For comparison, the time series plot of Joule II 36.234 total flux at an altitude $150km$ (bottom) is also shown. The vertical red line marked the peak position.	94
4.12	Plot of simulated fluxes as a function of the spin time for the right half of the MCP. Here a possible malfunction in the MCP is taken into account.	95

Chapter 1

Introduction

1.1 Background

Plasma is referred to as the fourth state of matter. It is a quasineutral gas of charged particles that exhibits collective behavior. At large scales, plasma is quasineutral which means that the same volume element contains roughly the same number of opposite charges; i.e., $n_i = n_e$. Therefore, the local charge and the electric field vanishes. However, at small scales quasineutrality breaks down which leads to the existence of net charge density and electric field. The spatial scales over which quasineutrality breaks is called Debye length (λ_D). The collective behavior of the plasma comes from the long range Coloumb interactions between charged particles. Debye shielding and plasma oscillations are manifestations of the collective behavior.

1.2 Debye shielding

The Coloumb potential of a test charge q in free space is given by:

$$\phi_c = \frac{q}{4\pi\epsilon_0 r}. \quad (1.1)$$

Due to shielding, the potential in a plasma is different from ϕ_c . In plasma the range of the potential associated with a charge \mathbf{q} is shorter than in vacuum. The reason is that free charges in a plasma tend to redistribute themselves, so as to effectively cancel the potential associated with \mathbf{q} . As a result the charge is effectively shielded, and the potential becomes negligible at distances exceeding a few Debye length " λ_D ". This potential is called Debye potential and is given by [2, 9, 5]:

$$\phi_D = \frac{q}{4\pi\epsilon_0 r} \exp\left(\frac{-r}{\lambda_D}\right). \quad (1.2)$$

Therefore, the Debye length is the spatial scale over which mobile charges screen out the electric field of the perturbed charge in plasma. In Eq. 1.2, neglecting the contribution from ions for simplicity, the Debye length λ_D is defined by:

$$\lambda_D = \left(\frac{\epsilon_0 k_B T_e}{n_o e^2}\right)^{\frac{1}{2}}. \quad (1.3)$$

Here, n_o is the plasma density, k_B is Boltzmann Constant and T_e is the electron temperature. A plot showing comparison of ϕ_D and Coloumb's potential ϕ_c as a function of distance r is shown in Figure 1.1.

1.3 Plasma Oscillations

When plasma is disturbed from an equilibrium, many different types of waves or normal modes can be excited, and propagate in the system. An important and ubiquitous special case of such perturbations is the "electron plasma wave" or "Langmuir wave". In these oscillations, owing to their larger masses, ions are immobile, while electrons oscillate due to electrostatic restoring forces. These oscillations occur at the "electron plasma frequency" (ω_{pe}) given by [2]:

$$\omega_{pe} = \left(\frac{n_e e^2}{\epsilon_0 m_e}\right)^{\frac{1}{2}}. \quad (1.4)$$

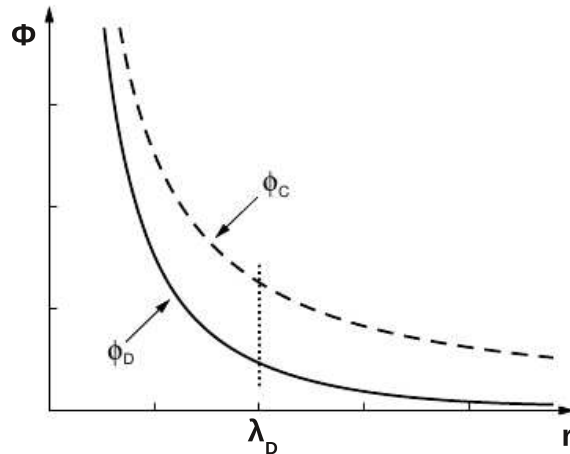


Figure 1.1: Plot of Debye potential ϕ_D and Coloumb potential ϕ_c as a function of distance r from a spherical charge q [2].

Here n_e is the electron density and m_e is the mass of the electron.

1.4 Occurrence of Plasma

Plasma, a gas of free charged particles, can be produced by heating or exposing ordinary gas to ultraviolet light or X-rays. More than 99% of the visible universe is thought to be in the state of plasma. It occurs, for example, in stars, a flickering aurora, the solar corona, lightning and many laboratory experiments such as tokamak devices. As we move away from the surface of the earth, beyond $100km$, plasma exists in various forms e.g. earth's ionosphere and magnetosphere, solar wind, solar corona and photosphere as well as in stellar interiors. This thesis is focused on selected aspects of earth's ionosphere and its interaction with in situ instruments. It is therefore, appropriate at this point to briefly review some basic physics and phenomenology of the ionosphere [9].

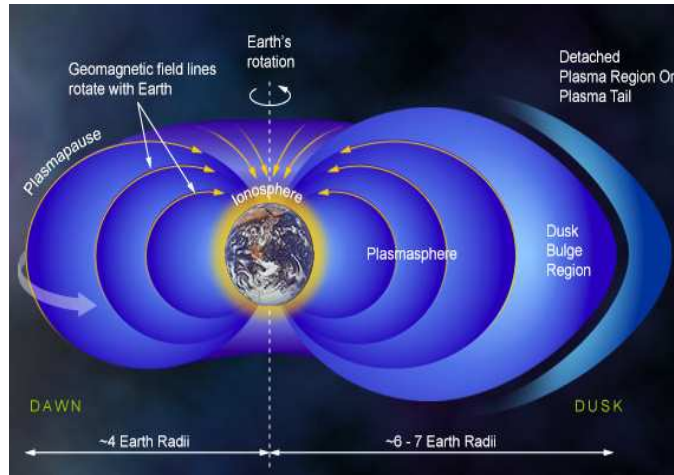


Figure 1.2: Illustration of the Earth's ionosphere inside the magnetosphere [11].

1.5 Earth's ionosphere

Earth is surrounded by different gases and dust particles. At lower altitudes the atmosphere is mostly neutral. At altitudes above approximately 85km , the chemistry of the atmosphere changes considerably, and an important component of ionized molecules and atoms appears. The ionosphere is the ionized region which starts at approximately 85km and extends to a few thousands of kilometers, thus making the base of the magnetosphere. The magnetosphere is the cavity formed by the supersonic solar wind plasma as it hits the terrestrial magnetic field and is deflected around it. The ionosphere is the transition region between the neutral atmosphere and the fully ionized magnetospheric plasma. Inside the magnetosphere, there is a donut shaped region known as the plasmasphere. It is an extension of the Earth's ionosphere as illustrated in Figure 1.2. It contains a partially ionized collisional plasma in which the rate of ion neutral collisions is larger than that of Coloumb collisions. The existence of the ionosphere is evident from the landmark experiment on the transatlantic

radio communication by Marconi, 1901. The experimental demonstration of the deflection of radio waves around the earth's surface to a much greater extent than could be attributed to diffraction. Radio signals can also reflect from the conducting layer in the upper atmosphere back toward the earth. The reflection properties of this conducting layer is affected by solar UV radiation and it affects radio wave propagation [13].

1.5.1 Formation and composition of the Ionosphere

The formation and existence of the ionosphere is due to several sources that are responsible for ionizing neutral gas atoms and molecules. There are two main sources of ionization: solar radiation and energetic particle precipitation. The counteracting processes are attachment and recombination. Plasma source and sink terms vary sensitively with solar illumination and space weather conditions. As a result the degree of ionization varies with time (seasonally and diurnally), with geographic location (altitude and latitude) and with solar activity. Solar radiation (Extreme Ultraviolet(EUV), Ultraviolet (UV) and Xrays) are the dominant source of ionization in the low and mid latitude ionosphere. Recombination and attachment processes also vary with altitude which also affect the electron density. Electron density variations divide the ionosphere in three different layers known as D, E and F as shown in Figure 1.3. Radio sounding of the ionosphere also indicated the existence of these distinct layers in the ionosphere. These layers are characterized by a density peak at specific altitudes as briefly explained below:

D region The region below an altitude of $90km$ constitutes the lower ionosphere. It is weakly ionized and dominated by the neutral dynamics and composition. The main sources of ionization are EUV and X-rays.

E region The region extending from $90km$ up to $160km$ is called E region. The ionization peak occurs at approximately $110km$. It is formed by

the absorption of longer wavelength UV's that can penetrate to lower altitudes. It contain partially ionized plasma composed of molecular ions such as NO^+ , O_2^+ and N_2^+ .

F region The region beyond $160km$ constitutes the F region, which is further divided into two layers; i.e., F_1 and F_2 . The F_1 region is a day side feature of the ionosphere and it has an ionization peak at approximately $200km$. The F_2 region however, exists by day and night with an ionization peak at approximately $300km$. Plasma in this region is composed mainly of O^+ ions, with relatively small fractions of H^+ and He^+ ions [2, 13]. The concentrations of electrons and ions at different altitudes in the ionosphere are also shown in the Figure 1.3.

High Latitude Ionosphere At high latitudes ($\geq 70^\circ$) in the polar cap and the auroral zone, energetic particle precipitation is an important source of ionization. The geomagnetic field lines extend deep into space in the anti sunward direction thus along open field lines. Energetic particles (mostly electrons) from the plasma sheet travel along the magnetic field lines into the ionosphere. These particles collide with neutral atoms and molecules and cause excitation and ionization. When excited atoms and molecules radiatively decay to their ground state, they emit optical radiations of different wavelengths. This radiation in turn is the source of aurora. The earliest phenomenon originating in the upper atmosphere, observed by mankind was the aurora Borealis (Northern lights) and aurora Australis (Southern lights) [13]. Aurora appear in the night sky in the form of arcs, bands, patches and rays. The most commonly observed aurora are green (corresponding wavelength $\lambda = 557nm$) and red (corresponding wavelength $\lambda = 630nm$) due to excitation of atomic Oxygen at low altitudes (between $100km$ to $200km$) and high altitudes ($200km$) respectively as shown in the Figure 1.4 [2].

1.5.2 Variability of the Ionosphere

The ionosphere exhibits temporal and spatial variations. The origins of ionospheric variability can be characterized as follows:

Solar Radiation The solar radiation which ionizes the atmosphere, varies with the solar cycle as well as day-to-day variations in solar activity. The solar flux induces variations in the neutral composition, neutral temperatures and plasma densities. The solar zenith angle dependence in turn leads to diurnal and seasonal variations in the ionosphere.

Solar wind conditions The interaction between solar wind and the geomagnetic field leads to modifications of the global structure of *F – region* ionosphere. The disturbed solar wind conditions induce changes in neutral composition and energetic particle precipitation.

Meteorological influences During the past few decades, it has been recognized that the state of the ionosphere is also determined by processes taking place in the lower atmosphere. These are called meteorological effects and they occur as a result of upward propagating gravity waves. The coupling between these waves with ionosphere leads to the modification of the E-region ionosphere. Many studies are presented to assess the variability of ionosphere in response to the above mentioned factors. For example, Forbes, M.J. et al, 1999, examined ionosonde data in order to quantify the ionospheric variability [3].

1.6 Ionospheric Plasma Modeling

In this thesis, different computational models are used to simulate ionospheric plasma perturbations and the interaction of ionospheric plasma with spacecraft. These models are based on the fluid and kinetic description of ionospheric plasma. In particular, the low-mid latitude ionospheric model SAMI2 is based

on a fluid description of plasma. Magnetic perturbations and low frequency waves are described in the magnetohydrodynamics(MHD) approximation. The interaction between the ionospheric plasma and spacecraft is studied with codes based on a kinetic description of the plasma. It is therefore necessary to give an overview of these different plasma models.

1.6.1 Fluid model

In this approach ionospheric plasma is treated as a fluid which is composed of ions and electrons. Plasma dynamics is described by a set of fluid equations. These are the continuity, the momentum and the energy conservation equations. In SAMI2 the continuity and momentum equations are solved for seven ion species. The equations for the temperature are solved for H^+ , He^+ , O^+ ions and for electrons. The temperature of molecular ions NO^+ , O_2^+ and N_2^+ is equal to that of O^+ . The continuity equation for ions is given by:

$$\frac{\partial n_i}{\partial t} + \nabla \cdot (n_i \vec{V}_i) = P_i - n_i L_i. \quad (1.5)$$

Here P_i , is a source term. It corresponds to the production of ions due to photoionization of the neutrals. n_i and \vec{V}_i represent the ion density and velocity. L_i , is a sink term which is related to recombination losses. The momentum density conservation equation for ion is given by [24]:

$$\frac{\partial(\rho_i \vec{V}_i)}{\partial t} + \nabla \cdot (\rho_i \vec{V}_i \vec{V}_i) = -\nabla p_i + n_i e (\vec{E} + \vec{V}_i \times \vec{B}) + \rho_i \vec{g} - \rho_i \nu_{in} (\vec{V}_i - \vec{V}_n) - \rho_i \nu_{ij} (\vec{V}_i - \vec{V}_j) \quad (1.6)$$

where p_i is the thermal pressure for ion species, \vec{V}_n is the neutral velocity, ν_{in} is the ion-neutral collision frequency, ν_{ij} is the ion-ion collision frequency, \vec{E} and \vec{B} represent the electric and magnetic field. In Eq. 1.6 the momentum loss terms due to recombination and ionization are assumed to be small and they

are neglected for simplicity. The energy equation for ions is given by [24]:

$$\frac{\partial T_i}{\partial t} + \vec{V}_i \cdot \nabla T_i + \frac{2}{3} T_i \nabla \cdot \vec{V}_i + \frac{2}{3 n_i k_B} \nabla \cdot \vec{Q}_i = Q_{in} + Q_{ie}. \quad (1.7)$$

Here T_i is the ion temperature, $\rho_i = n_i m_i$ is the ion mass density, \vec{Q}_i is ion heat flux, Q_{in} is heating due to ion-neutral collision, and Q_{ie} is heating due to ion-electron collision. In SAMI2 there are two approximations made in order to solve the equation of motion for electrons. The first approximation is that the electron inertia term is ignored due to the small electron mass. The second approximation is that the electron neutral collision frequency is very small; i.e., $\nu_{en} \ll \Omega_e$ at altitudes beyond $75km$ and therefore, the corresponding terms are ignored [12]. The resulting equation of motion for electron can be written as:

$$-\nabla p_e - e(\vec{E} + \vec{V}_e \times \vec{B}) = 0 \quad (1.8)$$

where p_e is the electron thermal pressure [24].

1.6.2 MHD model

MHD is a single fluid theory which is a further simplification of multi fluid theory [2]. It treats plasma as a conducting fluid which can be described by a combination of fluid equations, Maxwell's equations and Ohm's law.

Fluid Equations The motion of a MHD fluid is described by the mass continuity and the momentum equations as given by:

$$\frac{\partial \rho_i}{\partial t} + \nabla \cdot (\rho_i \vec{V}_i) = 0 \quad (1.9)$$

$$\frac{\partial (\rho_i \vec{V}_i)}{\partial t} + \nabla \cdot (\rho_i \vec{V}_i \vec{V}_i) = \vec{J} \times \vec{B} - \rho_i \nu_{in} (\vec{V}_i - \vec{V}_n). \quad (1.10)$$

Ohm's Law Ohm's law is used to describe conducting media and it relates

the current density \vec{J} with the applied fields. It is given by:

$$\vec{J} = \sigma(\vec{E} + \vec{V}_i \times \vec{B}). \quad (1.11)$$

Here, σ is the conductivity. It is related to the plasma density (n_o) and electron-ion collision frequency (ν_{ei}) through the relation $\sigma = \frac{n_o e^2}{m_e \nu_{ei}}$. In partially ionized plasma such as in the ionosphere $\nu_{ei} \ll \Omega_e$ where $\Omega_e = \frac{eB}{m_e}$ is the electron gyrofrequency [12]. Therefore, electron-ion collisions are negligible and in ideal MHD approximation Ohm's law reduces to the following form:

$$\vec{E} + \vec{V}_i \times \vec{B} = 0. \quad (1.12)$$

Maxwell's Equations Plasma is composed of charged particles which are affected by the ambient electromagnetic fields. These fields are described by Maxwell's equations under the following MHD assumption that plasma is electrically neutral and therefore, the net charge density vanishes. The resulting reduced Maxwell's equations used to derive magnetic field perturbations are given by [2]:

$$\nabla \times \vec{E} = -\frac{\partial \vec{B}}{\partial t} \quad (1.13)$$

$$\nabla \times \vec{B} = \mu_o \vec{J} + \frac{1}{c^2} \frac{\partial \vec{E}}{\partial t}. \quad (1.14)$$

1.6.3 MHD Waves

The MHD model described in last section is used to describe magnetic field perturbations and the propagation of small amplitude waves in the ionosphere. The plasma is assumed to be cold and therefore, the thermal pressure term is ignored in the momentum equation. In the cold plasma approximation, there are two low frequency modes: the shear Alfvén and the compressional

mode. The relevant equations are obtained by using linear perturbation theory. According to linear perturbation theory, the physical quantities ρ , \vec{V}_i , and \vec{B} consist of two parts: *a*) time independent quantities and *b*) small perturbations. Thus physical variables of interest can be written as: $\rho = \rho_o + \rho_1$, $\vec{V}_i = \vec{V}_1$ and $\vec{B} = \vec{B}_o + \vec{B}_1$, where subscript *o* refers to the equilibrium quantities and subscript 1 refers to small, first order perturbations. By using this approach, two sets of linearized first-order equations describing the shear Alfvén and the compressional mode are obtained. The corresponding equations are given in Chapter 2, but a brief overview of these modes is given here.

Shear Alfvén mode These are transverse waves in which the plasma perturbations are perpendicular to the ambient magnetic field \vec{B}_o . The vector diagram of the shear Alfvén mode is shown in Figure 1.5. It can be seen that \vec{B} and \vec{V} represent the perturbed magnetic field (\vec{B}_1) and the ion velocity (\vec{V}_1) respectively. The vector illustration shows that both \vec{B} and \vec{V} are parallel to each other and perpendicular to the background magnetic field \vec{B}_o and the wave vector \vec{k} . The fact that \vec{V} is perpendicular to \vec{k} ; i.e., $\vec{k} \cdot \vec{V} = 0$ implies that shear Alfvén waves does not involve compression of the fluid. Propagation of the wave is along \vec{B}_o with the phase velocity given by:

$$V_p = V_A \cos\theta \quad (1.15)$$

where V_p is the phase velocity, V_A is the Alfvén velocity and θ is the angle between \vec{k} and \vec{B}_o . These waves can transport energy only along the ambient magnetic field.

Compressional mode The compressional mode is also called the fast Alfvén mode because its phase speed is higher than that of the shear Alfvén mode. The compressional wave mode can transport energy isotropically in any direction with a group velocity (V_g) equal to the Alfvén speed V_A . The vector diagram of the compressional mode is shown in the Figure

1.5. For the compressional mode $\vec{k} \cdot \vec{V} \neq 0$ and $\vec{k} \cdot \vec{B} = 0$ which implies that it involves a compression of plasma and the magnetic field [5].

1.6.4 Kinetic Theory

Kinetic theory is a statistical approach to compute the average motion of large number of particles. At any given time the state of these particles is represented by a point in 6D phase space in which the coordinates consist of a particle spatial coordinates and canonical momenta. The probability density for finding a particle with velocity \vec{v} to be located at position \vec{r} , is proportional to distribution function $f(\vec{r}, \vec{v}, t)$. Various macroscopic averages can be obtained by taking the moment of the velocity. The general expression for the k th velocity moment is given by [10]:

$$g_k = \int v^k f_s(\vec{r}, \vec{v}, t) d^3v. \quad (1.16)$$

The zeroth moment is the number density of species s and is given by:

$$n_s = \int f_s(\vec{r}, \vec{v}, t) d^3v. \quad (1.17)$$

A frequently used distribution to describe a collisionless and drifting plasma is called drifting Maxwellian velocity distribution. It is given by:

$$f(v) = n \left(\frac{m}{2\pi k_B T} \right)^{\frac{3}{2}} \exp\left(-\frac{m(\vec{v} - \vec{v}_d)^2}{2k_B T} \right). \quad (1.18)$$

Here, n is the number density, T is the temperature, and \vec{v}_d is the plasma drift velocity. If plasma is stationary ($\vec{v}_d = 0$) then the distribution is simply a Maxwellian. In a Maxwellian distribution the exponent is the ratio of the kinetic energy ($W = \frac{1}{2}mv^2$) to the average thermal energy ($k_B T$). When particles are moving in the presence of an electric potential ϕ , however, then the total energy of the particle is $W = \frac{1}{2}mv^2 + q\phi$ and the resulting equilibrium

distribution function becomes:

$$f(v) = n \left(\frac{m}{2\pi k_B T} \right)^{\frac{3}{2}} \exp - \left(\frac{\frac{1}{2}mv^2 + q\phi}{k_B T} \right) \quad (1.19)$$

where ϕ is the electrostatic potential. The kinetic equation that describes the evolution of the distribution function in time is known as Vlasov's equation and is given by:

$$\frac{\partial f}{\partial t} + \vec{v} \cdot \nabla_x f + \frac{q}{m} (\vec{E} + \vec{v} \times \vec{B}) \cdot \nabla_v f = 0. \quad (1.20)$$

The test particle modeling used in this thesis is based on Liouville's theorem. In Eq. 1.19 the left hand side is a convective derivative; i.e., $\frac{d}{dt} = \frac{\partial}{\partial t} + \vec{v} \cdot \nabla_x + \frac{q}{m} (\vec{E} + \vec{v} \times \vec{B}) \cdot \nabla_v$. Therefore, Eq. 1.19 can be written as:

$$\frac{df}{dt} = 0. \quad (1.21)$$

Eq. 1.20 shows that in the absence of short range forces, the distribution function remains constant along a particle trajectory. This corresponds to Liouville's theorem for a system of N point particles in classical statistical physics [5].

1.6.5 Computational Aspects

The results presented in this thesis are based on four different kinds of codes. SAMI2 [24] and TOPO [34] are coupled to solve the partial differential equations that represent the Shear Alfvén and the compressional modes. The code made use of 2D grid on a given magnetic meridian. The grid is composed of 2×10^4 cells and the code runs on a single processor job with 1GB of memory. The PTetra code used to simulate the interaction between spacecraft instruments and ionospheric plasma is a multiprocessor code based on the Message passing interface (MPI) [58]. PTetra simulations are run until a steady state is

Table 1.1: Description of computational resources used in the PTetra code. These simulations made use of the Westgrid computing facilities.

Geometry	cells	Particles	Processors and memory
SLP and post	4.5×10^5	50×10^6	10 with 1Gb
SII, boom and Payload	2×10^6	100×10^6	50 with 2GB
SII and boom	1×10^6	50×10^6	5 with 2GB

achieved. For the segmented Langmuir probe (SLP) the time required to reach steady state varies with the probe bias voltage. Negatively bias probe which leads to the ion current branch of the IV curve required a longer time to reach steady state than that of positive bias. For the Suprathermal Ion Imager (SII) the time required to achieve steady state depends on the size of simulation domain. The large simulation domain which consists of SII, the boom and the payload takes longer time to reach steady state than that of the smaller domain. The efficiency of the code is increased by performing numerical simulations with more than one processor. The choice of the number of processors depends on the size of simulation domain, the number of cells and the number of simulated particles. The description of the grid size, number of processors, memory and the injected particles for PTetra simulations are given in Table 1.1. Test particle modeling is used to compute the particle velocity distribution functions and fluxes on the MCP [74]. The velocity distribution functions are calculated for NO^+ and O_2^+ at 36 locations in the vicinity of the SII sensor for different plasma flow directions. The Test particle code runs on a single processor and it uses a 3D adaptive velocity grid at each position \vec{r} . The computation time and the memory depend on the mesh resolution which is based on the minimum and maximum refinement of the velocity grid. The computer memory used in backward Liouville's calculations is $2GB$. The computation of the particle fluxes on MCP by using forward Liouville's approach requires memory $7GB$ and therefore, these calculations are also done on Westgrid computers.

1.7 Objectives

In this thesis, 2D and 3D numerical modeling is used to investigate selected aspects of ionospheric physics. Firstly, the coupling between the neutral atmosphere and the ionosphere is studied. It is shown that this coupling can lead to the generation of Shear Alfvén and compressional waves, when a large amplitude acoustic impulse associated with earthquakes reach ionospheric altitudes. Secondly, the interaction between particle sensors and the ionospheric plasma is simulated. This is done by comparing kinetic simulation results with in situ measurements of two types of sensors: DEMETER's segmented Langmuir probe and Joule2's Suprathermal Ion Imager.

1.7.1 Thesis Outline

The thesis is organized in the following manners: Chapter 2 presents a simple 2D seismo-ionosphere coupled model to explain the ionospheric perturbations generated by earthquakes. This work is largely based on a published article by Imtiaz, et al., 2012 [7]. Chapter 3 investigates a number of factors contributing to the current characteristics of a Segmented Langmuir probe (SLP) using the 3D particle in cell code PTetra. This work is largely based on a published article by Imtiaz, et al., 2013 [8]. Chapter 4, also uses PTetra to simulate the interaction between the Suprathermal Ion Imager (SII) sensor and surrounding plasma. Test particle calculations are then used to compute ion distribution functions at the aperture of the sensor, and to track them inside, down to the array of detectors forming the Micro channel plate (MCP). The results are compared with in situ measurements from the NASA sounding rocket 36.234 as a part of the Joule2 mission. This chapter is largely based on a manuscript which, as of this writing, will soon be submitted for publication. Chapter 5 contains the summary and conclusion of the thesis.

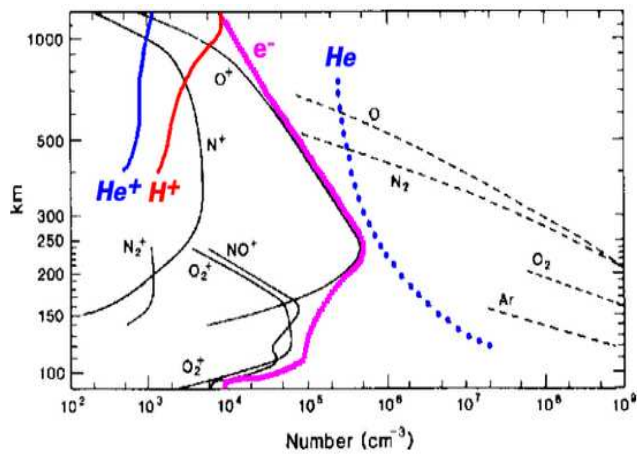
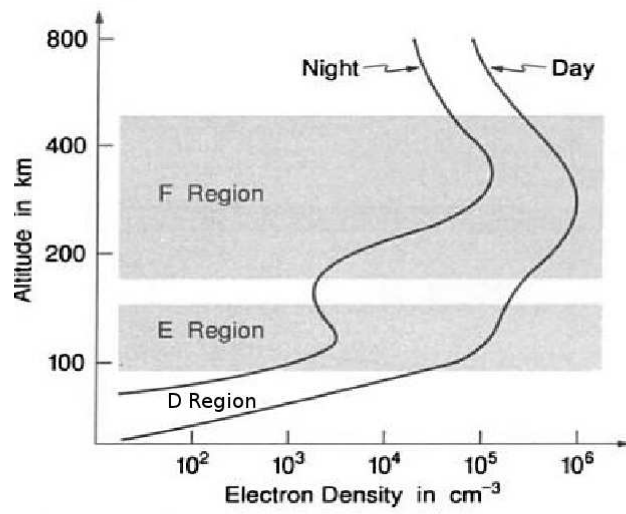


Figure 1.3: Day and night side variation of electron density in D, E and F layers of the ionosphere (top) [2]. The electron and ion densities as a function of altitude in the ionosphere (bottom) [6].



Figure 1.4: Aurora green and red lines corresponding to the atomic Oxygen [1].

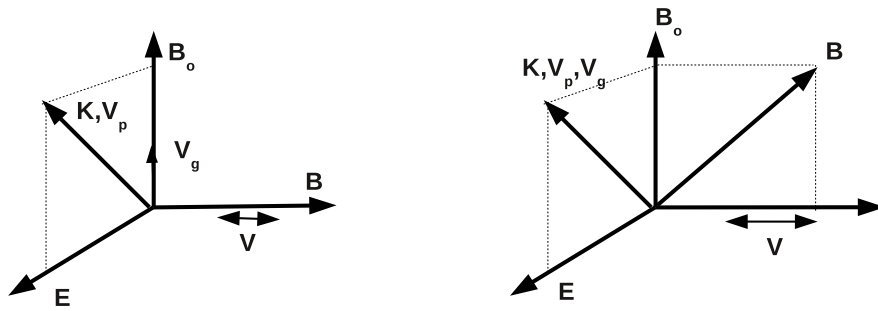


Figure 1.5: Vector illustration of shear Alfvén mode (left) and the compressional mode(right).

Chapter 2

Modeling of ionospheric Magnetic field perturbations

This chapter focuses on the numerical study of ionospheric perturbations resulting from the seismo-ionospheric coupling. For this purpose a simple coupled seismo-ionospheric model is developed that describes the ionospheric perturbations, in particular the magnetic field perturbations associated with Earthquakes. Simulation results illustrating the magnetic field and the associated total electron content (TEC) perturbations are then presented. Numerical values of the perturbed TEC obtained from the model are also compared with satellite and GPS based data.

2.1 Introduction

Acoustic gravity waves (AGW's) are generated by events on the earth's surface such as earthquakes, mine blasts, volcano eruption, tsunamis, underground explosions that cause local displacement of the neutral atmosphere. If these neutral atmospheric pressure perturbations occur over large areas, they can travel to large altitudes without being significantly attenuated by diffraction. As altitude increases, the background neutral density decreases and the wave

amplitude increases as a consequence of wave energy conservation. These waves can reach ionospheric altitude and induce detectable traveling ionospheric disturbances [18, 15, 30]. Damping of neutral acoustic waves in the upper atmosphere is caused by thermal diffusion and mainly viscosity [14]. Following an earthquake, a variety of signatures are observed in the ionosphere. These include plasma density perturbations, temperature and electromagnetic perturbations. The advancement in technology over the past few decades has made it possible to detect ionospheric perturbations associated with seismic induced gravity waves. The DEMETER satellite, launched on 29 June 2004, was devoted to study seismo-ionospheric perturbations induced by earthquakes and other geophysical phenomena. Several authors have presented analyses based on DEMETER data to illustrate the connection between seismic activity and ionospheric perturbations. In pre-seismic effects, Parrot et al., 2006 studied seismo-electromagnetic signatures before two earthquakes of magnitude 6.9 and 7.4 which occurred in the region of the Kii-Peninsula. They found an increase in the power spectrum intensity of electric field and a sudden change in the cut off frequency of the electromagnetic waves [37]. Nemeč et al., 2008 presented a statistical study based on DEMETER data in order to analyze the intensity of very low frequency (VLF) electromagnetic waves in the vicinity of the earthquakes. They found that during the night, there is a significant decrease in the intensity of VLF before an earthquake [36]. Muto et al., 2008 observed a decrease of signal to noise ratio (SNR) in VLF transmitter signals at the time of the earthquake. Their study is based on eight earthquakes of magnitude greater than 5 [32]. Another powerful tool used to map the ionospheric perturbations is the GPS ground based network system. Total electron content (TEC) observations with the GPS tracking network provide a very comprehensive system to detect ionospheric density perturbations. The Total Electron Content (TEC) is the integral of the electron density along a line of sight from the transmitter to the receiver. Liu et al., 2001, Trigunait et al., 2004, Kiryushkin et al., 2007

analyzed GPS-TEC data to assess the pre-seismic TEC variations above an earthquake epicenter [31, 39, 26]. Co-seismic ionospheric TEC perturbations were reported by some authors [16, 17, 19, 25]. Computer modeling has been used to analyze TEC profiles from post-seismic GPS-TEC data [22, 38]. Enhancements in the total electron content affect currents and hence electric fields in the ionosphere. Gwal et al., 2006 and Zhang et al., 2010 observed electric field variations in the ionosphere linked to seismic events [23, 42]. Evidence of geomagnetic perturbations in the ionosphere associated with earthquakes is also found in the literature. Many authors performed analyses of signals measured from satellites, in a wide frequency ranges to report geomagnetic perturbations related to earthquakes for example: Telesca et al., 2008 and Kushwah et al., 2009 [40, 27]. In addition, Chavez et al., 2011 developed a method to detect seismo-magnetic signals associated with three earthquakes ($M = 6 - 7.2$) [20].

2.1.1 Motivation

Some computational models have been developed that couple the neutral atmosphere and the ionosphere through gravity waves in order to assess the response of ionospheric plasma. Marchand and Berthelier, 2008 developed a simple model for post seismic ionospheric disturbances above an epicenter up to the conjugate point [33]. Their study made use of the SAMI2 ionospheric model and it focused on plasma density, temperature and ion velocity perturbations. The propagation of these perturbations in the ionosphere along the magnetic field lines gives rise to ion acoustic waves. As they propagate along field lines, ion acoustic perturbations were found to be attenuated and the signal observed at the conjugate point was very weak [33]. Their model however, does not account for magnetic field perturbations which can also be generated when a large amplitude acoustic impulse reaches the ionosphere. Therefore, the motivation behind this study is to construct and use a model that accounts for the magnetic field perturbations in the ionosphere associated with earthquakes. The

inclusion of magnetic field perturbations allows us to calculate the amplitude of post seismic signatures of ionospheric perturbations at the magnetic conjugate point, and assess their detectability. For this purpose a simple model for an acoustic gravity impulse is introduced in the ionospheric model SAMI2 [24]. The gravity impulse affects several ionospheric parameters included in SAMI2. Among them the parameters of interest are the collision frequency, the plasma density, the plasma temperature and the ion velocity. Magnetic perturbations are introduced in this study by solving reduced MHD equations using the finite element code TOPO, and SAMI2 [34]. The two codes are coupled through perturbations in the ion density and the collisional drag force between neutrals and ions. The locally generated magnetic field disturbances are the source of low frequency electromagnetic waves which propagate in the ionosphere at large distances from the source region. Two wave modes are considered: shear Alfvén and compressional modes. The shear Alfvén mode propagates along the ambient magnetic field and the compressional mode propagates transverse to the magnetic field. These modes carry significant perturbations along and transverse to the ambient magnetic field. TEC perturbations associated with the ion acoustic and compressional modes present some interesting features. In particular TEC perturbations associated with the compressional mode are stronger and of longer duration compared to those of the ion acoustic mode. The remainder of this chapter is organized in the following manner: Section 2.2 presents a description of the model, the basic equations and the numerical approach used to solve the system of equations. Section 2.3 presents example results. Finally, Section 2.4 contains a summary and a general discussion of the findings.

2.2 Model

The physical phenomenon under consideration involves ionospheric perturbations induced by the acoustic impulse resulting from seismic activity. To simulate ionospheric plasma perturbations induced by an acoustic wave impulse two coupled codes are used. The first one, SAMI2 is used to model the ionosphere. The second one, TOPO a general purpose finite element code, is used for the description of magnetic field perturbations.

2.2.1 Acoustic gravity wave model

The acoustic impulse of small amplitude (of order of a few mm) and long period (10 – 100s) generated at ground level in an earthquake over large areas, propagate vertically upward. Studies based on gravity waves show that their amplitude increases exponentially with height as the waves propagate upward. This increase is due to the decay of the background atmospheric neutral density and the near conservation of wave kinetic energy. For simplicity in what follows, the neutral atmosphere is treated as an isothermal fluid and pressure is assumed to be related to the mass density through $p = C_s^2 \rho$, where $C_s = (\frac{p}{\rho})^{\frac{1}{2}}$ is the acoustic speed. Given this approximation, the neutral continuity and momentum conservation equations are:

$$\frac{\partial \rho}{\partial t} + \frac{\partial}{\partial z} (\rho v) = 0 \quad (2.1)$$

and

$$\frac{\partial}{\partial t} (\rho v) + \frac{\partial}{\partial z} (\rho v v + \rho C_s^2) = -\rho g. \quad (2.2)$$

The steady state solution to these equations leads to the hydrostatic equilibrium condition given by:

$$\rho = \rho_0 \exp(-z/h). \quad (2.3)$$

In Eq. 2.1 to 2.3, z is the altitude, g is the acceleration due to gravity, $h = \frac{k_B T}{mg}$ is the scale height and ρ_0 is the neutral density at ground level $z = 0$. The equations can also be linearized with respect to this equilibrium, and solved to describe perturbations associated with small amplitude acoustic impulses. Many types of impulses can exist, depending upon different types of perturbation that can occur at ground level. In what follows I consider two types of impulses corresponding to two possibilities of the ground motion are considered. In the first case, denoted with P_1 , the ground is assumed to rise and then move back to its original level. This kind of acoustic impulse is reported by Krasnov et al., 2011. Their investigations are based on the seismic data related to an earthquake in the Czech republic: magnitude: 3.6 and depth of epicenter: 7870m [29]. A solution to the linearized equations above corresponding to this motion is given by:

$$v_{P1} = \sqrt{2}V_0 \frac{z - C_s t}{C_s \tau} \exp\left[\left(\frac{1}{2} + \frac{z - z_0}{2h}\right) - \eta^2\right] \quad (2.4)$$

$$\frac{\rho_{P1}}{\rho_0} = \sqrt{2} \frac{V_0}{C_s} \left(\frac{z - C_s t}{C_s \tau} + \frac{C_s \tau}{4h}\right) \exp\left[\left(\frac{1}{2} + \frac{z - z_0}{2h}\right) - \eta^2\right]. \quad (2.5)$$

The corresponding profiles of the neutral density and velocity perturbations are illustrated in Figure 2.1 (top). It is observed that both the neutral density and velocity perturbations follow the motion of the earth surface. When the ground moves up it lifts the neutral density along with it, and it gives rise to a positive peak in the density and velocity perturbations. The downward motion of the ground leads to a decrease in the neutral density and velocity perturbations. The second case, denoted with P_2 , corresponds to a vertical rise of the ground during a characteristic time τ after which the ground remains at a level higher than the one at which it started; i.e., the ground does not come back to its starting position. This kind of acoustic gravity impulse is observed during underground explosions [28]. A possible solution to the linearized form

of Eq.2.1 and 2.2 corresponding to P_2 is given by:

$$v_{P2} = \sqrt{2}V_0 \exp\left[\left(\frac{1}{2} + \frac{z - z_0}{2h}\right) - \eta^2\right] \quad (2.6)$$

$$\frac{\rho_{P2}}{\rho_0} = \sqrt{2} \frac{V_0 \tau}{h} \exp\left[\left(\frac{1}{2} + \frac{z - z_0}{2h}\right)\right] \left[\frac{\sqrt{\pi}}{4} (1 - \text{erf}(\eta)) + \frac{h}{C_s \tau} \exp[-\eta^2]\right]. \quad (2.7)$$

Profiles for the neutral density and the velocity perturbations corresponding to a pulse of type P_2 are shown in Figure 2.1 (bottom). In the above equations $\eta = \frac{(z - z_0 - C_s(t - t_0))}{C_s \tau}$, V_0 is the maximum perturbed neutral atmosphere velocity at height z_0 , C_s is the local sound speed, t_0 is the time at which the center of the pulse reaches the reference height z_0 , and τ is the half pulse duration. Referring to the Mass Spectrometer Incoherent Scatter (MSIS) model of the neutral atmosphere [13], the sound speed at $z_0 = 250$ km at noon in winter, is taken to be $C_s = 600$ m/s. Considering oxygen(O) as a major species at this height, the scale height h is calculated from $h = \frac{mg}{k_B T} = 41$ km. At altitude of 250 km, where the neutral density has decreased by a factor of 10^{-10} , the neutral velocity perturbations are amplified by approximately 10^5 . For example, a large seism could give rise to a vertical displacement of 2 cm with a period of 10 – 100 s, corresponding to a vertical velocity $2 \times 10^{-5} - 2 \times 10^{-4}$ m/s at ground level. The corresponding perturbed velocity in the ionosphere, at 250 km altitude, would therefore be of order 2 – 20 m/s. Large earthquakes of magnitude 8 – 9 could lead to even larger perturbation amplitudes at these altitudes. A detailed study of lithosphere-atmosphere-ionosphere coupling requires models that couple surface waves on the solid earth, with gravity waves of the neutral atmosphere and the ionosphere. Here I use the two dimensional SAMI2 model and assume that an acoustic impulse defined by neutral velocity and density perturbations, reach ionospheric altitudes 150 – 350 km. The perturbed velocity of neutrals in the ionosphere at 250 km altitude would therefore be of order 1 – 20 m/s, which is 0.2 – 3% of the local sound speed (C_s). The corresponding wave amplitudes are very small, therefore nonlinear effects are

ignorable.

2.2.2 Ionospheric model

The dynamics of the ionosphere is modeled with the 2D mid latitude ionospheric model SAMI2. This model is described in detail by Huba et al., 2000 [24]. The model is based on the fluid description of the ionospheric plasma. It solves the continuity and momentum equations for electrons and seven ion species (H^+ , He^+ , N^+ , O^+ , N_2^+ , NO^+ , O_2^+). It also solves the energy transport equations for electrons and major ion species (H^+ , He^+ , O^+) along the field lines in a given magnetic meridian. It uses a day and night time photoionization model for the temporal variation of plasma density. The neutral wind is included in SAMI2 through an empirical models namely the Horizontal Wind Model (HWM) and MSIS. It also uses fits to the International Geomagnetic Reference Field (IGRF) to approximate the local magnetic field as a tilted and off centered dipole field, with parameters that depend on the selected magnetic meridian. SAMI2 also includes $\vec{E} \times \vec{B}$ drift model, that accounts for slow drifts [24]. In this study we are interested in rapid phenomena such as compressional and shear Alfvén waves; the slow $\vec{E} \times \vec{B}$ drifts included in SAMI2 are small compared to the fast MHD drifts and they are neglected for simplicity. However, $\vec{E} \times \vec{B}$ drifts associated with the short perturbations considered here are included in the linear MHD model which is used for the description of compressional and shear Alfvén waves as discussed in next section.

2.2.3 Linear MHD model for compressional and shear Alfvén waves

Magnetic field perturbations are described in the ideal MHD approximation. A set of linearized MHD equations are obtained from Maxwell's and fluid conservation equations in cylindrical geometry. In these calculations an offset tilted

dipole magnetic field is assumed, with magnetic dipole oriented along the z -axis. Cylindrical coordinates r and z centered on this dipole are obtained through the transformation from the geocentric to the magnetic dipole frame. In these coordinates, the ambient magnetic field (\vec{B}_o), the perturbed magnetic field (\vec{B}_1) and the ion velocity perturbations (\vec{V}_1) can be written as

$$\vec{B}_o = \frac{\mu_o m}{4\pi(r^2 + z^2)^{\frac{5}{2}}}(rz\hat{r} + (2z^2 - r^2)\hat{z}) \quad (2.8)$$

$$\vec{B}_1 = b_1\hat{\phi} + b_2\hat{b} \times \hat{\phi} + b_3\hat{b} \quad (2.9)$$

$$\vec{V}_1 = v_1\hat{\phi} + v_2\hat{b} \times \hat{\phi} + v_3\hat{b} \quad (2.10)$$

$$\hat{b} = u_r\hat{r} + u_z\hat{z} \quad (2.11)$$

where \hat{b} is a unit vector along the ambient magnetic field. Here b_1 , v_1 are the azimuthal (toroidal) components of the perturbed magnetic field and velocity, b_2 , v_2 are the components of the perturbed fields and velocity in the direction perpendicular to \hat{b} and $\hat{\phi}$, b_3 and v_3 are components along \hat{b} . Substituting these expressions in the linearized MHD equations and, consistent with the 2D SAMI2 model, assuming that perturbed quantities are azimuthally symmetric; i.e., they are independent of ϕ , one finds the following set of coupled partial differential equations:

$$\rho_o(1 + \frac{V_A^2}{c^2})\frac{\partial v_2}{\partial t} = \frac{B_o}{\mu_o}[\frac{\partial(u_r b_2)}{\partial r} + \frac{\partial(u_z b_2)}{\partial z} + \frac{\partial(u_z b_3)}{\partial r} - \frac{\partial(u_r b_3)}{\partial z}] - \nu_{in}\rho_o(v_2 - U_2) \quad (2.12)$$

$$\frac{\partial b_2}{\partial t} = u_r \frac{\partial(B_o v_2)}{\partial r} + u_z \frac{\partial(B_o v_2)}{\partial z} + \frac{u_r B_o v_2}{r} \quad (2.13)$$

$$\frac{\partial b_3}{\partial t} = u_z \frac{\partial(B_o v_2)}{\partial r} - u_z \frac{\partial(B_o v_2)}{\partial z} + \frac{u_z B_o v_2}{r} \quad (2.14)$$

$$\frac{\partial \rho_2}{\partial t} = \frac{1}{r} \frac{\partial(r\rho_o u_z v_2)}{\partial r} - \frac{\partial(\rho_o u_r v_2)}{\partial z} \quad (2.15)$$

$$\rho_o(1 + \frac{V_A^2}{c^2})\frac{\partial v_1}{\partial t} = \frac{1}{\mu_o}[B_{oz}\frac{\partial b_1}{\partial z} + B_{or}\frac{\partial b_1}{\partial r} + \frac{B_{or}b_1}{r}] - \nu_{in}\rho_o(v_1 - U_1) \quad (2.16)$$

$$\frac{\partial b_1}{\partial t} = \frac{\partial(B_{or}v_1)}{\partial r} + \frac{\partial(B_{oz}v_1)}{\partial z} \quad (2.17)$$

where ρ_o is the unperturbed plasma density, V_A is the Alfvén speed, ν_{in} is the ion neutral collision frequency and $U_1(U_2)$ is the zonal(meridional) component of the neutral wind. Here B_{or} and B_{oz} represent the radial and zenith components of the ambient magnetic field, where u_r and u_z are the components of the unit vector \hat{b} . In a cylindrically symmetric geometry it can easily be seen that v_2 , b_2 and b_3 represent a compressional (poloidal) mode, while v_1 and b_1 represent a shear Alfvén (toroidal) mode. In Eq. 2.15, ρ_2 represents the perturbed plasma density associated with the compressional mode. In the above equations $\rho_o\nu_{in}(v_s - U_s)$, $s = 1, 2$ is the collisional drag force between ions and neutrals. It is the source of perturbations in the ionospheric magnetic field, plasma density and the ion velocity. It is noted that there is no coupling between the compressional and the shear Alfvén mode.

2.2.4 Numerical Approach

A two dimensional finite element code TOPO, developed by Marchand et al., 1997 [34], is used to solve the system of coupled partial differential Eq. 2.12 to 2.17 by imposing appropriate boundary conditions. TOPO solves equations of the form

$$\sum_{l=1}^N (Z_{kl} \frac{\partial}{\partial t} U_l + \nabla \cdot (A_{kl} U_l) + \nabla \cdot (\vec{B}_{kl} \cdot U_l) + C_{kl} U_l + D_{kl} \cdot U_l) + S_k = 0 \quad (2.18)$$

where U_l is unknown and A_{kl} , B_{kl} , C_{kl} , D_{kl} are known coefficients. The S_k represents the source term. The index k and l runs from 1 to N ; i.e., over the number of equations. The mesh used in TOPO is unstructured with triangular elements. The mesh is aligned along the magnetic field in order to preserve the strong anisotropy of shear Alfvén waves propagating along magnetic field lines. The size of the mesh depends on the horizontal and vertical scales. These

scales vary spatially with altitude. For example, the horizontal scale ranges from 135 to 251 km and the vertical scale ranges from 7 to 13 km. There are four boundaries considered for the simulation domain. Those are: (1) the base of the ionosphere at 90km altitude in the Northern hemisphere, (2) the base of the ionosphere at 90km altitude in the Southern hemisphere, (3) the inner boundary corresponding to the lowest field line (at 500 km maximum altitude) and (4) the outer boundary that corresponds to the highest field line with maximum altitude and latitude are 8000 km and 62° respectively. Two types of boundary conditions are used in the simulations, known as essential (Dirichlet) and natural (Neumann). For the plasma velocity at boundaries 1 and 2 essential boundary conditions are imposed; i.e., the plasma flow velocity is assumed to be equal to the neutral wind velocity. For boundaries 3 and 4 natural conditions are imposed; i.e., all diffusive fluxes are zero at the inner and outer boundary. Natural boundary conditions are imposed for the perturbed magnetic field at boundary 1 and 2. The resulting discretized equations are solved iteratively with the generalized minimal residual (GMRES) method with incomplete LU preconditioning [41]. In order to solve the reduced MHD equations several input parameters are required and they are obtained through coupling with SAMI2. These include the ambient magnetic field, the plasma density, the zonal and meridional components of the neutral wind. Profiles of the ambient magnetic field (B_o), the plasma density (n_o), the collision frequency (ν_{in}) and the Alfvén speed (V_A) in the ionosphere are shown in the Figure 2.2 and 2.3. The ambient magnetic field has a maximum of about $6.3 \times 10^{-5}T$ at the poles and it is minimum at the equator. The profile of unperturbed plasma density shows the maximum value of about $3.3 \times 10^{12}m^{-3}$ at lower altitudes. The ion-neutral collision frequency is higher at the lower altitudes and it decreases at higher altitudes. The Alfvén speed depends on the ratio between the ambient magnetic field and the plasma density which is high at the poles and smaller in the equatorial region. In order to model the seismic

Table 2.1: Physical parameters used in SAMI2 model that also accounts for the acoustic impulse

Physical parameter for P_1 and P_2	Value
Ambient magnetic field (B_o)	6.2×10^{-5} T
Plasma density (ρ_o)	2.5×10^{12} no./m ³
ap index	21
F10.7	188
Local time at start of run	1500 UT
Reference height (h_o)	250 km
Maximum perturbed velocity (V_o at 250 km)	15m/s
Geographic latitude of the epicenter (θ)	36°N
Geographic longitude (ϕ)	90°
Scale height (h)	41 km
Pulse half width in latitude ($\delta\theta$)	1.5°

perturbations in the ionosphere, SAMI2 model containing the neutral density and velocity perturbations associated with impulses P_1 and P_2 , is coupled with TOPO. The coupling between the two codes accounts for the collisional drag force between ions and the neutral atmosphere which is strong in the region where the neutral density perturbation is higher. The parameters used for the two pulses are given in Table 2.1: The epicenter of the event is considered at latitude $\theta = 36^\circ\text{N}$ and longitude $\phi = 90^\circ$ E. The choice was motivated by the fact that this position corresponds to an Indian region which is highly vulnerable to earthquakes. Also, the latitude considered is consistent with the fact that SAMI2 is a mid latitude ($< 62^\circ$) ionospheric model.

2.3 Results and Discussion

In this section, a quantitative study of the effect of seismic activity on the ionosphere away from the epicenter is presented in two steps. As a first step, two impulses P_1 and P_2 are postulated at ionospheric altitudes, and use is made of the 2D model of the ionosphere SAMI2 to calculate the resulting perturbations in the surrounding plasma. The variations in the plasma parameters are studied by comparing simulation results with and without the presence of neutral

acoustic impulse P_1 and P_2 . The propagation of these plasma perturbations along the field line excite ion acoustic waves. The plasma density perturbation (δN_e) is calculated by taking the difference between densities with and without the impulse. From there TEC perturbations are calculated numerically by integrating the perturbed electron density along the radial path in the altitude range 90 – 2000 km. The perturbed TEC is represented by the following integral:

$$\delta TEC = \int_{h_o}^{h_m} \delta N_e dz. \quad (2.19)$$

This quantity is measured in terms of TEC unit (TECU); i.e., $1TECU = 10^{16} \text{electrons}/m^2$. In the second step, the magnetic field perturbations in the ionosphere are modeled by coupling SAMI2 and TOPO. These perturbations are found to excite the shear Alfvén and compressional waves in the ionosphere. The coupled codes are then used to study the electromagnetic perturbations arising from the coupling between neutrals and ionospheric plasma. These include variations in the ion velocity, the magnetic field and TEC values associated with the compressional mode. Simulation results illustrating perturbations in TEC associated with the ion acoustic mode and the compressional mode along with the electromagnetic perturbations are then presented.

2.3.1 TEC perturbations associated with the ion acoustic mode

The ion acoustic mode is obtained directly from SAMI2. It is an electrostatic mode which involves thermal pressure gradients and it propagates parallel to the magnetic field. Acoustic impulses modify the local plasma dynamics through drag forces between ionospheric plasma and the perturbed neutral wind velocity. Variations in the neutral density also result in a perturbation in photoionization, which affects the plasma density. For the assumed amplitude of the two pulses, the maximum relative perturbations in the electron density

associated with pulses P_1 and P_2 are approximately 6% and 20% respectively. The TEC perturbations associated with the ion acoustic mode are computed for the two pulses and are plotted as a function of time and latitude as shown in Figure 2.4. It is observed for pulse P_1 that the maximum TEC perturbation is followed by a minimum and after a short interval the TEC perturbations become zero which is consistent with the behavior of the pulse P_1 . For pulse P_2 , TEC perturbations persist for a longer time after the passage of impulse and the maximum is not followed by the minimum. This hypothetical pulse corresponds to the motion of ground which lead to the lifting of neutral atmosphere to a higher level. Therefore, the corresponding time scale of TEC perturbations associated with pulse P_2 is longer than that for pulse P_1 . A decrease in the perturbed TEC value would require the inclusion of lateral transport of neutrals in the gravity wave model, which is not taken into account here. The maximum TEC perturbations associated with pulse P_1 and P_2 are approximately 0.012 TECU and 0.05 TECU, respectively. It is observed that the maximum TEC perturbations occur at higher latitudes; i.e., $+2^\circ\text{N}$ from the epicenter. The reason for this shift can be explained on the basis of factors that contribute to the coupling. The geometry of the magnetic field lines also contribute to this coupling. For example, strong coupling occurs in the region where the magnetic field lines are more vertical, which occurs at higher latitudes in the Northern hemisphere. The minimum TEC variation for the two pulses is approximately $(2 - 5) \times 10^{-3}$ TECU.

2.3.2 Magnetic field perturbations

Coupling between the neutral atmosphere and the ionosphere also results in magnetic field perturbations. These in turn lead to shear Alfvén and the compressional waves in the ionosphere. The shear Alfvén mode propagates along the ambient magnetic field. This mode is described by v_1 and b_1 in Eq. 2.15 and 2.16. Figure 2.5 shows spatial profiles of toroidal magnetic field perturbations

associated with pulses P_1 and P_2 . The corresponding ion velocity perturbations are shown in Figure 2.6. As expected, both magnetic field and plasma velocity perturbations propagate along the ambient magnetic field. The corresponding relative magnetic field perturbations associated with pulses P_1 and P_2 are of the order 0.008% and 0.03% respectively. The maximum perturbed velocity of the ions for pulses P_1 is of the order of 2 – 3m/s and for P_2 is about 6 – 7 m/s away from the epicenter; i.e., at the equator. The compressional mode arises from the perturbations in the magnetic field and plasma density transverse to the ambient magnetic field and it is described in terms of v_2 , b_2 and b_3 as given by Eqs. 2.12-2.14. It propagates at speeds ranging from 2×10^7 m/s at 250km to 2×10^6 m/s at high altitude. The maximum magnetic field perturbations associated with the compressional mode are illustrated in Figure 2.7 and the corresponding maximum ion velocity perturbations are shown in Figure 2.8. The relative magnetic field perturbations associated with pulses P_1 and P_2 are of the order 1.11% and 2.9% respectively. The corresponding ion velocity perturbations are approximately 17 m/s and 40 m/s, respectively. The variations in the magnetic field and plasma velocity associated with the compressional mode are stronger than for the shear Alfvén mode. This difference arises from the coupling of the two modes with the neutral wind through collisional drag force. The shear Alfvén mode is coupled with neutrals through the zonal component of the perturbed neutral wind. The compressional mode is coupled through the meridional component of the perturbed neutral wind. Given the azimuthally symmetric neutral wind perturbation assumed here, the orientation of Earth magnetic field is such that it couples more strongly with the compressional wave than with the shear Alfvén mode. The shape of the magnetic field lines varies with latitude; i.e., the magnetic field lines are more vertical at higher latitudes. An epicenter at higher latitude would result in a stronger perturbation in the compressional mode and weaker perturbations in the shear mode.

2.3.3 TEC perturbations associated with the compressional mode

The analysis of density perturbations for compressional mode is quantified in terms of the corresponding TEC perturbations. TEC perturbations associated with pulses P_1 and P_2 are shown in Figure 2.9. It is found that the maximum variations in the TEC associated with P_1 and P_2 are about 0.04 TECU and 0.5 TECU, respectively. There are some differences observed in TEC perturbations associated with the compressional mode and that of the ion acoustic mode. These are:

- TEC perturbations associated with the compressional mode are stronger than those of the ion acoustic mode.
- The duration of TEC perturbations associated with the compressional mode is longer than that associated with the ion acoustic mode.
- The maximum TEC perturbations associated with the compressional mode occurs at relatively higher latitudes than that associated with the ion acoustic mode.

This last feature can be explained by the fact that the compressional mode propagates transverse to the ambient magnetic field. The propagation of the compressional mode leads to a strong perturbation in the plasma density and ion velocity in the radial direction. A comparison of numerical results of the perturbed TEC with the GPS/DEMETER data is shown in Table 2.2.

2.4 Summary

In this chapter a simple coupled seismo-ionospheric model is presented which simulates the magnetic field perturbations associated with earthquakes. For the assumed amplitude of the acoustic impulses P_1 and P_2 , the model allows to

Table 2.2: Comparison between numerical and observational TEC perturbations, [35, 21, 16]

Year	Epicenter	$\delta\text{TEC}(\text{TECU})$	Technique
1994	Northridge CA ($34^\circ N$)	0.01	GPS
2002	Denali ($34^\circ N$)	0.05	Satellite
2006	Kuril Islands($46.6^\circ N$)	0.2	Satellite
2003	Tokachi-Oaki ($41.8^\circ N$)	0.7	Satellite
Present study	$36^\circ N$	0.012-0.04	Numerically(P_1)
Present study	$36^\circ N$	0.05-0.5	Numerically(P_2)

compute perturbations in the magnetic field, the plasma velocity and in TEC values. These perturbations are strong in the region where the collisional drag between the ions and neutrals is most significant. Collisional drag between plasma and neutrals depends on the ion-neutral collision frequency. These parameters are therefore, more significant in the altitude range 150 – 350 km. Coupling between the neutral density and the ionosphere results in magnetic field perturbations. This is explained by the fact that a vertically propagating neutral acoustic impulse effectively pushes against the ionospheric plasma due to collisional friction. In the off-centered and tilted dipole magnetic field of Earth, part of this push is in the azimuthal (toroidal) direction and results in a shear Alfvén wave propagating along the background field line. Another part is in the meridional plane and results in a compressional Alfvén wave propagating in the meridional (poloidal) direction. With the longitude and latitude of the epicenter considered, and given the orientation of the local magnetic field, this coupling is found to be stronger for the compressional mode. Also, due to the variation in the direction of the magnetic field with latitude (\vec{B} is more vertical at higher latitudes), it is found that coupling between the neutral impulse perturbation and the ion acoustic wave, increases at higher latitudes. This explains why TEC perturbations associated with ion acoustic perturbations are maximum at latitudes slightly above that of the epicenter. Propagation of the shear Alfvén mode occurs with minimum dissipation and attenuation, compared to the ion acoustic mode. Magnetic field perturbations

associated with the compressional mode are localized in the vicinity of the epicenter. However, magnetic field perturbations associated with the shear Alfvén mode are more likely to be observable in the vicinity of the epicenter up to the conjugate point. As mentioned above, the maximum TEC perturbations obtained in this study have magnitudes that are consistent with observations.

1

¹”A version of this chapter has been published. Imtiaz, N., and Marchand, R.; Modeling of ionospheric magnetic field perturbations induced by earthquakes, *Journal Geophys. Res.*, 117, 2012.”

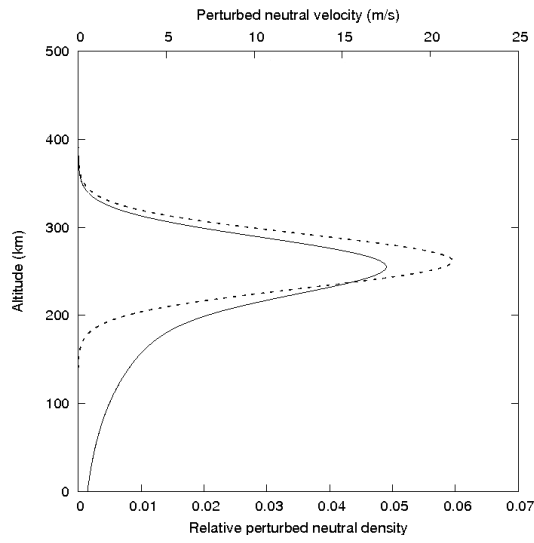
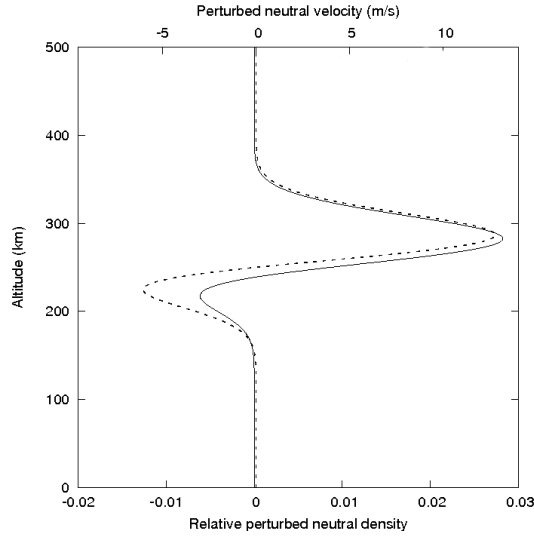


Figure 2.1: Profiles of the relative neutral density perturbation (solid line) and velocity perturbation (dotted) associated with acoustic impulse P_1 (top) and P_2 (bottom).

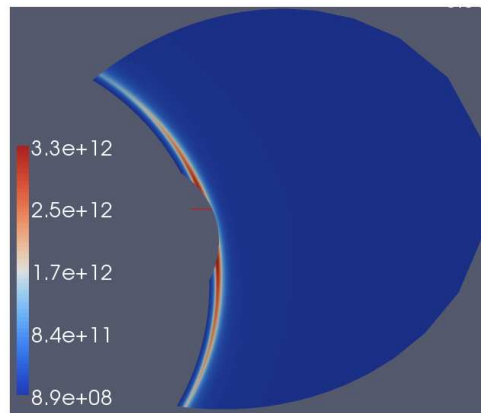
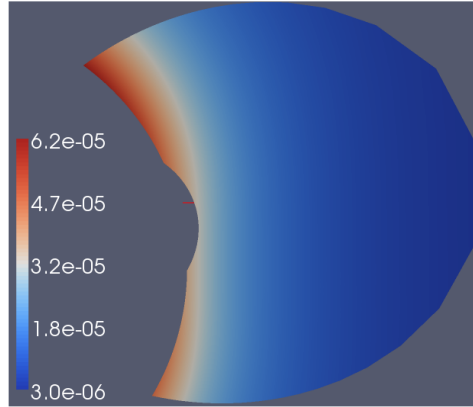


Figure 2.2: Profiles of the ambient magnetic field B_o (T) (top) and unperturbed plasma density (m^{-3}) (bottom) in the simulations. This equilibrium is used as starting point to model linear perturbations that are presented in this chapter.

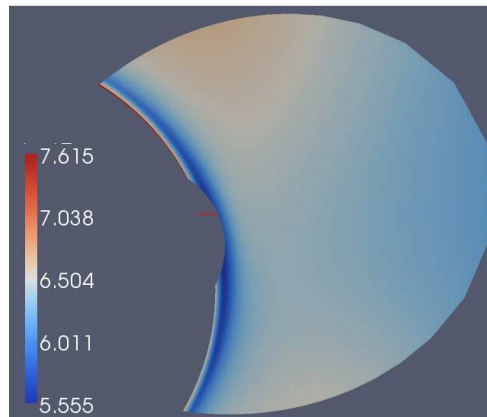
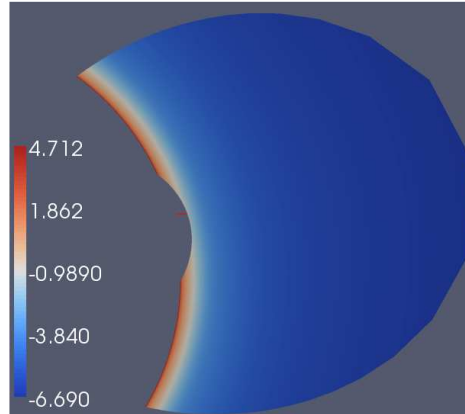


Figure 2.3: Profiles of the $\log_{10} \nu_{in}$ (top) and Alfvén speed (bottom). This equilibrium is used as starting point to model linear perturbations that are presented in this chapter

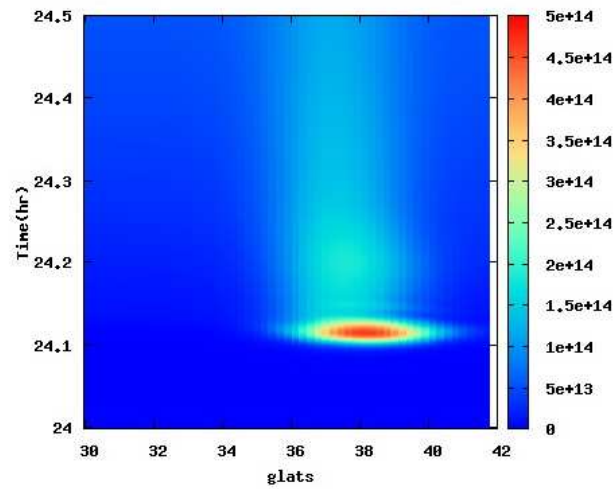
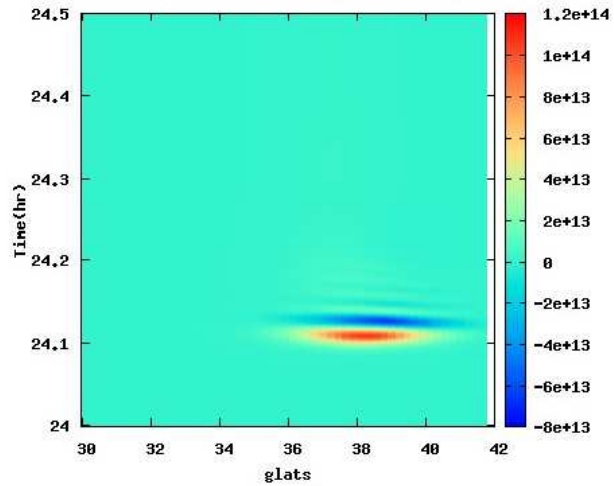


Figure 2.4: TEC perturbations as a function of geographic latitudes for the ion acoustic mode associated with pulses P_1 (top) and P_2 (bottom).

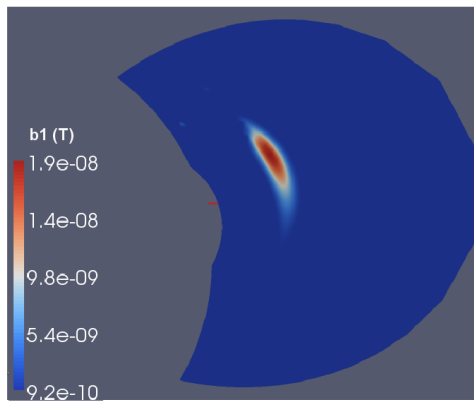
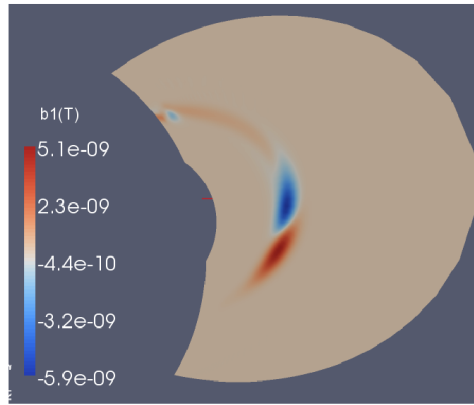


Figure 2.5: 2D profiles of magnetic perturbations $b_1(T)$ associated with P_1 (top) and P_2 (bottom), 20 min after arrival of pulse at 250km .

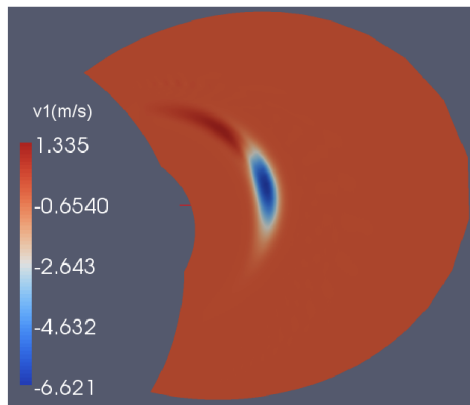
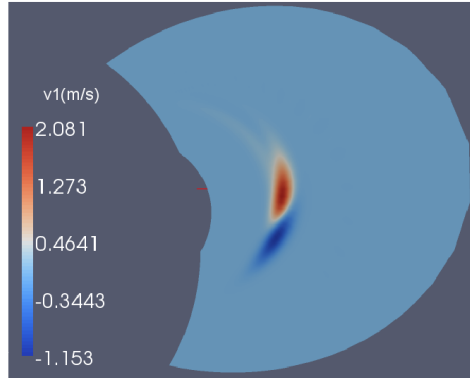


Figure 2.6: 2D profiles of the velocity perturbations $v_1 m/s$ (shear Alfvén mode) induced by pulses P_1 (top) and P_2 (bottom), 20 min after arrival of pulse at $250 km$.

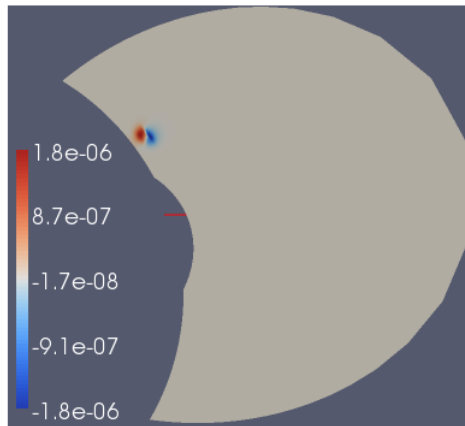
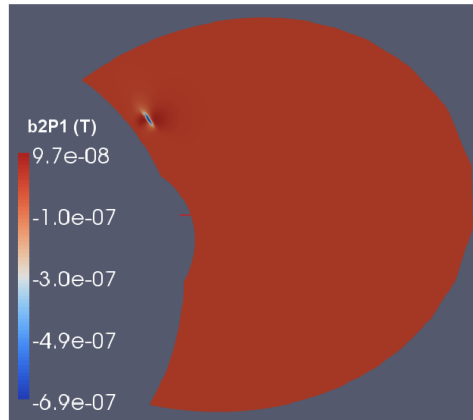


Figure 2.7: 2D profiles of the magnetic perturbations $b_2(T)$ associated with P_1 (top) and P_2 (bottom), shortly after the arrival of pulse at 250km .

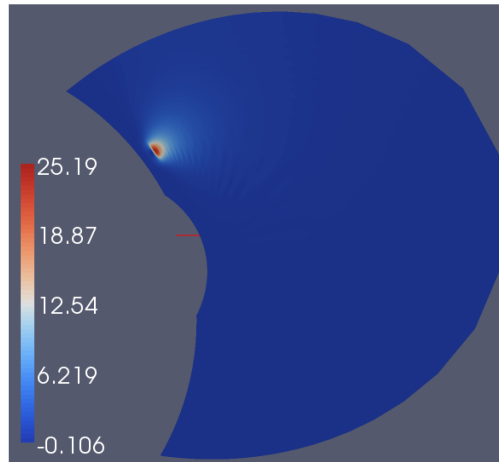
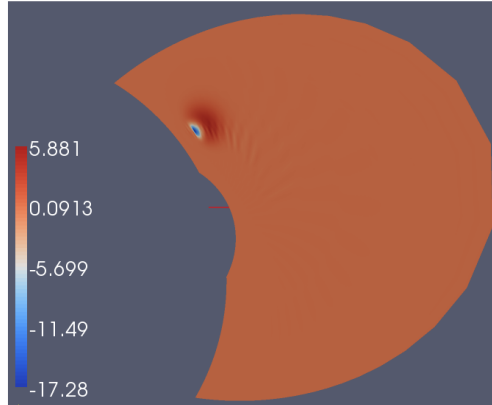


Figure 2.8: 2D profiles of $v_2(m/s)$ (compressional mode) induced by the acoustic impulse P_1 (top) and P_2 (bottom), shortly after the arrival of pulse at $250km$.

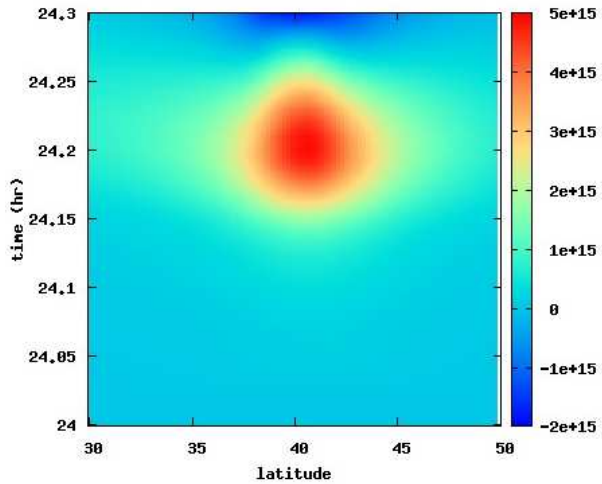
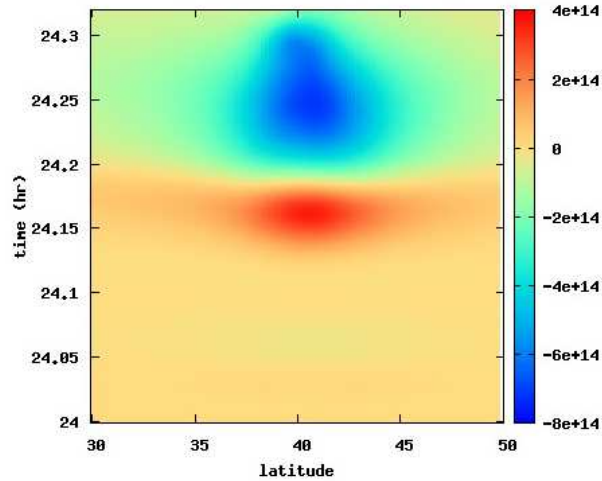


Figure 2.9: TEC perturbations as a function of geographic latitude ($glat$) associated with the compressional mode for pulses P_1 (top) and P_2 (bottom).

Chapter 3

Modeling of in situ Langmuir Probe measurements

Langmuir probes were the first in situ instrument carried by sounding rockets and satellites to measure the plasma density and temperature in space. The interaction between the space plasma and the probe affects the measurements. Several numerical models have been developed to simulate spacecraft plasma interaction in order to understand the physical factors that play an important role in the measurements made with these probes. The present study is based on the modeling of the current characteristics of the DEMETER Segmented Langmuir probe (SLP) under different ionospheric plasma conditions. The chapter starts with an overview of basic technique involved in the operation of the Langmuir probe and the background studies. Then we describe the geometry of the SLP that is under consideration. Finally, simulation results are presented.

3.1 Langmuir Probe Technique

Langmuir probes are widely used diagnostic instruments for both laboratory and space plasma. The technique consists of exposing an electrode to plasma

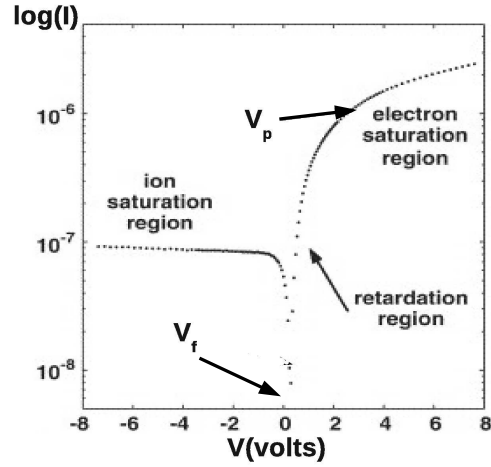


Figure 3.1: Typical I-V curve of a Langmuir probe illustrating the ion current, electron retardation and electron saturation current regions. In the figure V_f is the probe floating potential and V_p , the plasma potential, corresponds to the inflection point in the I-V curve. Reprinted from Lebreton, J.P., 2009 [57].

and measuring the collected current as a function of the bias voltage. By performing several measurements at different bias voltages, a current-voltage graph or characteristic curve is produced. The resulting characteristic curve of the probe is used to infer information about plasma parameters, for example the plasma density, temperature, plasma potential and the floating potential [44, 45, 59, 69]. For example a typical current characteristic of a Langmuir probe is shown in Figure 3.1. The current characteristic is divided into three distinct regions according to the plasma potential (V_p) and the floating potential (V_f). These are the following:

Ion Saturation Region When the probe is biased to a large negative voltage; i.e., $V \ll V_f$, all the electrons in the vicinity of the probe are repelled. As a result the current collected by the probe consists of ions with negligible

contribution from the electrons. This branch of the I-V curve is called "ion saturation region".

Floating Potential The floating potential (V_f) is the voltage at which the net current collected by the probe is zero; i.e., $J_i + J_e = 0$ where J_i and J_e represent the ion and electron current densities respectively.

Plasma Potential The plasma potential or space potential (V_p) is the voltage at which no sheath exist around the probe. A sheath is the region in which the quasineutrality of the plasma surrounding the probe is violated and the space charge density in this region is given by: $\rho = e(n_i - n_e)$. However, at $V = V_p$ the space charge density vanishes which implies that $\rho = 0$.

Retardation Region It is the current collected by the probe when it is biased to a potential which is greater than the floating potential and smaller than the plasma potential; i.e., $V_f < V < V_p$. As the potential of the probe increases beyond V_f the probe attracts more electrons than ions. For Maxwellian electrons the current in this region increases exponentially and can be approximated with the following relation:

$$I_e = n_o e A_p \sqrt{\frac{k_B T_e}{2\pi m_e}} e^{\frac{e(V-V_p)}{k_B T_e}}. \quad (3.1)$$

Here, I_e is electron current, A_p is the area of the probe, k_B is the Boltzmann constant, m_e is the mass of an electron and T_e is the electron temperature. The semilogarithmic plot of current vs. bias voltage gives a straight line. The slope of the straight line is given by $\frac{e}{k_B T_e}$ and it is used to infer the value of the electron temperature T_e .

Electron Saturation Region When the probe is biased to a potential which is greater than the plasma potential; i.e., $V > V_p$, the probe attracts

electrons and repel ions. It leads to the current branch on the I-V curve which is known as "electron saturation region" [46, 52].

3.1.1 Sheath impact on Langmuir probe measurements

When a probe is immersed in a plasma, it perturb the local plasma. Charged particles in the plasma redistribute themselves in order to shield the perturbing electric field induced by the probe. The shielding causes the breakdown of charge neutrality and a net charge density $\rho = e(n_i - n_e)$ exists around the probe. A strong potential drop between the probe and the plasma is confined to the small non neutral region. This region is called a "sheath" and its thickness is of the order of few Debye length (λ_D). The formation of the sheath around a negatively biased probe and the variation in the plasma density is illustrated in Figure 3.2. It can be seen that the sheath is accompanied by a presheath region which consists of a shallow potential drop. The pre sheath is a transition layer between the neutral plasma and the sheath in order to maintain the continuity of the ion flux. It is quite obvious that the Debye length λ_D depends only on the plasma parameters; in particular, on the density (n_o) and the electron temperature (T_e). It does not depend the biasing of the probe. The electrostatic sheath around the probe, however, strongly depends on the biasing voltage; that is, the sheath size varies with the bias voltage. In a collisionless plasma, the current collected by the probe is affected by the thickness of the sheath. There are two limiting cases for a sheath surrounding the probe in the plasma e.g., a thin sheath and a thick sheath.

Thin Sheath A thin sheath is formed around the probe (spherical or cylindrical), when the Debye length is much smaller than the radius of the probe; i.e., $\lambda_D \ll a$. In this case the planar probe approximation is sufficient to describe the current collected by the probe. In a thin sheath approximation, the effective probe area and the geometrical probe area are same.

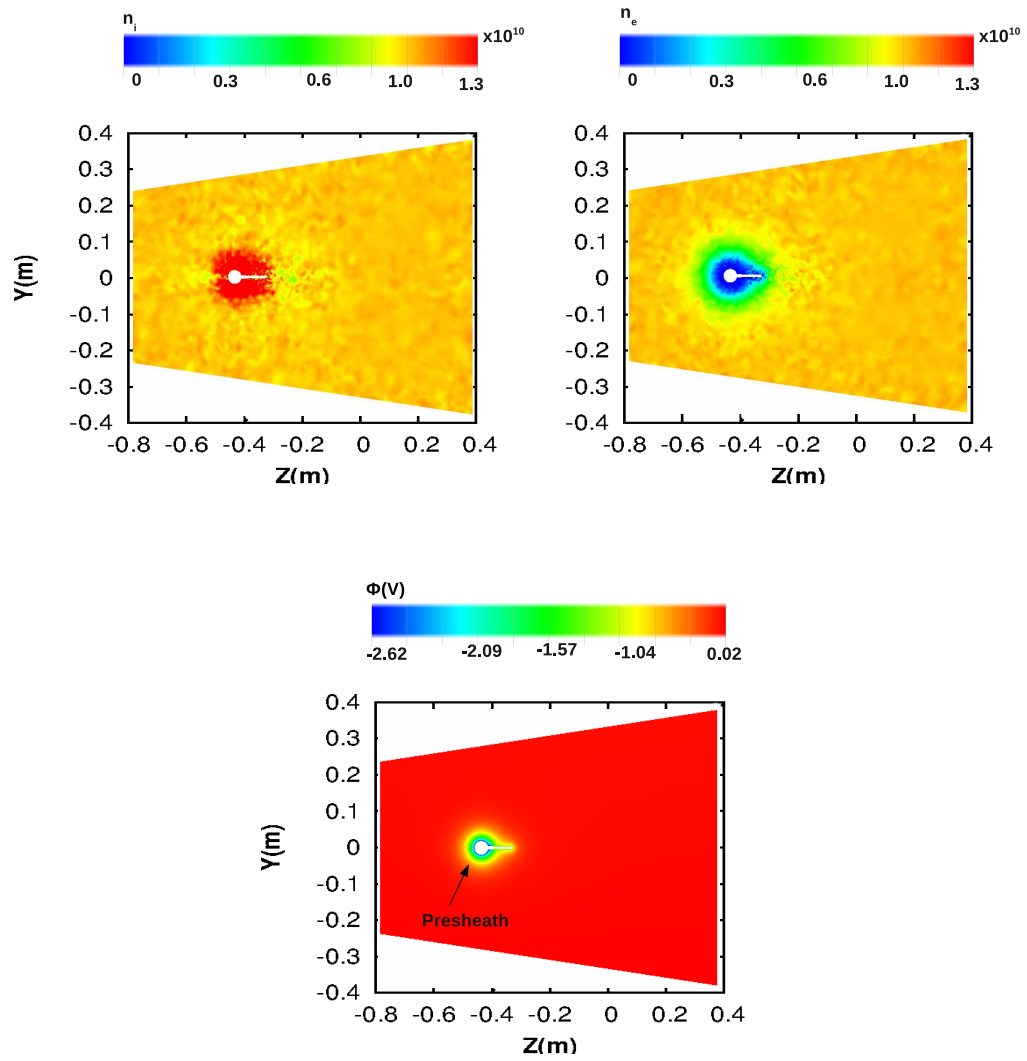


Figure 3.2: Illustration of the ion density (top left), electron density (top right) and the sheath potential (bottom) around a Langmuir probe.

Thick Sheath A thick sheath is formed around the probe (spherical or cylindrical), when the Debye length is larger than the radius of the probe; i.e., $\lambda_D \gg a$. In thick sheath approximation, the orbits of the charged particles play an important role and their motion can be described by the Orbital Motion Limited (OML) theory. According to this theory, the current collected by the probe depends on a critical impact parameter b_c which corresponds to the orbits of the particles that hit the probe at grazing angle. Particles with trajectories with an impact parameter smaller than b_c ; i.e., $b \ll b_c$ will hit the probe and contribute to the collected current. Particles with trajectories such that $b \gg b_c$, on the other hand, will not hit the probe and therefore, not contribute to the collected current. These three scenarios are illustrated in Figure 3.3. In a collisionless sheath, the critical impact parameter (b_c) can be obtained by solving the energy and the angular momentum conservation equations. The resulting expression for b_c is given by [66]:

$$b_c = a \left(1 - \frac{q\phi(a)}{W_o} \right)^{\frac{1}{2}}. \quad (3.2)$$

Here, q is the charge, $\phi(a)$ is the potential at the surface of the probe and $W_o = 1/2m_i v_i^2$, is the kinetic energy of the ions. Eq. 3.2 shows that the critical impact parameter depends on the electrostatic potential energy and the kinetic energy of the particles. The attractive potential for ions; i.e., ($\phi(a) \ll 0$) leads to a value of b_c which is larger than a . Therefore, in the thick sheath approximation the effective probe area is larger than the geometrical probe area for the attracted species [64, 66].

3.2 Background Studies

Early theoretical studies have been devoted to investigate the current characteristics of symmetrical probes, such as cylindrical, spherical and planar

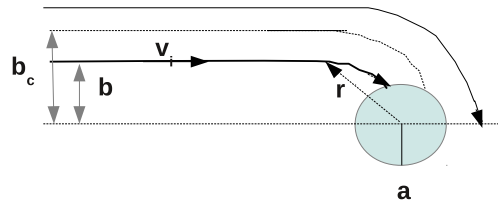


Figure 3.3: Illustration of different trajectories of the ions in thick sheath.

probes. Mott-Smith and Langmuir proposed equations to derive the velocity distributions directly from the I-V curves of spherical and cylindrical probes in drifting Maxwellian plasma [61]. Hoegy and Brace studied the response of planar, cylindrical and spherical Langmuir probes in isotropic and anisotropic non-Maxwellian plasma. They found that for isotropic distributions, the saturation current is temperature independent for cylindrical probes whereas, it is highly temperature dependent for the planar and spherical probes. Their study also showed that for isotropic plasma, these three geometries are equally suitable for the ionospheric electron density and temperature measurements. For anisotropic distribution, however, these three probe geometries are not equally suitable for the measurement of ionospheric plasma parameters [51]. El Saghir and Shanon presented integral relations for obtaining the electron energy distribution functions for different Langmuir probe geometries [67]. For ionospheric measurements, Langmuir probes have been widely used on satellites or rockets to measure electron and ion densities, temperatures and flow velocities, as well as spacecraft floating potentials in ionospheric and magnetospheric plasma. Many authors analyzed Langmuir probe measurements in the ionosphere to understand different physical phenomena. For example, Olson et al., 2010 applied a simple analytical probe-in-sheath model to the Langmuir probe data from the Cassini spacecraft to study the spacecraft sheath effects on the current characteristics of the probe [63]. Piel et al., 2001 studied the influence of the geomagnetic field and probe contamination on plasma diagnostics with Langmuir probes in the equatorial ionosphere [65]. Some numerical models were also developed for the detailed description of Langmuir probes. For example, Hilgers et al., 2008 presented numerical results of SPIS simulations of spherical and cylindrical Langmuir probe geometries in a regime in which the OML approximation is expected to be valid [50]. The numerical results of their study are in good agreement with theoretical predictions by Laframboise and the Orbit Motion Limited (OML) theory [55, 56]. Recently, the use of

directional Langmuir probes to measure plasma flow velocity, and understand the dynamics of laboratory and space plasma has received special attention. Nagaoka et al., 2000 demonstrated experimentally and theoretically the measurements of the plasma flow velocity by using directional Langmuir probe under weakly ion-magnetized conditions [62]. Lebreton et al., 2002 designed a DEMETER Langmuir probe experiment, also called ISL, for in situ measurements of ionospheric plasma parameters. The ISL instrument consists of two sensors: a cylindrical Langmuir probe (*LP*) and a spherical segmented Langmuir probe (*SLP*). In their study, Lebreton et al. gave a brief description of the ISL instrument design, its in-flight operation and data analysis techniques [57]. Seran et al, 2005 developed a particle in cell (PIC) model to investigate the capabilities of the SLP to diagnose bulk plasma parameters[68]. Their model, however, do not account for the complete geometry of the SLP (stem and post). The small stem is also a part of the guard electrode and collects some current. Therefore, the total current collected by the guard electrode will be larger than that it is computed without small stem. They did not include the electron current branch which corresponds to the positive biasing of the SLP. For given plasma parameters the electrons are slightly magnetized and show sensitivity to the orientation and magnitude of the magnetic field. As a result the electron current branch of various segments show variation with the magnetic field. The detailed analysis of this effect is included in my model.

3.2.1 Goal of this Study

The goal of the present study is to simulate the current characteristics of the DEMETER SLP. For this purpose, we used PTetra which is capable of simulating the time dependent interaction of satellites with space plasma [58]. The numerical results of the present study show some interesting features. These include: the angular anisotropy in the current collected by various collectors, the sensitivity of the electron current to the orientation of the magnetic field

and the enhancement in the ion current due to the presence of the minority light H^+ ions.

3.3 The DEMETER Segmented Langmuir Probe (SLP)

The SLP is part of the scientific payload of a French micro satellite, DEMETER. A complete description of the segmented Langmuir probe is given by Lebreton et al., 2006 [57]. The SLP is part of the ISL instrument that comprises two Langmuir probes: a cylindrical Langmuir probe and the SLP as shown in Figure 3.4. DEMETER was used as a flight demonstrator for the SLP. The cylindrical Langmuir probe was regularly used to measure bulk parameters of the ionospheric plasma, while the SLP was only used occasionally, as the primary objective was to characterize its performance in different plasma conditions encountered during the DEMETER mission. The SLP consists of a spherical probe with its surface divided into seven independent collectors; six spherical segments each of radius 0.5cm and a guard electrode. The guard electrode consists of a sphere of radius 2cm and a small cylinder (1.5cm in length, 6mm in radius). The six segments are electrically insulated from each other and from the guard electrode, but all components of the SLP are kept at the same potential. They are positioned around the sphere at different angles with respect to one another. The orientation of the segments around the sphere is illustrated in Figure 3.4. Segment S_2 is aligned with the satellite velocity (along Z-axis in the ram direction). Other segments S_1 , S_3 are located symmetrically at an angle of 45° , S_4 , S_5 and S_6 are at an angle 90° with respect to the ram direction. The probe is mounted on a post of 6cm in length and 4mm in radius. On DEMETER, this post is grounded with respect to the spacecraft body. In the simulations, it is used as a reference with respect to which the probe bias is determined. The I-V characteristics are obtained by applying the

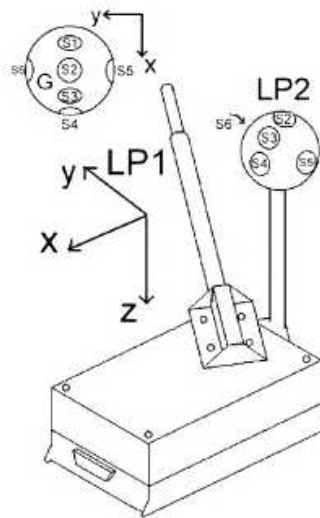


Figure 3.4: Segmented Langmuir probe (top) and illustration of the various segments (bottom). Reprinted from Lebreton, J.P., 2006 [57].

same potential to all seven collectors and measuring the current collected by each segment individually.

3.4 Numerical Approach

A three dimensional particle-in-cell (PIC) code PTetra, is used to simulate the current-voltage characteristics of the probe [58]. The model is based on a fully kinetic description of all plasma species with physical charges and masses. The

model accounts for a uniform and constant background magnetic field. It also accounts for several phenomena of physical importance in the spacecraft interaction with the plasma. These include satellite charging, photoelectrons and secondary electrons emission. For low Earth orbit (LEO) satellites (at altitude range 100 km to 1000 km, in the ionosphere), the impact of the secondary electrons is not significant. However, photoemission can affect the current collection of the sunlit area which eventually depends on the solar angle. In this study, the effect of photoelectrons was assessed by comparing the characteristics computed with and without photoemission. The differences were found to be small ($<5\%$). A more rigorous analysis of photoemission effects would require the inclusion of a more complete description of the satellite geometry, such as the satellite body and the solar panel. PTetra uses a standard PIC approach, in which simulation particles, or macro particles, represent many physical particles. In addition to charge and mass, each macro particle also carries a statistical weight corresponding to the number of physical (real) particles that it represents. In this study, 10^8 macro particles are used in the simulation domain, to simulate the plasma near the probe. The mesh used in the study is unstructured with tetrahedral elements. It was generated with CUBIT [47] and it consists of 79861 vertices connected in 454950 tetrahedra. The resolution of the mesh varies in space in order to resolve the fine features near the probe. The size of largest elements in the simulation domain is 2cm and the smallest ones on the probe is 2.5mm. The outer boundary of the simulation domain is located sufficiently far from the probe for the boundary conditions to have a negligible influence on the simulation results. The equations of motion of the particles are solved by using the second order accurate leap frog method. The integration of these equations requires the knowledge of \vec{E} and \vec{B} fields. The magnetic field \vec{B} is calculated from the International Geomagnetic Reference Field (IGRF) model [53] by using the time and satellite position at which measurements were made. Poisson's equation is solved

Table 3.1: Physical parameters assumed in the reference simulation, corresponding to DEMETER orbit 06911-0 at 8:16 UT

Physical parameter	Value
Electron density	$1.3 \times 10^{10} \text{ m}^{-3}$
Plasma temperature	0.3 eV
Magnetic field (\vec{B}_o)	$(40.68, -1.257, -6.787)\mu\text{T}$
Plasma Flow velocity (v_d)	$(0, 0, 7500) \text{ m/s}$
Altitude	712 km
Geographic latitude	70.76°N
Geographic longitude	54.40°
Majority ions	78%O ⁺
Minority ions	22%H ⁺
Debye Length	0.035m
Electron thermal velocity $v_{the} = \sqrt{\frac{2k_B T_e}{m_e}}$	324.8km/s
Electron thermal gyro radius	0.042m
Hydrogen Ion thermal velocity $v_{thH} = \sqrt{\frac{2k_B T_i}{m_H}}$	7.6km/s
Oxygen Ion thermal velocity $v_{thO} = \sqrt{\frac{2k_B T_i}{m_O}}$	1.9km/s
Ion thermal gyro radius	5.4m

as a boundary value problem with Dirichlet boundary conditions [58]. The numerical solution of Poisson’s equations requires the volume charge density and the charge collected by each probe component. A collected current is specified on the probe, whereas the post is assumed to be floating. Note that, other than the post and the spherical probe, our simulations do not account for the other components of the satellite. If the entire spacecraft were included in the model, the negative of the current imposed on the probe would also have to be imposed on the rest of the satellite in order to ensure current balance. In such a case the post would only be collecting a small fraction of that current, owing to its small surface area compared to that of a spacecraft body. This is why the post, used as a satellite ground proxy, is assumed to be collecting zero net current. The imposed probe collected current is varied in such a way as to produce a potential difference with the (grounded) post ranging from -5V to $+5\text{V}$. The simulation parameters used in our analysis and summarized in Table 3.1 correspond to DEMETER measurements along day side orbit 06911-0.

3.5 Results and Discussion

In this section the computed characteristics of the SLP and their comparison with DEMETER satellite measurements is presented. Four simulation cases are considered to study the influence of different physical phenomena on the current collection of the SLP. These are:

- A reference case, corresponding to the plasma composed of 22% H^+ and 78% O^+ ions with a magnetic field obtained from the IGRF [53].
- A case in which the plasma is stationary. It shows the sensitivity of the collected current to the plasma flow velocity.
- A plasma with 100% O^+ ions. This case is presented to show the effect of light (H^+) and heavy (O^+) ions on the ion current branch of the SLP.
- A case in which the magnetic field is varied in magnitude and direction with respect to the reference magnetic field (\vec{B}_o). This is done to illustrate the sensitivity of the collected electron current to the orientation and the magnitude of the magnetic field.

The simulation results obtained for these four cases are compared with in-flight DEMETER satellite measurements. Two sweeps are presented for the measurements: a short duration (fast) and a long duration (slow) sweep. These two sweeps are explained by Lebreton et al., 2006 [57]. The data acquisition times for the fast and the slow sweeps are 0.25s and 2s respectively. Each sweep consists of two parts: an up (negative to positive) and a down scan (positive to negative). In Figure 3.5, 3.7 and Figure 3.8, the fast up scans (thick solid line) are followed by the fast down scan (broken line), and the slow up scans (thin solid) are followed by slow down scans (broken thin line). It is noted that the up and down scans for both sweeps show hysteresis. The difference between the I-V curves for the up and the down sweeps is used to estimate the surface properties of the probe, and in particular to characterize the thin layer

due, for example, to surface contamination, or perhaps to a thin dielectric film of unknown origin, which is thought to be responsible for the hysteresis which varies with sweep speed. The characteristics of the properties of the layer and its influence on the determination of the plasma parameters is the subject of ongoing work (Lebreton, private communication).

3.5.1 Reference case

The reference conditions correspond to the plasma parameters given in Table 2.1. The composition of the ionospheric plasma for the LEO environment depends strongly on the altitude, latitude, local time and the solar activity. The ion composition on board DEMETER is obtained from the ion composition measurements of the Instrument d'Analyse du Plasma (IAP) [43]. The simulations are done with the same density of H^+ and O^+ ions as measured on DEMETER; that is, 22% H^+ and 78% O^+ . The current collected by the seven segments of the SLP as a function of bias voltage is computed with PTetra. The resulting characteristics in the range -5V to +5V are shown in Figure 3.5. The anisotropy in the ion current collected by the various segments shows that the segment S_2 (facing the ram direction) collects slightly more current than the other segments. The anisotropy in the collected ion current is mainly controlled by the direction of the plasma flow velocity, hence the segment facing the ram directly collects the largest current. The comparison of the reference simulation results (accounting for the H^+ ions) with DEMETER measurements shows good qualitative and quantitative agreement in both ion and electron current branch of the I-V curves. A proper calibration has been made for the I-V converter of the cylindrical probe and for seven I-V converters of the SLP prior to launch. The description of the calibration is beyond the scope of the present study. However, the post-flight calibration of the I-V converters has not been available yet. This could be the source of uncertainty in the ion current part of the I-V curve. It could also affect the electron part of the characteristic, but

it would likely be negligible. There are various physical factors that play an important role in the current collection of the SLP as for example, the plasma flow velocity, the ion composition of the ionospheric plasma, the attitude of the satellite and the orientation of the magnetic field. Numerically, it is straightforward to include each effect separately in order to assess its relative importance. The resulting variation in the current collected by the SLP is studied for the probe in a stationary plasma, in a plasma consisting of 100% O^+ ions, and in a scenario where the magnetic field points in a different direction to account for a possible error in the satellite attitude. These effects are considered below.

3.5.2 Sensitivity to the Plasma flow velocity

The plasma flow velocity modifies the current collected by the SLP. In the reference case, the magnitude of the plasma flow velocity is 7.5 km/s which is equivalent to the orbital velocity of the satellite. However, the orbital velocity of the satellite is in the $-Z$ direction and in the probe frame of reference, the plasma is drifting with the same speed in the opposite direction. The plasma drift velocity is 5 times greater than the O^+ thermal velocity (1.9km/s), and it is comparable to the H^+ thermal velocity (7.6km/s). The Mach number defined as the plasma drift velocity divided by the ion sound speed ($M = \frac{v_d}{c_s}$). The reference case leads to the Mach number which is approximately 5. Hence, the plasma flow is supersonic and a visible wake in the ion density is expected behind the probe in all cases with $M > 1$. The structure of the wake region is shown in Figure 3.6 for the weakly biased (+2V) and strongly biased (+5V) probe. It is observed that the size of the wake region and plasma sheath potential vary with the probe biasing. In order to determine the sensitivity of the I-V curves to the plasma flow velocity, the simulations are repeated for the SLP in the stationary plasma ($v_d = 0$) with Mach number $M = 0$. The effect of the ion flow velocity is assessed by comparing the simulation results obtained for a stationary plasma, with the measurements and with the simulation results

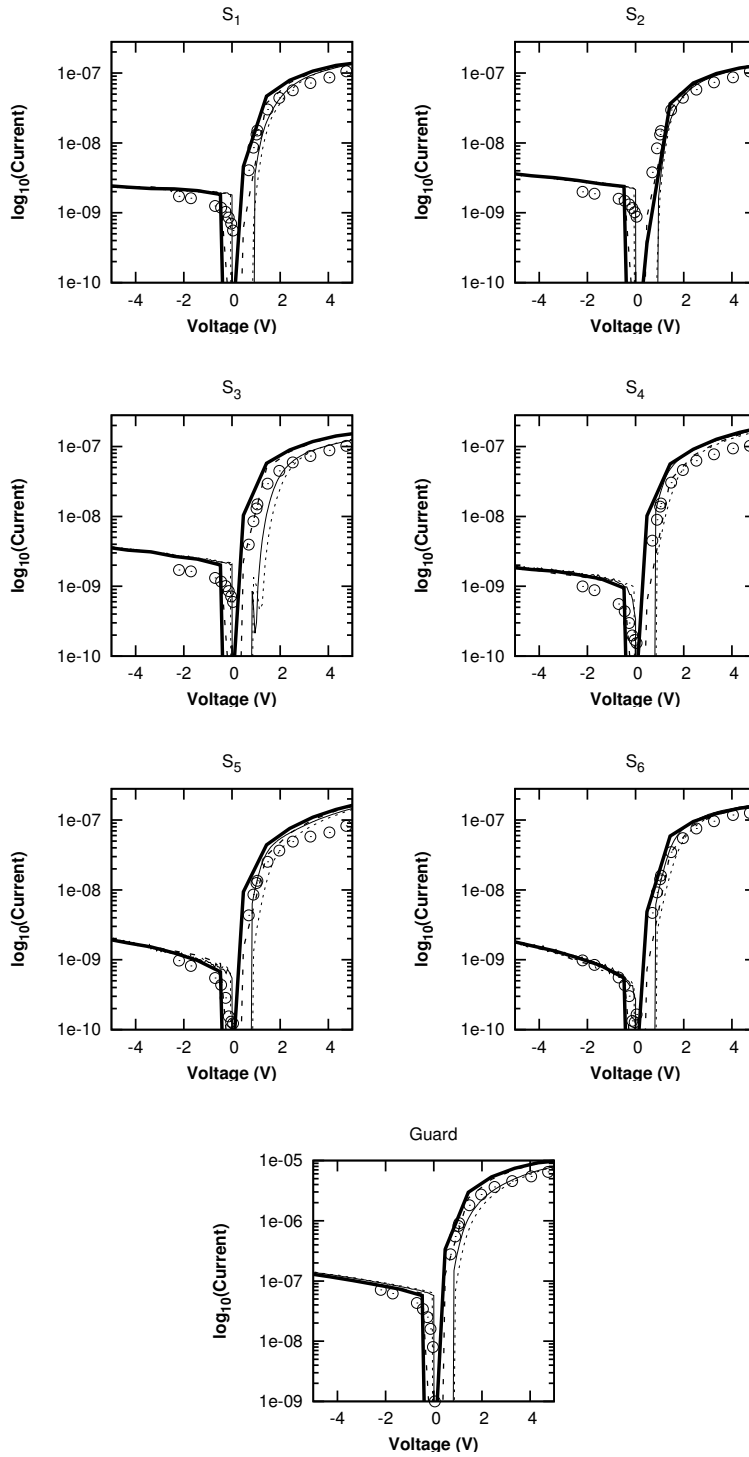


Figure 3.5: Comparison between the simulated and measured I-V curves for segments $S_1, S_2, S_3, S_4, S_5, S_6$ and the guard electrode. The thicker lines show the characteristics for the fast scan and thinner lines show the characteristics for the slow scan. In both cases the solid lines are for the up scan (negative to positive) and dashed lines for the down scan (positive to negative). Circles show the characteristics obtained from the reference case.

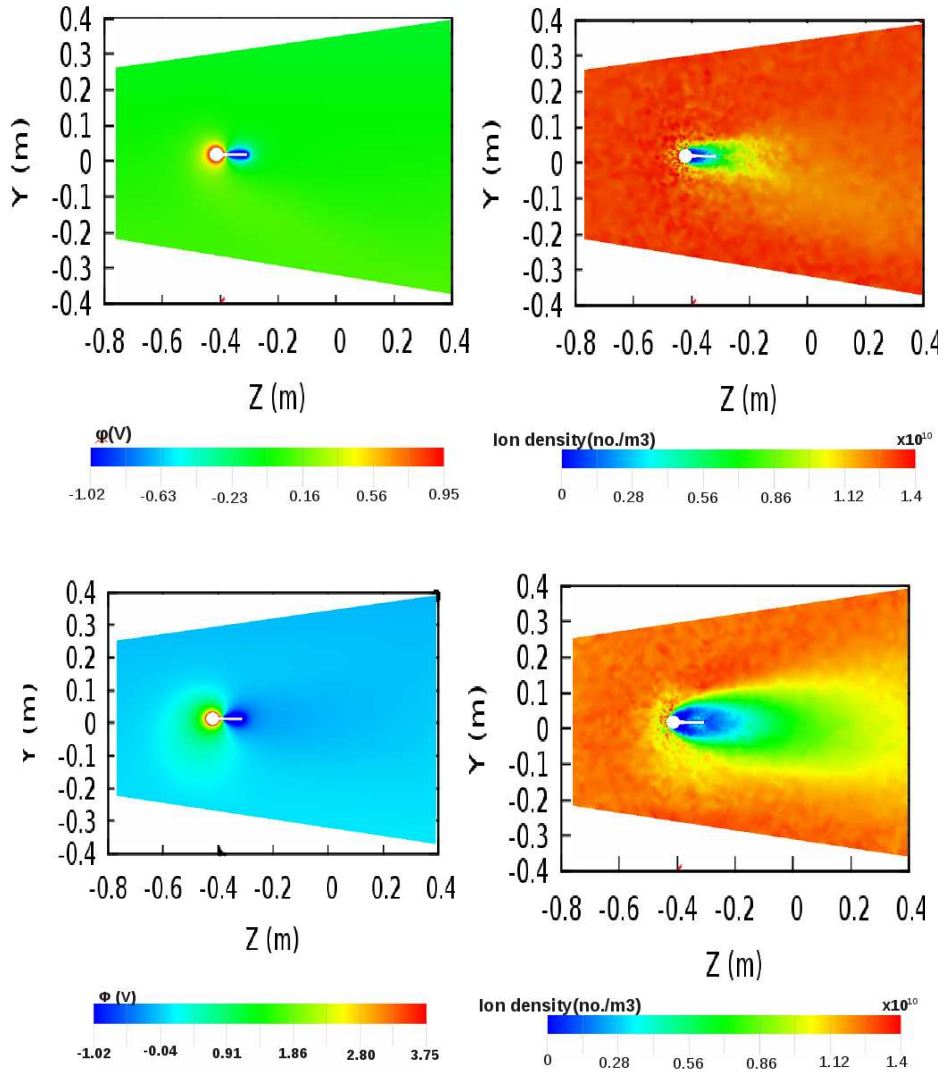


Figure 3.6: Profiles of the sheath potential (left) for weakly biased ($\sim +2V$) and strongly biased ($\sim +5V$) probe, and the corresponding wake in ion density behind the probe (right). Plasma is drifting in Z direction, whereas the orbital velocity of the satellite is in $-Z$ direction.

obtained for the reference case. The comparison is shown in Figure 3.7. The plasma drift velocity significantly affects the ion current branch of the I-V curves. It is found that the segments facing the ram direction (S_1, S_2 , and S_3) collect a large current and the segments facing the downstream region (S_4, S_5 and S_6) collect a small current when $M = 5$ compared to $M = 0$ case. The plasma drift velocity leads to a higher concentration of the ions in the upstream region and lower ion concentration in the downstream region. For a non drifting plasma, however, collected ion currents are nearly the same for all probe segments.

3.5.3 Ion mass and composition

The effect of ion mass and composition is assessed by comparing the simulation results obtained for a 100% O^+ plasma, with measurements and with simulation results obtained for the reference case. This comparison is shown in Figure 3.8. It is observed that the simulated I-V curves show qualitative agreement with measurements. Quantitatively, however, there are marked discrepancies in the ion current branch. It is found that in an assumed 100% O^+ plasma, the ion current collected in negative biasing is significantly less (by $\sim 36\%$) than that in the reference case. This decrease in the ion current can be understood from the Orbit Motion Limited (OML) theory of the spherical probes. In this case, the Debye length ($\lambda_D = 0.035\text{m}$) is greater than the probe radius ($a = 0.02\text{m}$) and the sheath around the SLP is thick. The motion of the ions in the thick sheath depends on the impact parameter as given in Eq. 3.2. The ions approaching the probe with distances exceeding the impact parameter (b_c) do not contribute to the probe current. Only ions which have approaching distances smaller than the impact parameter will contribute to the collected current. The impact parameter depends on the ratio of the probe potential to the bulk energy of the ions. The bulk energies of the H^+ and O^+ ions are 0.29eV and 4.7eV respectively. The corresponding impact parameter b_c of the H^+ ions is 3 times

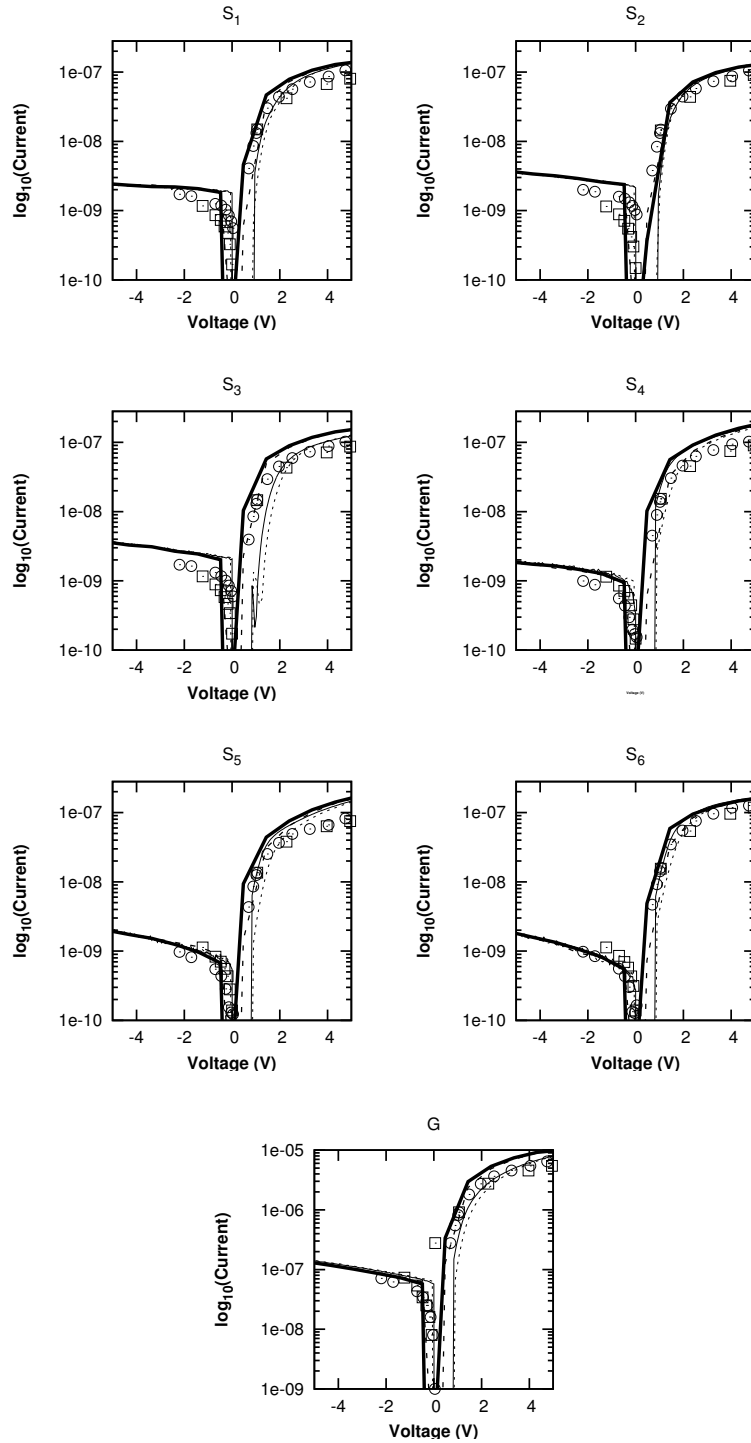


Figure 3.7: Comparison between the simulated and measured I-V curves for segments $S_1, S_2, S_3, S_4, S_5, S_6$ and the guard electrode. The measured characteristics and the reference case are the same as in Figure 3.5. Circles show the characteristics obtained from the reference case and Squares represent the characteristics obtained from the stationary plasma case.

larger than that of the O^+ ions. Therefore, the effective cross section ($\sigma=\pi b_c^2$) of H^+ is 9 times that of the O^+ ions. The resulting current collected by the probe immersed in a plasma made of 100% O^+ ions therefore, will be less than that of plasma containing lighter H^+ ions.

3.5.4 Sensitivity to the magnetic field

The magnetic field also affects the I-V curves of the SLP. In the reference case, the magnetic field $\vec{B}_o = (40.68, -1.257, -6.787)\mu\text{T}$ is obtained from the IGRF model. The angle between the \vec{B}_o and the Y-axis (normal to segments S_5 and S_6) is 88.23° which corresponds to an angle of $\sim 2^\circ$ with respect to the surface of the top segment. The reference \vec{B}_o is almost parallel (grazing) to segments S_5 and S_6 . In order to determine the sensitivity of the results to the orientation of the magnetic field, the simulations are repeated with a magnetic field $\vec{B}' = (29.17, 29.17, 0.78)\mu\text{T}$. The magnitude of \vec{B}' is the same as that of the reference magnetic field, but with a change in direction by $\sim 45^\circ$. Current characteristics are also computed with zero magnetic field. The resulting characteristics for the above mentioned two cases are compared with the reference simulation case and are illustrated in Figure 3.9. In this case, magnetization plays an important role in the interpretation of the I-V curves of the SLP. It is parameterized in terms of the ratio between the thermal gyro radius of a particle and the characteristic scale length of the system. If this ratio is small (≤ 1) particles are magnetized, otherwise they are unmagnetized. In our study, the scale length is characterized by the radius of the probe 0.02m, whereas the thermal gyro radii of electrons and O^+ ions are 0.042m and 5.4m respectively. Whence, electrons here are weakly magnetized and ions are effectively unmagnetized. Varying the orientation of the magnetic field by 45° has relatively little effect on most characteristics. In the absence of the magnetic field, however, the differences in the collected electron current are noticeable. It is observed that with zero magnetic field, the SLP simulated collected electron current is approximately

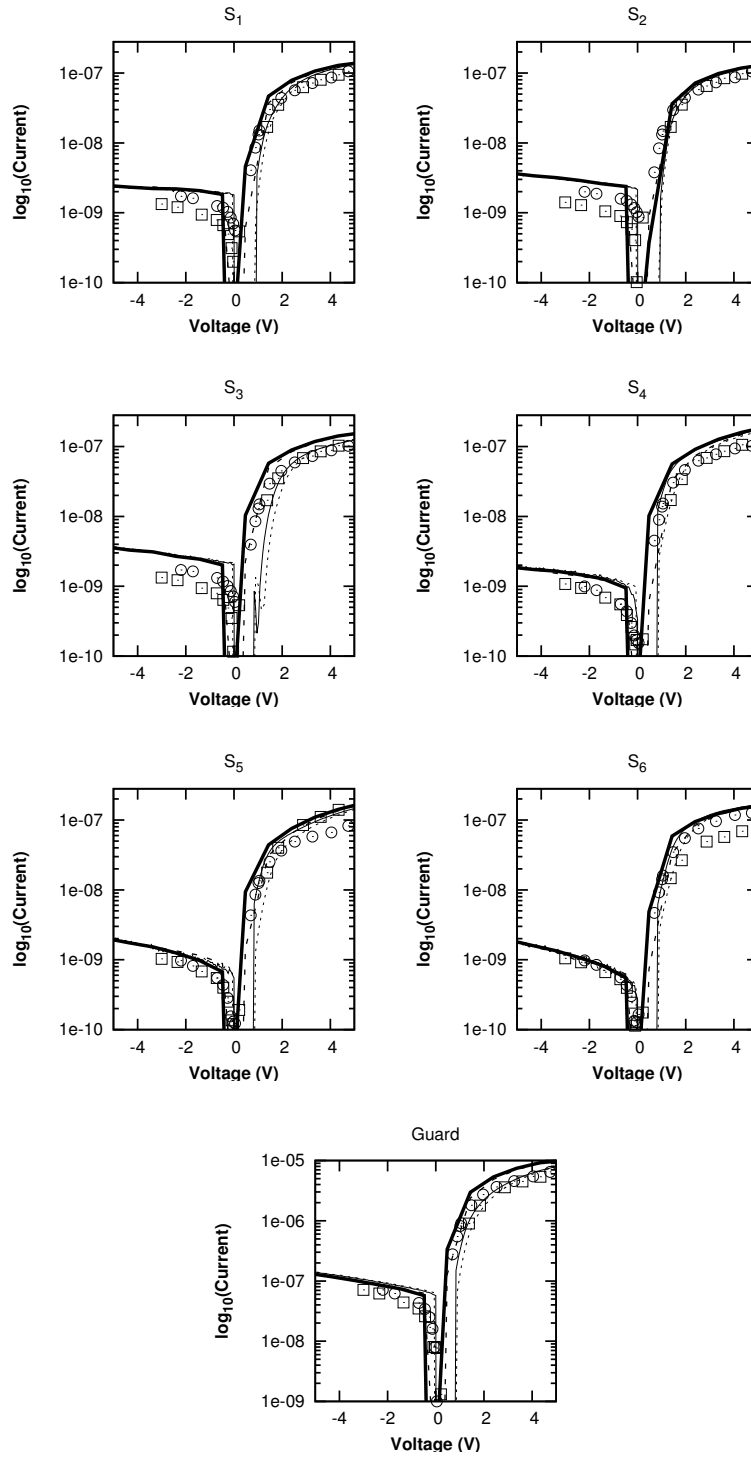


Figure 3.8: Comparison between the measured and simulated I-V curves for segments S_1 , S_2 , S_3 , S_4 , S_5 , S_6 and the guard electrode, showing the effect of the ion composition. The measured characteristics and the reference case are the same as in Figure 3.5. Circles represent the characteristic obtained with the reference case and squares show the characteristics computed with 100% O^+ ions.

twice the value computed in the reference case.

3.6 Summary

The PTetra numerical model is well adapted to compute the current characteristics of a segmented Langmuir probe, which is part of the scientific payload of the DEMETER micro satellite. Four cases were considered to study the sensitivity of the I-V curves: The first one serves as a reference with respect to which the other two cases are compared. The second case looks at the effect of the ion mass composition, and the third case shows the sensitivity of the electron collected current to the magnetic field. PTetra simulation results are compared with DEMETER measurements along a day side orbit. The comparison shows good qualitative agreement in all cases. In the reference case, that accounts for 78% O^+ and 22% H^+ , the collected current is comparable of the measured current with some minor differences. There are several physical factors at play in the current collection of the SLP. These include: the ionospheric plasma composition, the magnitude of the plasma drift velocity, the strength and orientation of the magnetic field. A quantitative assessment of these effects was made by carrying out simulations in which each effect was taken into account separately. The high mobility of the H^+ ions leads to a significant contribution in the ion collected current when the probe is negatively biased. The probe collects 3 times more ion current compared to the computed collected currents in an assumed 100% O^+ plasma. The plasma drift velocity affects the current collected by the SLP and in particular, the ion current branch. The moderate magnetization of the electrons causes the electron current branch to be sensitive to the presence of the magnetic field. In the absence of a magnetic field, there is a significant increase in the electron current collected by all segments compared to the reference case. However, the magnetic field does not affect the ion current branch. This is due to the fact that collected electrons, even

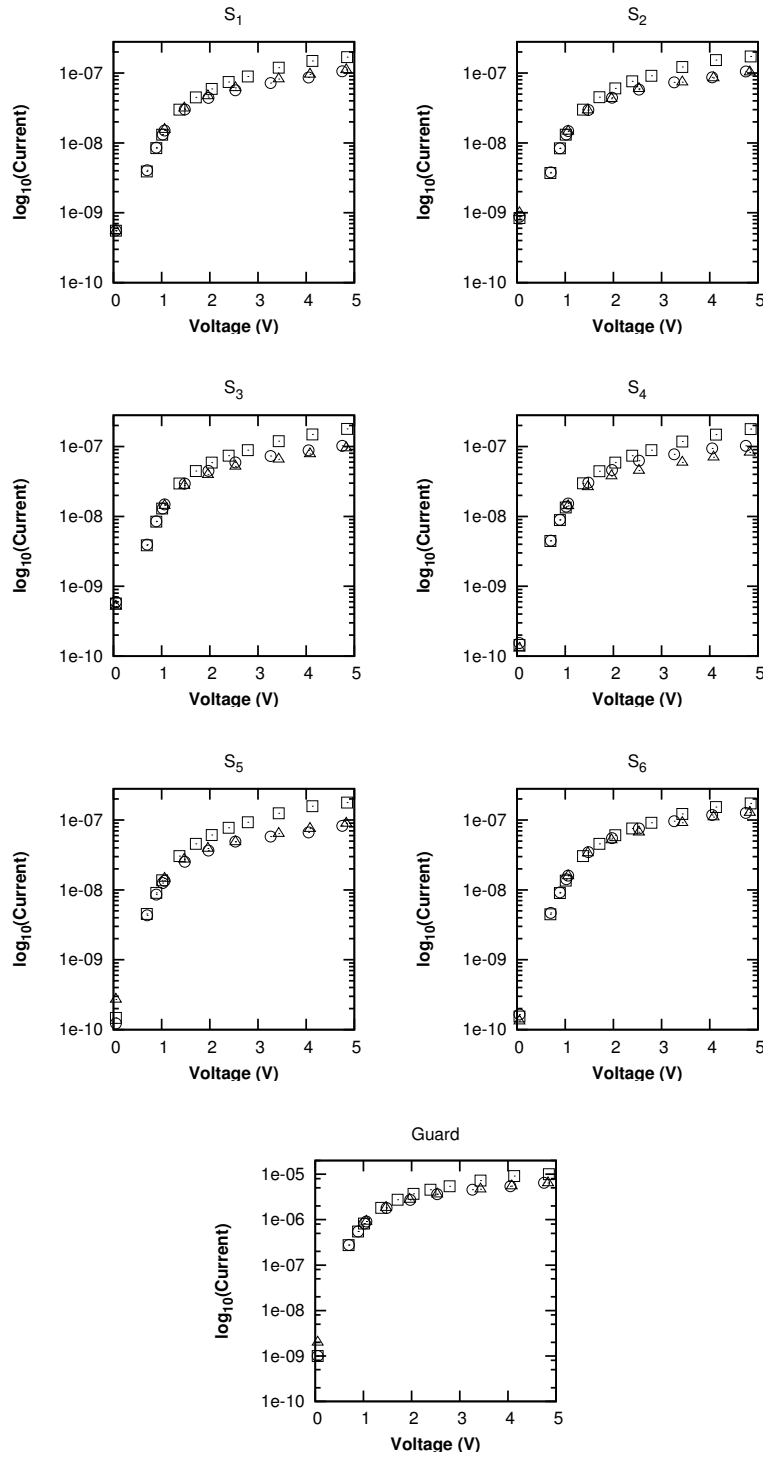


Figure 3.9: Simulated I-V curves for segments $S_1, S_2, S_3, S_4, S_5, S_6$ and the guard electrode, showing the effect of the magnitude and the orientation of the magnetic field. Circles show the reference case and triangles represent the characteristics obtained with the magnetic field (B') at an angle of 45° with respect to the surface of the top segment. Squares show the characteristics computed without magnetic field.

when weakly magnetized, are constrained to come from the magnetic flux tube of radius equivalent to the electron thermal gyro-radius ($\sim 4\text{cm}$). When $B=0$, on the other hand, the collected electrons come from all directions without any constrained on their motion and contribute significantly to the electron current branch. The best agreement with the measurements is obtained with the reference case, which accounts for the magnetic field and the plasma made of 78% O^+ and 22% H^+ ions as measured on DEMETER. The effects considered in this study, therefore, need to be taken in to account in the interpretation of the I-V curves of a Segmented Langmuir probe.

1

¹”A version of this chapter has been published. Imtiaz, N., Marchand, R., and Lebreton, J.P.; Modeling of current characteristics of segmented Langmuir probe on DEMETER, Phys. Plasmas, 20, 2013.”

Chapter 4

Test Particle modeling of the JOULEII Suprathermal Ion imager

In this chapter, test particle modeling of a low energy particle sensor called Suprathermal Ion Imager (SII) is described in detail. It mainly covers the preliminary results of SII along with their comparison with the rocket based measurements in the high latitude ionosphere (auroral region). These measurements are obtained from the JOULE-II sounding rocket campaign. This chapter starts with an overview of the JOULE-II mission and instrumentation.

4.1 Introduction

Particle sensors have been widely used on satellites and sounding rockets to provide in situ measurements of space plasma, including particle velocity distribution functions. For example, Hundhausen et al., 1967 investigated the use of particle analyzers to measure two dimensional ion velocity distribution in the solar wind plasma [72]. Measurements of three dimensional particle velocity distributions in the magnetosphere are also reported by several authors [71, 76, 78].

Recently, these sensors have been used on many satellites that are operational or scheduled for launch. For example the three Swarm satellites, a European space Agency mission scheduled for launch in 2013 will carry an Electric Field Instrument (EFI) consisting of two Thermal Ion Imager (TIIs). Particle sensor measurements are known to be affected by the interaction between spacecraft instruments and ionospheric plasma. The main factor here is the electrostatic sheath and the wake formed around the spacecraft and on board instruments. Theoretical and computational studies have been presented to analyze these effects. For example, Olson et al., 2010 used a particle in cell (PIC) approach to investigate the evolution of the sheath potential profiles around the Cassini spacecraft. They found that the plasma parameters, in particular, the drift velocity and the temperature affect the wake region and make the spacecraft potential less negative [77]. Yang et al. 2010 used SPIS to understand wake effects on the sheath region around DEMETER [81]. Marchand et. al., 2010 used PIC and test-particle modeling to study the electrostatic sheath effects on the measurements of the Swarm Electric field instrument. They observed that the aberrations associated with finite sheath effects were less with the heavy O^+ ions than with light H^+ ions [75]. Rehman et al., 2012 extended this study by including the effect of geomagnetic field on the particle distributions in the vicinity of the Swarm Thermal Ion Imager (TII) [79]. The Suprathermal particle imager which measures the two dimensional distribution functions of low energy particles was first tested in flight on GEODESIC. This sounding rocket was launched by the Canadian space agency (CSA) on February, 2000 with the objective of making high-time-resolution measurements of core electrons ($0 - 10eV$) and ions ($0 - 50eV$) [73]. Similarly, the Suprathermal Ion Imager (SII) was also used on NASA sounding rocket 36.234 as a part of JOULE II mission. The main objective of the Joule II mission was to study the Joule heating in the ionosphere. The rocket was launched during an active aurora above Fairbanks Alaska in January 2007. Some studies have been devoted to

analyze the rocket data and its comparison with ground based measurements. Sangalli et al, 2009 analyzed rocket based measurements of the ion flow velocity, the electric and magnetic fields. From these measurements, they calculated the Joule heating rate and the height integrated profiles of Pedersen and Hall conductivities for a moderately active substorm [80]. Burchill et al, 2012 presented rocket 36.234 and Poker Flat Incoherent Scatter radar (PFSIR) data to investigate ionosphere-thermosphere (IT) coupling. Their study was based on the measurement of the ratio of the ion cyclotron frequency to the ion neutral collision frequency. From measured ion fluxes, they observed that the particles detected in the sensor had energies above $2eV$, which led to higher ion temperatures than expected. Their observation is consistent with the negative floating potential of the payload [70].

4.1.1 Motivation

The goal of this study is to understand the ion temperature measurements predicted by Burchill et al. [70]. From measured ion fluxes, they observed that the particles detected in the sensor after accelerated through the sheath had energies above $2eV$, as shown in Figure 4.1. As a result the predicted ion temperature was higher than expected. In an attempt to elucidate this discrepancy the interaction between the Suprathermal Ion Imager (SII) and ionospheric plasma is simulated to assess the impact of the sheath on ion measurements in the E-region ionosphere. This is done by first calculating the electric sheath surrounding the SII sensor and then by computing the particle velocity distribution functions and ion fluxes at the entrance of SII sensor. The distribution functions are then used to inject particles in the sensor aperture and tracking them down to the micro channel plate (MCP) consisting of a 32×32 array of detectors. For this purpose, a combination of particle in cell (PIC) and test particle simulation techniques is used. The PIC code is used to compute the electrostatic sheath potential around the SII sensor, and the float-

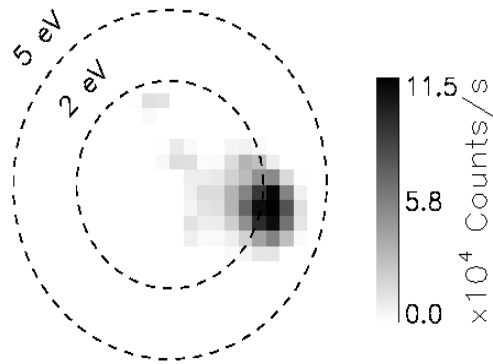


Figure 4.1: Illustration of the ion flux on MCP at $T = 294.36s$. The inner and outer circle represent the kinetic energies $2eV$ and $5eV$ respectively. The signal peak is outside the inner circle. Reprinted from Burchill et al., 2012 [70].

ing potential of the payload and the boom. The electrostatic sheath potential profiles are used to compute the particle velocity distributions around the SII sensor by using a backward Liouville approach. These velocity distributions are further used to inject particles into the sensor to calculate the particle fluxes on to the MCP by using a forward Liouville approach. The numerical results of the present study show some interesting features. As expected, the particle velocity distributions are stronger when the plasma flow velocity lies in the direct field of view of the SII aperture. Also the orientation of the plasma flow velocity with respect to the boom affects the ion fluxes significantly.

4.2 The Suprathermal Ion Imager: SII

The Suprathermal Ion Imager (SII) is part of the scientific payload of NASA sounding rocket 36.234 (series of Joule II mission). A complete description of the sensor is given by Knudsen et al. 2003 [73]. It is summarized here for completeness. The SII sensor consists of a cylinder of length 12cm and radius 1.9cm , which is mounted at the end of 1m long boom. The sensor skin is biased to -1.9V with respect to the payload floating potential in order to attract ions. The payload carried several instruments including the SII sensor to measure ion energy distribution functions. The illustration of the payload with SII sensor affixed on a boom, its coordinate system and the orientation of the ambient magnetic field \vec{B}_o are given in Figure 4.2 (top). The payload spins with a period of 1.6s around its rotation axis, which is aligned to within few degrees with the geomagnetic field vector (\vec{B}_o). The inner domain of the SII sensor is composed of two concentric hemispheres with a relative bias of -25V between the inner and outer shell. The electric field between the two shells is directed radially inward. The radii of the inner and outer hemispheres are 10.5mm and 14mm respectively. Ions enter through the small aperture in the outer hemisphere. They are deflected radially inward by the electric

Table 4.1: Plasma parameters assumed in the simulation, corresponding to altitude $150km$

Physical parameter	Value
ram velocity (\vec{v}_d)	$(-118.63, 985.78, 639.12)$ m/s
Ambient magnetic field (B_o)	5.33×10^{-5} T
Electron density (n_e)	4.83×10^{10} no./ m^3
Electron temperature (T_e)	600.2 K
Ion NO^+ density (n_{NO})	2.76×10^{10} no./ m^3
Ion O_2^+ density (n_{O_2})	2.07×10^{10} no./ m^3
Ions temperature ($T_i = T_e$)	600.2 K

field, they pass through a meshed window in the inner hemisphere and reach a field free region within the inner hemisphere. Particles with higher kinetic energy are deposited at large distances from their entry point compared to the lower energy particles. Ion fluxes are amplified by using a micro channel plate and the signal is tranfered to a fiber optic imaging bundle. These images are recorded by 256×256 pixel charge couple device (CCD) [70, 80]. The inner view of the SII sensor is also illustrated in Figure 4.2 (bottom).

4.3 Model Description

Kinetic modeling based on two different numerical techniques is used to simulate the measurements made by particle sensor SII. These are the following:

4.3.1 PIC Modeling

The three dimensional PIC code used here is PTetra. A detailed description of the code is given by Marchand, 2012 [58]. It is summarized in Chapter3. The code uses unstructured adaptive meshes to represent complex structures. The mesh used in the study is unstructured with tetrahedral elements. It is generated with GMSH. The simulation parameters used in the analysis are given in Table 4.1. The ram velocity of the rocket payload is mainly along -Y direction; i.e., downward along the payload axis. In the payload frame,

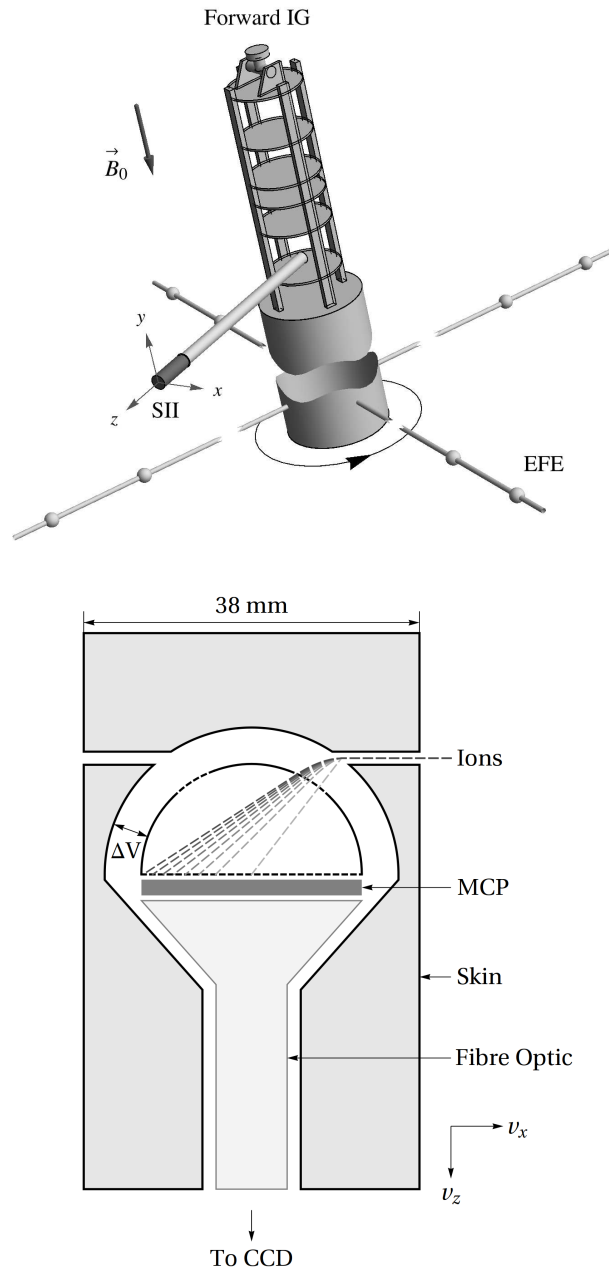


Figure 4.2: Joule payload (top) and illustration of Suprathermal Ion Imager SII (bottom). Reprinted from Burchill et al., 2012 [70].

Table 4.2: Plasma flow velocity (\vec{V}_o) components for different angles (θ) with respect to the boom used in the simulations

Case description	θ	$V_o(m/s)$
1	0°	(0, 985.78, 650.51)
2	45°	(459.98, 985.78, 459.98)
3	60°	(563.36, 985.78, 325.26)
4	90°	(650.51, 985.78, 0.)
5	120°	(563.36, 985.78, -325.26)
6	135°	(459.98, 985.78, -459.98)
7	180°	(0, 985.78, -650.51)

plasma is drifting with the same speed in the upward direction. The effect of the ram velocity on the SII is analyzed by considering different orientations of the plasma flow velocity vector with respect to the boom. The illustration of the velocity angle with respect to the boom is given in Figure 4.3. The angles and the corresponding plasma flow velocity components are given in Table 4.2: For all orientations of the ram velocity considered, PTetra simulations are carried forward in time until a steady state is reached. The time required to reach steady state depends on the size of the simulation domain, the number of particles used in the simulation and the size of the mesh. A smaller simulation domain takes less time than a larger simulation domain. The larger simulation domain considered includes the rocket payload which is used as the electrical ground. The boom is also assumed to be grounded with the spacecraft body and the SII sensor is biased to $-1.9V$ with respect to the boom. In this study, the main focus is on the SII sensor, therefore a truncated geometry is used for simplicity in order to reduce computational time. The simplified geometry consists of a SII sensor fixed at the end of the boom and it does not include the rocket payload. In this case, in order to reproduce the correct sensor potential with respect to the background plasma, a collected current is imposed on the SII sensor, whereas the boom is considered as a reference such that the potential difference between the SII sensor and the boom is $-1.9V$. The imposed collected current is obtained from simulations carried out

in a larger simulation domain, including spacecraft body, and from which the current collected by the sensor, is calculated. It was verified that by imposing this collected current to the sensor, and by imposing a bias voltage of $-1.9V$ between the sensor and the segment of the boom, the correct voltages of the sensor and the boom (ground) with respect to the background plasma were obtained. The simulation results presented in this study are obtained with simplified geometry.

4.3.2 Test particle Modeling

Test-particle modeling have been widely used to study the kinetic properties of a plasma system in space and astrophysics. Two formulations are used here to compute: *a)* the ion velocity distribution functions around the sensor aperture and *b)* the fluxes on the MCP. These are respectively the backward Liouville approach and the forward Liouville approach. A detailed description of these two approaches is given by Marchand, 2010 [74]. Test kinetic modeling is based on Vlasov's equation and Liouville's theorem. We recall that, according to Liouville's theorem, in a collisionless plasma, the single particle velocity distribution function $f(\vec{r}, \vec{v}, t)$ remains constant along the particle trajectories.

Backward Liouville Approach

This formulation makes use of particle backtracking and Liouville's theorem. The backward Liouville approach is used to compute the velocity distribution functions for NO^+ and O_2^+ ion species at 36 points uniformly distributed around the SII aperture. In this approach, a 3D grid with N_v vertices is constructed in velocity space at each point \vec{r} around the sensor aperture. This grid is adaptive and it is based on a balanced octree decomposition of an initially uniform Cartesian mesh. At time t , for a given position \vec{r} and each velocity \vec{v} of the velocity grid, particle trajectories are integrated backward in time. If the trajectory of the particle ends inside the injection or source region, say, at position \vec{r}_o with

velocity \vec{v}_o , the distribution function is computed from $f(\vec{r}_o, \vec{v}_o, t_o) = f(\vec{r}, \vec{v}, t)$, where $f(\vec{r}_o, \vec{v}_o, t_o)$ is the assumed background distribution function. However, if the trajectory of the test-particle does not encounter the injection region, the value of the velocity distribution function is set to be zero. The velocity distribution function at time t is constructed from that at time t_o , by using Liouville's theorem. In this way the distribution function is discretized in 3D velocity space. The velocity distribution functions for both NO^+ and O_2^+ are computed independently.

Forward Liouville Approach

The second formulation makes use of particle tracking forward in time and Liouville's theorem. The NO^+ and O_2^+ velocity distributions calculated around the SII aperture are used to inject and push particles into the sensor. Particles entering the sensor, are deflected by the radial electric field between two hemispheres and they are collected by the MCP array as shown in the Figure 4.2 (bottom). The ion fluxes are computed on 64×64 pixel array. The contribution from each collected particle to the flux on a given pixel, is approximated by $\Gamma = f\vec{v} \cdot \hat{n}$, where f is the interpolated particle velocity distribution function at the aperture entrance and \hat{n} is the unit vector normal to the surface of the SII sensor.

4.3.3 Results and Discussion

In this section, the simulation results describing the effect of plasma flow velocity on the Suprathermal Ion Imager (SII) is presented in the following three steps:

- PTetra simulations are carried out for different orientations of the plasma flow velocity. Representative potential and ion density profiles are illustrated near the sensor.

- The electrostatic potential obtained from PTetra is used to compute the NO^+ and O_2^+ distribution functions at the entrance aperture of SII by using the backward Liouville approach.
- Using the particle distribution functions computed in the previous step, particles are injected in the sensor aperture down to the MCP by using forward Liouville approach. Ion fluxes are compared with rocket based measurements along its downward trajectory at an altitude $150km$.

4.3.4 Electrostatic Sheath and Plasma Density

The steady state electrostatic potential near SII and the potential of the boom are shown in Figure 4.4. The numerical value of the boom potential in this case is $-0.22V$, which is approximately $-4k_B T/e$. Being biased by $-1.9V$ with respect to the boom, the sensor shell potential however, is strongly negative at a voltage of approximately $-2.12V$ with respect to the background plasma. The electrostatic sheath with thickness of order of a few electron Debye length; i.e., $\lambda_{De} = 6.7mm$ is formed around the sensor. The values of the sensor shell potential and the boom potential are also slightly affected by the plasma flow velocity. In the simulations plasma is assumed to be composed of electrons and molecular ions, NO^+ and O_2^+ . The ion composition at an altitude $150km$ shows that the fraction of NO^+ and O_2^+ ions is approximately 57% and 40% respectively. All plasma species have a temperature of $600K$. The thermal velocities $v_{th} = \sqrt{\frac{2k_B T}{m}}$ of NO^+ and O_2^+ are $575m/s$ and $557m/s$ respectively. The plasma drift velocity $v_d = 1180m/s$ is approximately two times greater than the thermal velocities of NO^+ and O_2^+ . This leads to a supersonic flow of plasma with a Mach number $M = 2$ therefore, a wake is observed in the ion density. The structure of the ion density profile is different with different orientations of the plasma flow velocity. As an example, the ion density profiles in planes $X = 0, Y = 0$ and $Z = 0$, for angles $\theta = 0^\circ$ and $\theta = 90^\circ$ are illustrated

in Figure 4.5 and Figure 4.6 respectively. The negative biasing of the sensor results in higher ion density in the vicinity of the sensor with variations at different angles. It is found that for $\theta = 90^\circ$, the ion population in the vicinity of the sensor is higher compared to that at $\theta = 0^\circ$.

4.3.5 Modeling of velocity distribution functions

The computed electrostatic sheath potential profiles surrounding the SII sensor and payload are used to calculate the velocity distribution functions around the SII aperture. The effect of the ram velocity on SII is investigated by comparing the distribution functions obtained for different orientations of the plasma flow velocity vector. For example, the NO^+ distribution functions for the two different angles $\theta = 0^\circ$, and $\theta = 90^\circ$ computed at four locations A, B, C and D around the entrance aperture are shown in Figure 4.7 and 4.8. These points are exposed differently to plasma, which explains the difference in the distribution functions computed at these locations. The plasma flow velocity components for different orientations of the velocity vector are given in Table 4.2. It can be seen that the largest component of the plasma velocity vector is v_y . In all cases, the bottom of the sensor (near point C) is therefore, the most exposed to the plasma flow and the top (near point A) is the least exposed. Plasma flow in the vicinity of points B and D, on the other hand is intermediate between that at points A and C. The comparison between the distribution functions computed for $\theta = 0^\circ$, $\theta = 90^\circ$ and $\theta = -90^\circ$ in Figure 4.7, 4.8 and 4.9 shows some interesting differences. In the spacecraft frame, for $\theta = 0^\circ$ the component of the plasma flow velocity along the axis of the boom is $v_z = 650.51m/s$. For $\theta = 90^\circ$, the component of the plasma flow velocity perpendicular to the payload axis is also perpendicular to the boom and is equal to $v_x = 650.51m/s$. The component of the velocity along the payload axis is $985.78m/s$ in all cases. When plasma flow is along the boom ($\theta = 0^\circ$) the flow velocity is not in the direct field of view of point A and therefore, fewer

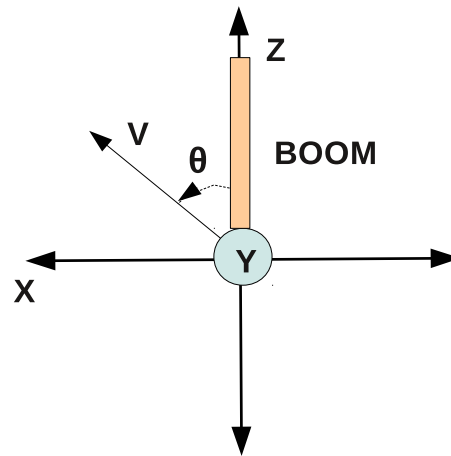


Figure 4.3: Illustration of the angle (θ) between the boom and the plasma flow velocity as seen in the spacecraft rest frame. In this illustration zenith is mainly in the \hat{y} direction.

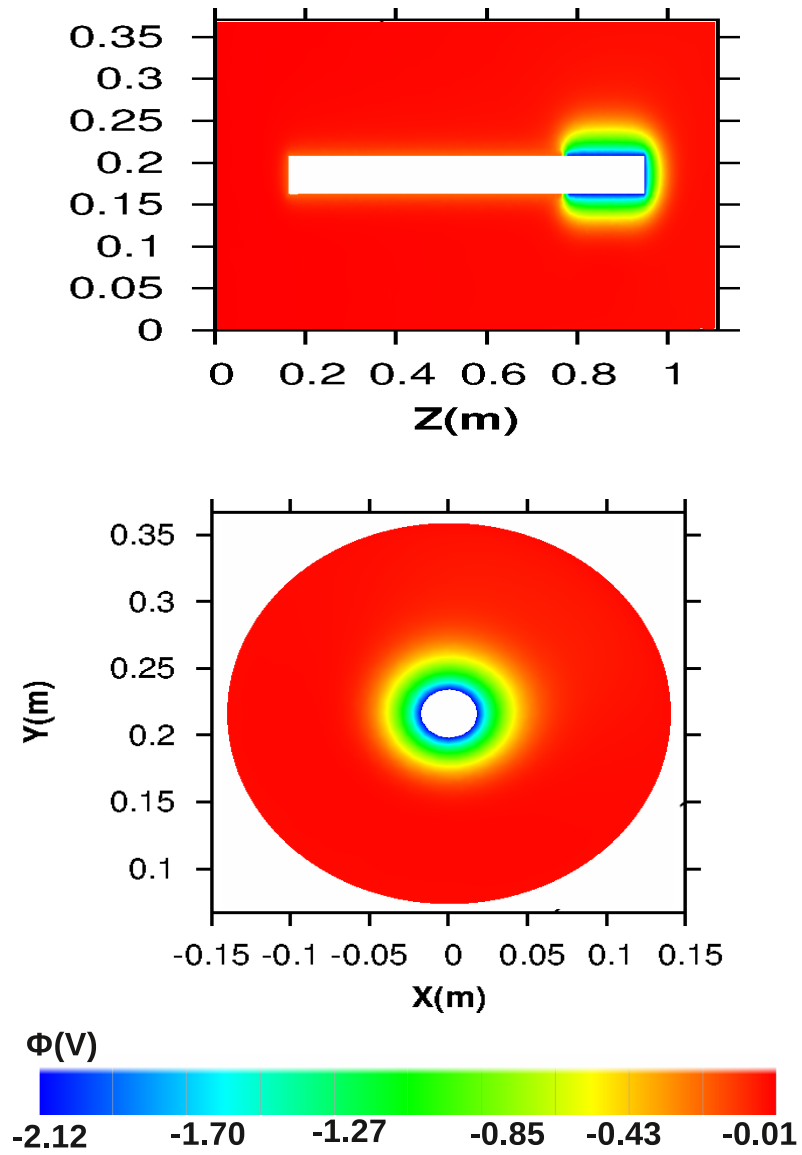


Figure 4.4: Plasma sheath potential profiles in the $X = 0$ (top) and $Z = 0$ (bottom) plane for $\theta = 90^\circ$.

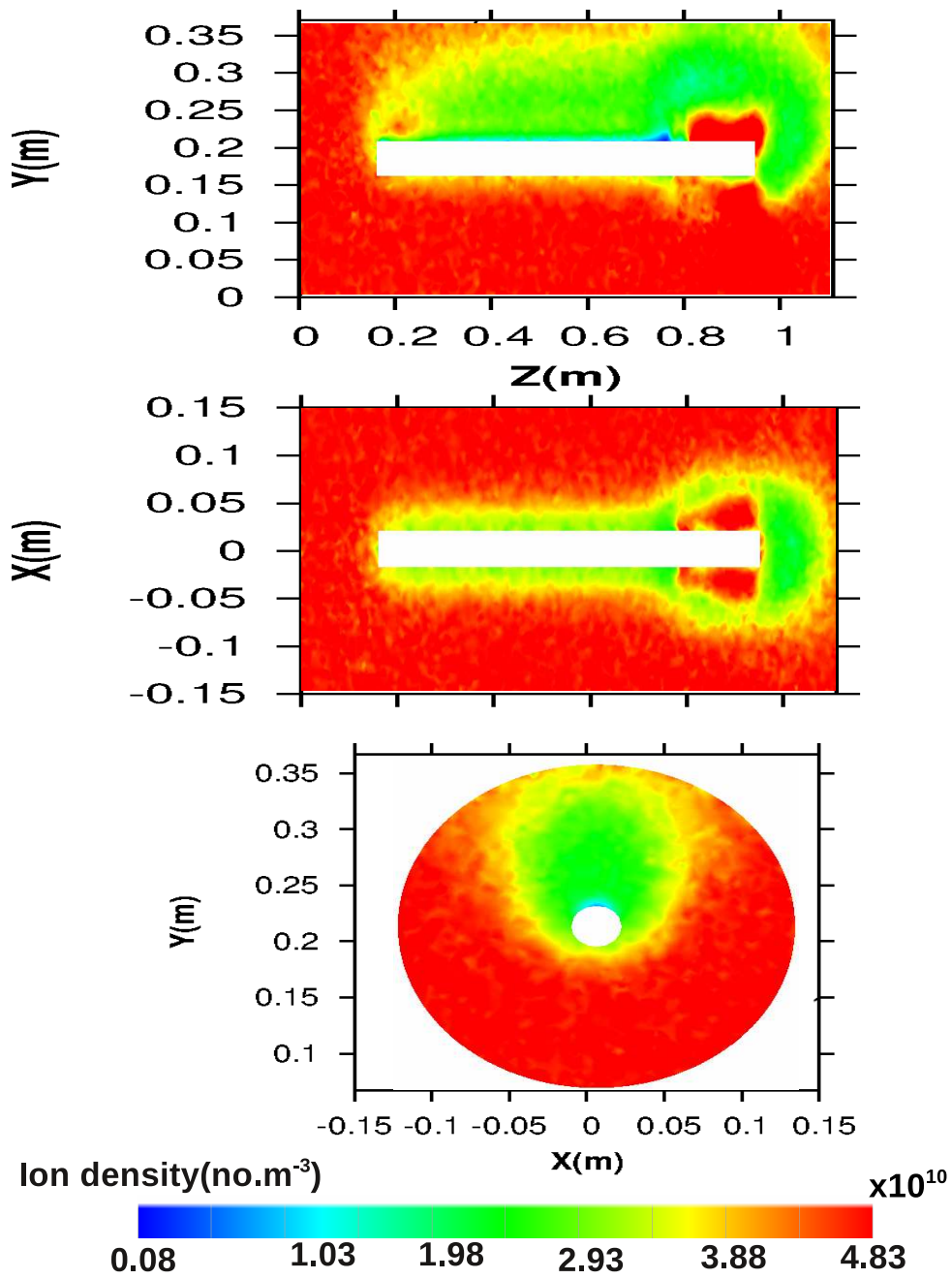


Figure 4.5: Illustration of ion density profile for $\theta = 0^\circ$.

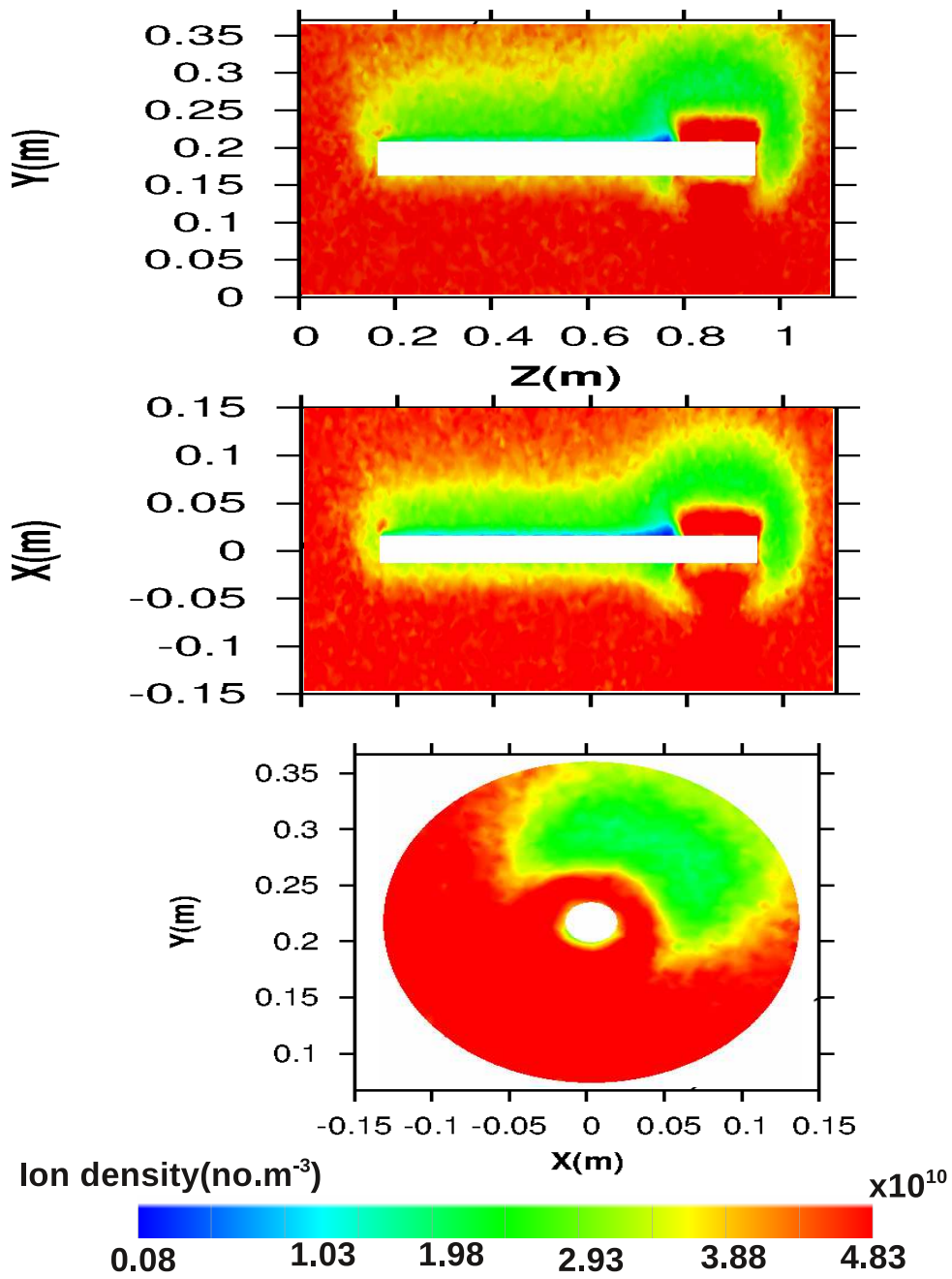


Figure 4.6: Illustration of ion density profile for $\theta = 90^\circ$.

particles reach at point A. In this case, particles reaching point A are the ones that are deflected by the attractive sheath potential. This explains the two components of the velocity distribution function at that point. When $\theta = 90^\circ$, the distribution function at point A also has two components. These however, are not symmetrical as with $\theta = 0^\circ$. This is due to the fact that particles reaching point A from the right have to be deflected more by the attractive sheath than those reaching A from left. This explains the larger extent of the distribution function with positive v_x (for particles deflected from the left) than that with negative v_x (for particles deflected from the right). Now considering point C, the distribution function is seen to be symmetrical with respect to $v_x = 0$ when $\theta = 0$, and shifted toward positive values of v_x . This shift is a direct consequence of the fact that, when $\theta = 90^\circ$, ions incident at C have an average velocity with a positive v_x component. The distribution functions at point B also show differences due to the fact that, when $\theta = 90^\circ$, plasma flow toward B is more direct than when $\theta = 0^\circ$. As a result, more particles will reach B when $\theta = 90^\circ$ than that when $\theta = 0^\circ$. The distribution functions for $\theta = -90^\circ$ are shifted to the left ($-X$) direction compared to the distribution functions obtained for $\theta = 90^\circ$.

4.3.6 Calculation of particle fluxes on the micro channel plate

The computed distribution functions are used to inject particles in the sensor and calculate particle fluxes on the MCP by using the forward Liouville approach. For this purpose a 64×64 pixel array is assumed on the MCP. Simulation results illustrating the ion fluxes on the pixel array are shown in Figure 4.10. In each panel, the net flux is composed of NO^+ and O_2^+ ions; that is, $\Gamma = \Gamma_{NO^+} + \Gamma_{O_2^+}$. The ratio between the masses of the two ion species being 1.07 both ions have nearly identical trajectories. The total ion fluxes on

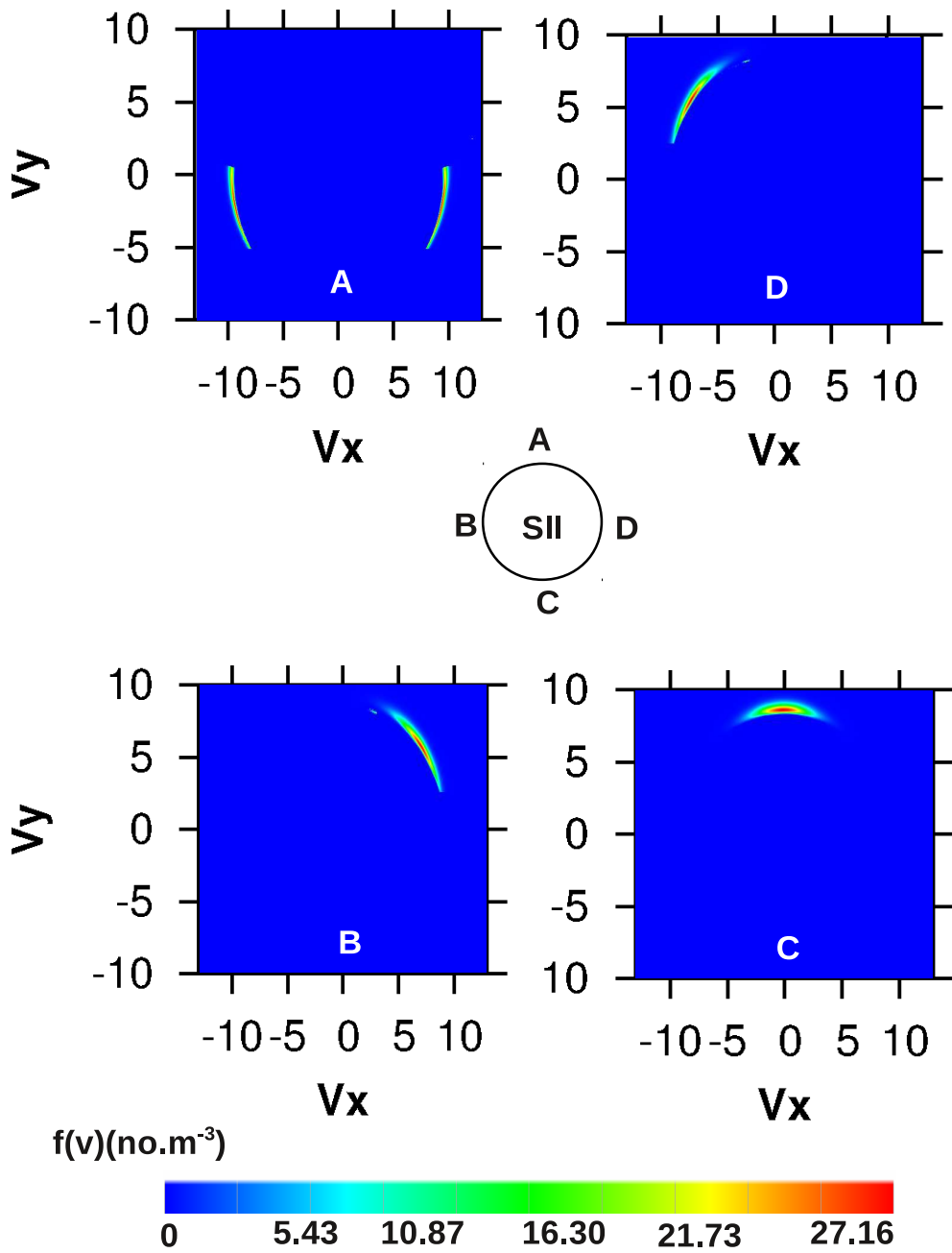


Figure 4.7: Illustration of NO^+ velocity distribution functions in the $v_z = 0$ plane for $\theta = 0^\circ$. Velocities are normalized with respect to the thermal velocity of NO^+ (575m/s).

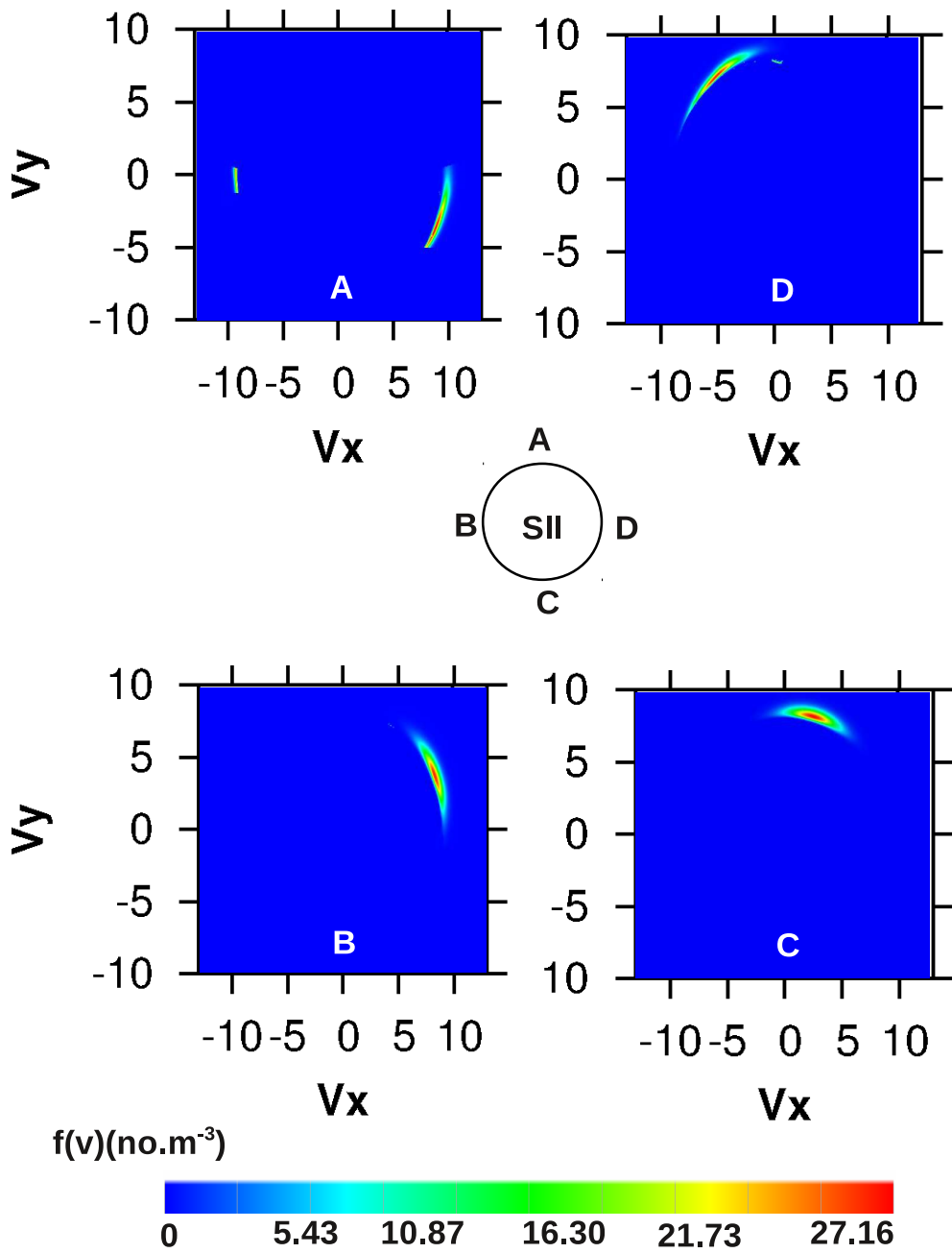


Figure 4.8: Illustration of NO^+ velocity distribution functions in the $v_z = 0$ plane for $\theta = 90^\circ$. Velocities are normalized with respect to the thermal velocity of NO^+ (575 m/s).

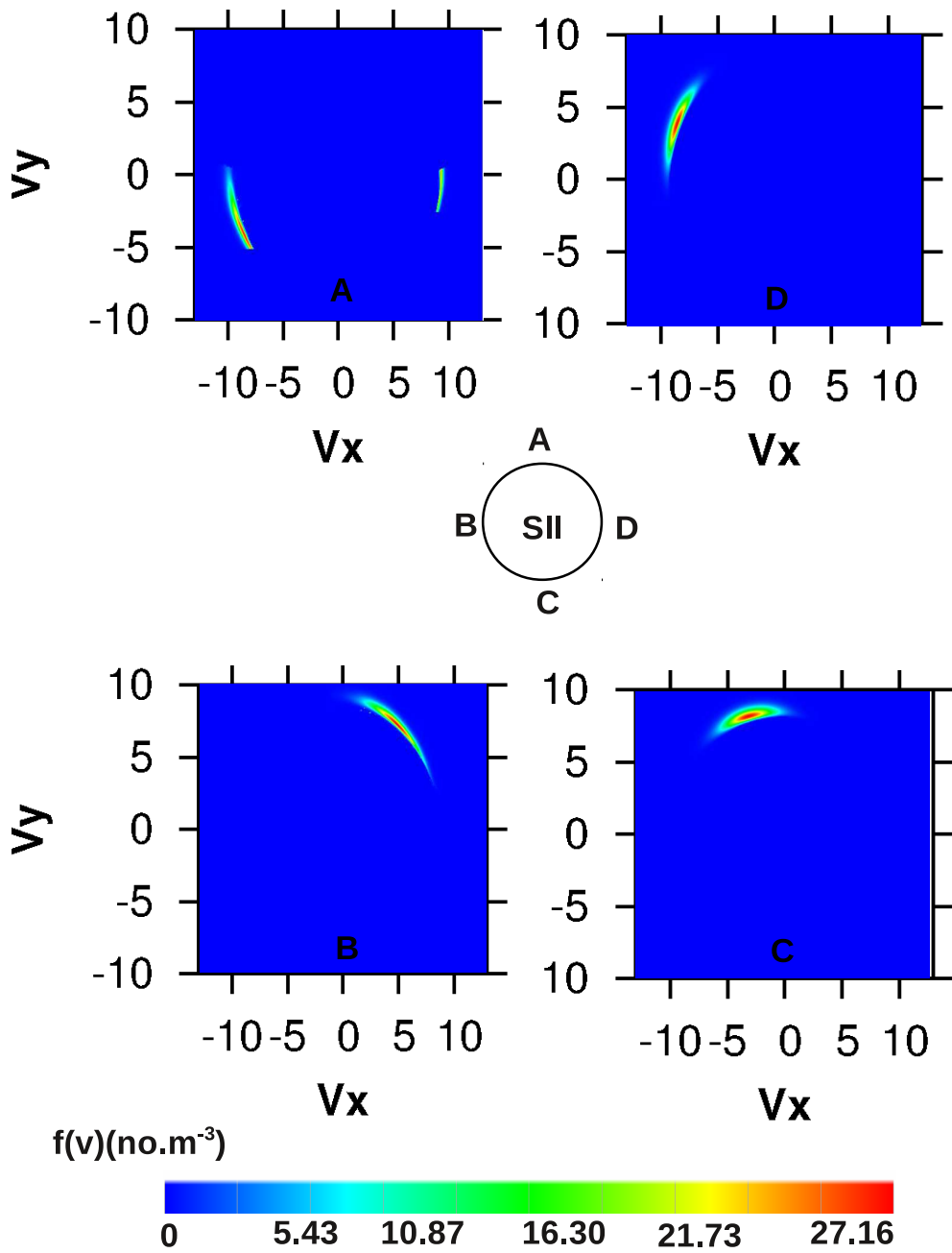


Figure 4.9: Illustration of NO^+ velocity distribution functions in the $v_z = 0$ plane for $\theta = -90^\circ$. Velocities are normalized with respect to the thermal velocity of NO^+ (575m/s).

the MCP show a marked dependence on the orientations of the plasma flow velocity vector as illustrated in Figure 4.11 (top). It is noticed that the peak in the total ion fluxes during the first half of a cycle (from 0° to 180°) occurs at approximately $\theta = 80^\circ$. The simulated ion fluxes in the second half of a cycle (from 180° to 360°) are essentially the mirror images of the ion fluxes obtained in the first half of a cycle (from 0° to 180°). This results in two maxima in the total ion flux per cycle. A plot of the time series of the total SII signal obtained on the MCP during the rocket downward trajectory at approximately 150km is also shown in Figure 4.11 (bottom). It is observed that the signal is periodic with a time period $T = 1.6\text{s}$ with only one peak per spin cycle. This is different from what is predicted by the simulations, where the total flux (integrated over the MCP pixel array) has two maxima per spin cycle. Owing to the different parts of the MCP in which the computed ion fluxes appear, as discussed above, a possible explanation for this difference is that a fraction of pixel array is not responding. Indeed for angles between 0° and 180° , ion fluxes are seen to be centered or shifted to the right of the vertical axis in Figure 4.10. Conversely this distribution is found to be centered or shifted to the left of the vertical, for angles between 180° and 360° . If for example, the detector on the left side of the MCP were damaged and not responding, the total measured flux would decrease as the angle is varied from 180° to 360° , and the calculated maxima in this interval would not be measured experimentally. The hypothesis of a malfunction of a part of the MCP in this flight has already been surmised by [70]. The comparison between our simulation results and the observations tend to confirm this hypothesis. If a malfunction of the detector, corresponding a dead left half of the MCP in Figure 4.10, is taken in to account in the calculations then the simulated fluxes also show one peak per spin cycle as illustrated in Figure 4.12. From the analysis of the spin profiles it is found that the full width at half maximum (FWHM) of the simulated flux profile is qualitatively and quantitatively comparable to that of the time series profile of the measured

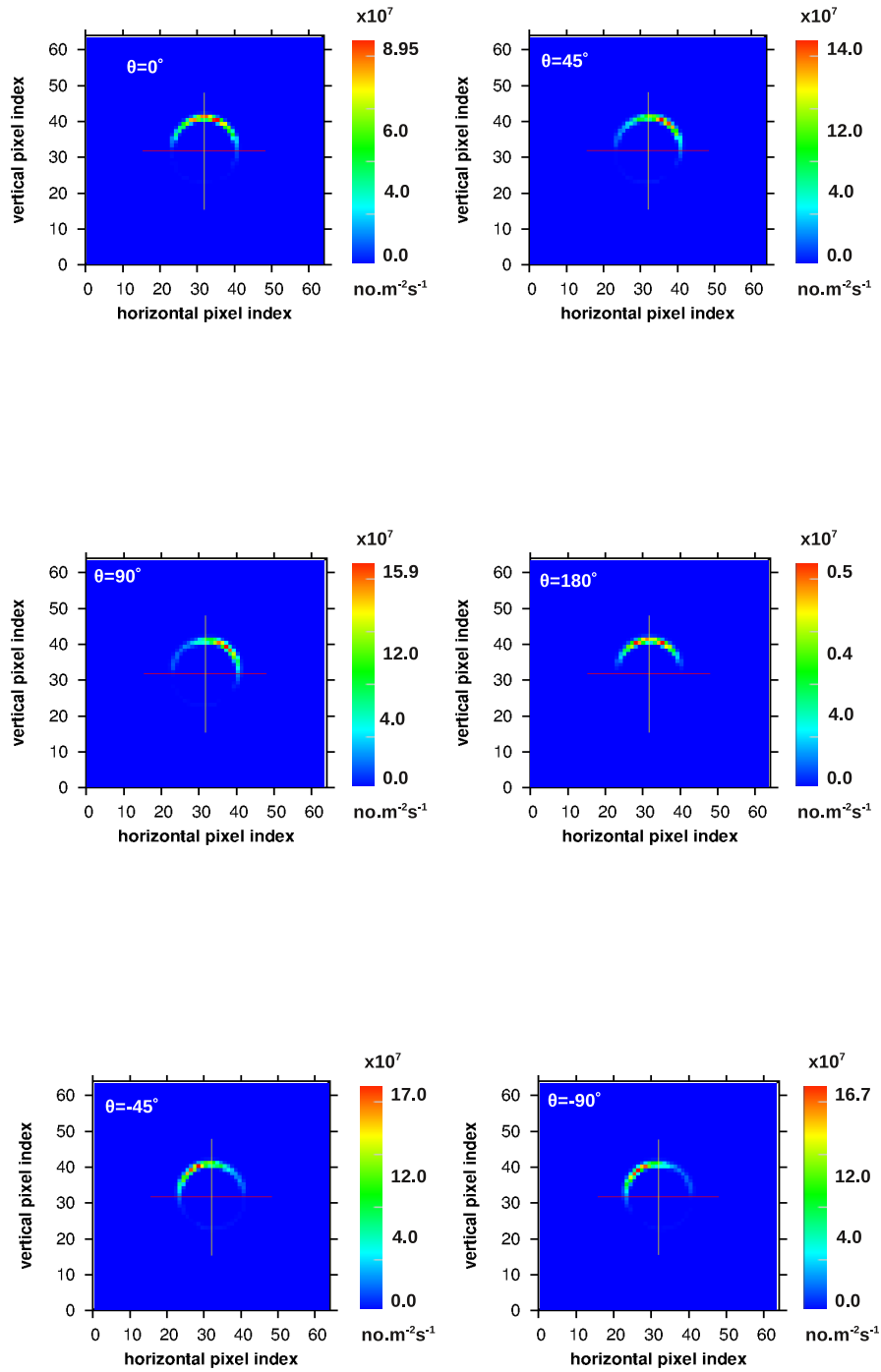


Figure 4.10: Illustration of fluxes on the MCP in the XY plane for various angles θ . Fluxes are shown as seen from the tip of the boom looking in the $-Z$ direction, toward the spacecraft main body.

SII signal.

4.4 Summary

A combination of PIC and Test-particle numerical models are used to compute the ion fluxes on the micro channel plate (MCP) of the Suprathermal Ion Imager (SII), which is part of the scientific payload of the NASA sounding rocket JOULE II. Simulations are carried out to investigate the effect of the plasma flow velocity and the electrostatic sheath on the SII sensor which is biased to $-1.9V$ with respect to the boom. This is achieved in three steps: Firstly, the electrostatic potential around the SII sensor and the potential of the boom are computed using the 3D PIC simulation code PTetra for different plasma flow conditions. Secondly, the effect of the finite electrostatic sheath and the flow velocity on the the distribution functions of NO^+ and O_2^+ ions in the vicinity of the sensor is determined. This is done by computing the O_2^+ and NO^+ ion distribution functions around the sensor aperture, using backtracking and Liouville's theorem. Thirdly, the sensitivity of the net ion flux on the MCP to the angle between the ram velocity and the boom is calculated. This is done by integrating test particle trajectories forward in time, and again using Liouville's theorem for a one-particle distribution function. The computed plasma sheath and the potential of the boom is influenced by the plasma flow velocity. The plasma sheath is found to have a marked influence on the particle velocity distributions. For example, the sheath electric field near the sensor aperture can cause incident particles to be deflected more and enter the sensor at positions far from where they would be incident in the absence of a sheath. Different direction of the background plasma flow velocity with respect to the boom, result in different particle deflections needed to reach at given points around the SII aperture. This in turn leads to different distribution functions as the angle θ between the flow velocity and the boom, is varied. Simulation

results are compared with the NASA sounding rocket Joule II 36.234 based measurements along its downward trajectory at an altitude 150km . The SII time series data shows one peak per spin cycle whereas the simulated total ion fluxes computed on the full MCP array show two peaks. A possible explanation for this discrepancy involves a malfunction of the detectors in part of the MCP, whereby only fluxes incident on part of the array of pixels in the SII sensor would be measured. This would confirm a hypothesis previously made by Burchill et al., 2012 to explain anomalies found in their measurements.

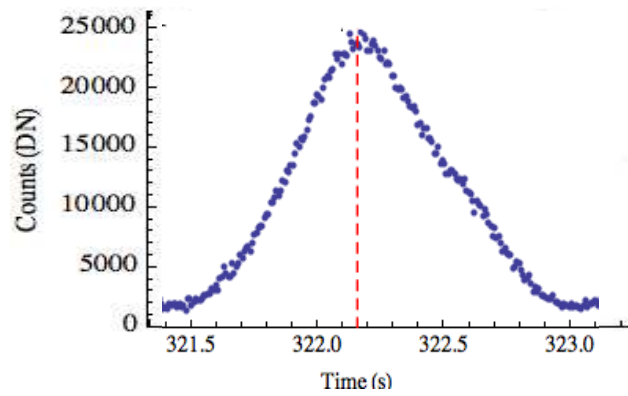
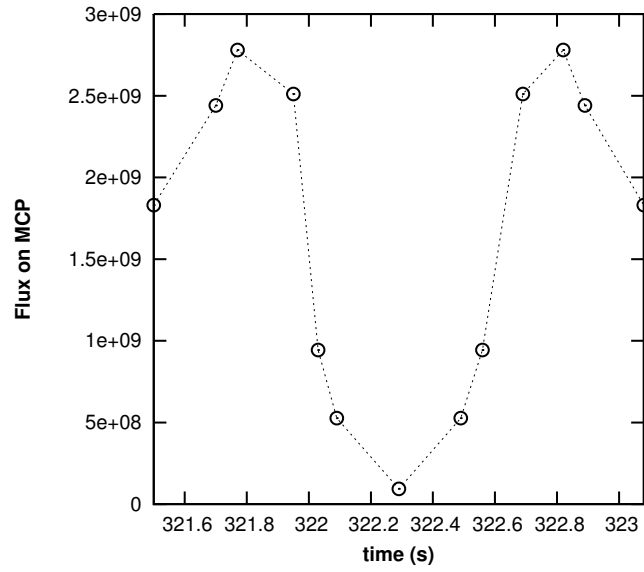


Figure 4.11: Simulation results illustrating the variation in the computed ion fluxes on the MCP as a function of time which is estimated from the spin angle (top). For comparison, the time series plot of Joule II 36.234 total flux at an altitude $150km$ (bottom) is also shown. The vertical red line marked the peak position.

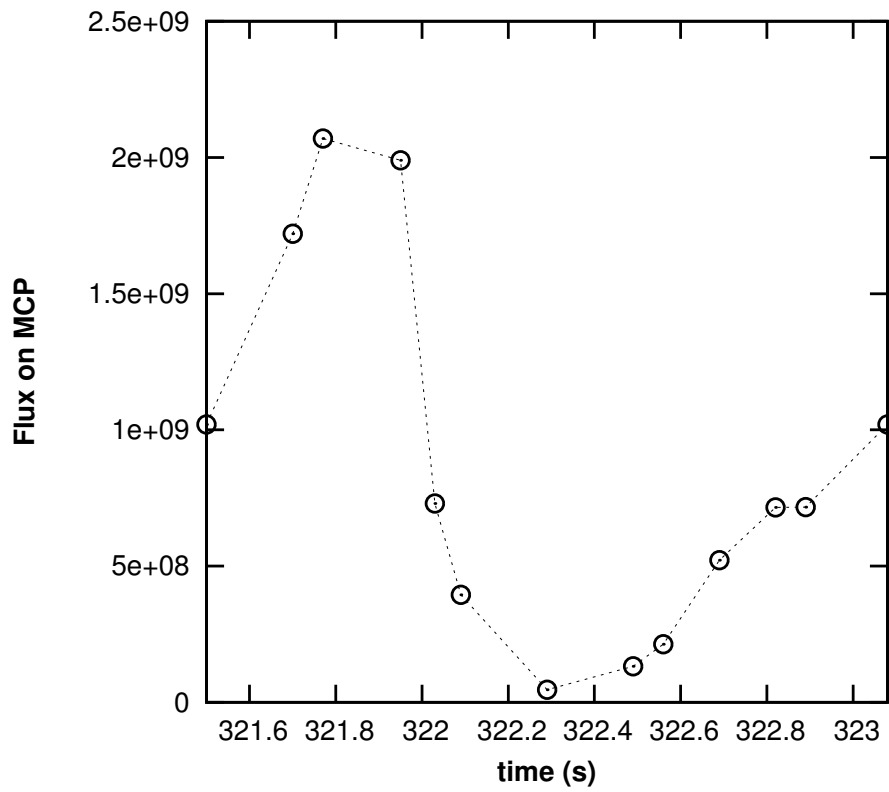


Figure 4.12: Plot of simulated fluxes as a function of the spin time for the right half of the MCP. Here a possible malfunction in the MCP is taken into account.

Chapter 5

Summary and Conclusions

There were two objectives of this thesis. The first was to assess the magnetic field perturbations in the ionosphere in a response to an earthquake. The second objective was to model the ionospheric interaction with particle sensors on board spacecraft. These two objectives were achieved by doing computer modeling and simulations with adapted computer models. In the first part of the thesis, a simple coupled seismo-ionospheric model that accounts for the magnetic field perturbations associated with earthquakes was presented. The model was based on a simple gravity wave model coupled to the 2D mid latitude ionosphere model SAMI2 developed by Huba and Joyce in 2000. Following an earthquake, disturbances in the neutral atmosphere density and velocity associated with gravity waves propagate vertically upward up to ionospheric altitudes 150 – 350 km, where significant coupling between the neutral atmosphere and the ionosphere occurs. As a result, a rapid variation in the ionospheric plasma density and temperature is observed associated with photoionization of the perturbed neutral density. A quantitative assessment of the variation in the electron density is obtained by calculating perturbations in the total electron content (TEC). Strong variations in the TEC are observed close to the epicenter which correspond to large plasma density perturbations in this region associated with the ion acoustic mode. The calculation of magnetic perturbations

was based on a set of linearized MHD equations. These equations were solved numerically by using the finite element code TOPO which was developed by Marchand in 1999. For that purpose TOPO was coupled with the mid latitude ionospheric model SAMI2. The coupling between the two codes accounts for variations in neutral gas density and the collisional drag force between ions and neutrals. Two wave modes are considered: the shear Alfvén mode and the compressional mode. Results of the magnetic field perturbations and of ion velocity perturbations associated with the shear Alfvén and the compressional modes are presented. Variations in the TEC values are also computed for the compressional mode by taking into account the density perturbations transverse to the magnetic field. Results representing TEC perturbations associated with the compressional mode show strong variations at high latitudes both as a function of time and latitude. Calculations presented here are based on a two-dimensional model in which perturbations are assumed to be axisymmetric with respect to the (off-centered and tilted) Earth dipole magnetic field. In particular, the velocity associated with an impulse in the neutral atmosphere is assumed to be purely in the meridional direction in this frame. In an actual seismic event, the neutral impulse would have a finite longitudinal extent, and the impulse would also involve perturbed neutral velocities in the azimuthal direction. Considering that ion velocity perturbations associated with the shear Alfvén mode are in the azimuthal direction, this would then lead to a stronger coupling of the neutral wind with the shear Alfvén mode. The analysis of this effect however, would require a three dimensional model. It can be concluded that the magnitude of ionospheric perturbations depend on the displacement of the ground level during earthquakes. In this study the maximum vertical displacement of the ground level considered is 2cm and the associated perturbations are moderate. On the other hand strong earthquake can lead to the maximum vertical displacement of several meters and therefore, the associated perturbations in the ionosphere would be of stronger.

The second part of this thesis focuses on spacecraft plasma interaction. More specifically this part was devoted to elucidate a number of physical factors that are at play in the interaction between spacecraft particle sensors and ionospheric plasma. These are effects associated with: 1) The electric sheath, 2) ion composition, 3) the magnetic field and 4) plasma flow velocity. These were studied by simulating two kinds of particle sensors: the DEMETER Segmented Langmuir Probe (SLP) and the JouleII Suprathermal Ion Imager (SII). Different plasma conditions were used corresponding to the region of interest in the ionosphere. Simulation results are compared with measurements in order to assess the validity of the models. The Segmented Langmuir probe (SLP) was part of the scientific payload on DEMETER and it was used to measure the electron density and temperature in the ionosphere at an altitude of approximately 700 km. The probe was also used to measure the plasma flow velocity in the satellite frame of reference. It was partitioned into seven collectors: six electrically insulated spherical segments and a Guard electrode (the rest of the sphere). Comparisons were made between model predictions and measurements for actual ionospheric plasma conditions encountered along the satellite orbit. Segment characteristics are computed numerically with PTetra, a three dimensional particle in cell simulation code. PTetra simulation results show different characteristics for the different segments of the probe. The current collected by each segment depends on its orientation with respect to the ram direction, plasma flow, the plasma composition and the orientation of the magnetic field. In a flowing plasma, there was a significant anisotropy in the current collected by probe segments, depending on their orientation with respect to the plasma flow velocity. It was found that the presence of light H^+ ions leads to a significant increase in the ion current branch of the I-V curves for negatively polarized SLP. The effect of the orientation of the magnetic field was demonstrated by varying its direction by a small angle with respect to the reference magnetic field. It was found that the orientation of the magnetic field strongly affects

the electron current branch of the I-V curves of certain segments on the SLP, whereas the ion current branch remains almost unaffected. PTetra simulations were validated by comparing the computed characteristics and their angular anisotropy with DEMETER measurements. Simulation results were found to be in good agreement with measurements. The effect of the ram velocity and the electrostatic sheath on the spacecraft instrument called Suprathermal Ion Imager (SII) was also numerically investigated. The SII sensor was mounted on a $1m$ boom carried by the scientific payload of NASA rocket 36.234 as part of the Joule II mission to investigate the Joule heating in the E-region ionosphere. The rocket flew into quiet auroral conditions above Northern Alaska on 19 January 2007. The payload was spin-stabilized with a spin period of $1.6s$. The SII sensor is an electrostatic analyzer that measures two dimensional slices of the distribution of the kinetic energies and arrival-angles of low energy ions. The study considered the interpretation of data obtained from the SII sensor in particular, the ion temperature measurements. This involved modeling of ion velocity distributions in the vicinity of the SII sensor aperture at an altitudes of approximately $150km$ under different plasma flow conditions. The electrostatic sheath profiles surrounding the SII sensor, boom and payload are calculated numerically with the PIC code PTetra. It was observed that the direction of the ion flow velocity vector modifies the plasma sheath potential profile. This in turn impacts the velocity distributions of NO^+ and O_2^+ ions at the aperture of the particle sensor. The velocity distribution functions at the sensor aperture were calculated by using test-particle modeling. These particle distribution functions were then used to inject particles in the sensor, and calculate the fluxes on the sensor micro channel plate (MCP), from which comparisons with measurements were made. In this case, the simulation results were different from the SII measurements. In particular, simulations predict two peaks in the total ion flux per cycle while, in the experiment only one maximum is observed. An interesting finding of this work is that simulation

results can be reconciled with measurements if part of the MCP is assumed to be non responding; a hypothesis made by Burchill et al., 2012 in a first analysis of the JouleII SII measurements. On the basis of different physical aspects of the ionosphere presented in this thesis, the following conclusions can be made:

- Large scale geophysical phenomena such as earthquakes can cause measurable ionospheric disturbances. These disturbances are associated with plasma velocity, magnetic field and the total electron content. These disturbances can travel to the magnetic conjugate point where they should be measurable.
- Satellites play important role in our everyday life and they are used for communication, Earth observation and basic science. Some of these satellites are low Earth orbit with altitudes up to $2000km$ and some are geosynchronous with orbits at approximately 6.6 Earth radii from the Earth center. They encounter different space plasma conditions which can affect the performance of on board instruments. Computer codes such as PTetra and Test particle simulations are efficient tools that can be used to understand the interaction between spacecraft and space plasma and to interpret sensor measurements. There are several factors that can affect measurements made with sensors on board spacecraft. These include: spacecraft charging, electric sheath, wake, magnetic fields, plasma composition and the flow velocity. A correct and optimal interpretation of in situ measurements requires that these effects be taken into account. Modeling of satellite and instrument interaction with space environment is a powerful tool to get the most value out of the sensitive and very expensive space infrastructure. It is also an essential part in the design and configuration of spacecraft and their instruments.

Bibliography

- [1] <http://astronomyforfun.com/the-northern-lights/>.
- [2] Baumjohann, W. and Treumann, R. A., Basic Space Plasma Physics, Imperial College Press., 1997.
- [3] Forbes, M.J., Palo, E.S., and Zhang, X.,: Variability of the ionosphere, J. Atmos. Solar-Terres. Phys., 1999.
- [4] Gorney, D.J.,: Solar cycle effects on the near-earth space environment, Geophys., Rev. Lett., 28, 315-336, 1990.
- [5] Gurnett, D.A. and Bhattacharjee, A.,: Introduction to Plasma Physics: with space and Laboratory Applications, Cambridge Univ. Press, 2005.
- [6] www.malagabay.wordpress.com/flourescing-sky.
- [7] Imtiaz, N., and Marchand, R.,: Modeling of ionospheric magnetic field perturbations induced by earthquakes, Journal Geophys. Res., 117, 2012.
- [8] Imtiaz, N., Marchand, R., and Lebreton, J.P.,: Modeling of current characteristics of segmented Langmuir probe on DEMETER, Phys. Plasmas, 20, 2013.
- [9] Parks, G., K., Physics of Space Plasmas, Addison-Wesley Publishing Company, 1991.

- [10] Paral, J., Hybrid-Kinetic Modelling of Space Plasma with Application to Mercury, PhD dissertation, 2013.
- [11] www.windows2universe.org/glossary/plasmasphere.html.
- [12] Prolss, W. G., Physics of the Earth's Space Environment, Springer Berlin Heidelberg, New York, 2004.
- [13] Schunk, R. and Nagy, A.F.: Ionospheres Physics, Plasma Physics and Chemistry, Cambridge, 2000.
- [14] Artru, J., Lognonné, P., and Blanc, E.,: Normal modes modeling of post-seismic ionospheric oscillations, Geophys., Res. Lett., 28, 697-700, 2001.
- [15] Astafyeva, I.E. and Afraimovich, E.L.: Long-distance traveling ionospheric disturbances caused by great Sumatra-Andaman earthquake on 26 December 2004, Earth Planet. Sp., 58, 1025-1031, 2006.
- [16] Astafyeva, I.E., Heki, K., Kiryushkin, V., Afraimovich, E.L. and Shalimov, S.: Two-mode long-distance propagation of co-seismic ionosphere disturbances, J. Geophys. Res., 114, A10307, doi: 10.1029/ 2008 JA013853.
- [17] Afraimovich, E.L., Ding F., Kiryushkin, V.V., Astafyeva, E.I.,: Near-field TEC response to the main shock of the 2008 Wenchuan earthquake, Earth, Planet. Space, 62, 899-904, 2010.
- [18] Cailas, E., and Minster J.B.: GPS detection of ionospheric perturbations following the January 17, 1994, Northridge earthquake, Geophys. Res. Lett., 22, 1045-1048, 1995.
- [19] Cailas, E., Haase, J.S., and Minster J.B.: Detection of ionospheric perturbations using dense GPS array in Southern California, Geophys. Res. Lett., 30, doi:10.1029/2003GL017708, 2003.

- [20] Chavez, O., Enriquez, R.P., Cruz-Abeyro, J.A., Millan-Almaraz, J.R., Kotsarenko, A., and Rojas, E.: Detection of electromagnetic anomalies of the three earthquakes in Mexico with an important statistical method, *Nat, Hazard. Earth Syst. Sci.*, 11. 2021 - 2027, 2011.
- [21] Ducic, V., Artru, J., and Lognonné, P.: Ionospheric remote sensing of the Denali earthquake Rayleigh surface waves, *Geophys. Res. Lett.*, 30(18), doi:10.1029/2003GL017812, 2003.
- [22] Garcia, R., Crespon, F., Ducic V., and Lognonne, P.: 3 D ionospheric tomography of post-seismic perturbations produced by the Denali earthquake from GPS data, *Geophys. J. Int.*, 142, 2000.
- [23] Gwal, A.K., Shrivastava, A., and Malhotra, K.: Observation of Seismogenic ultra low frequency electric field fluctuations detected as a burst in the ionosphere during tsunami over Andaman and Nicobar Islands, *Curr. Sci.(India)*, 91, 229-234, 2006.
- [24] Huba J. D., Joyce, G., and Fedder, J.A.: A new low-mid latitude ionosphere model, *J. Geophysical Res.* 105, 2335-2353, 2000.
- [25] Heki K., Ostuka, Y., Choosakal, N., Hemakorn, N., Komolmis, T., and Maruyama, T.: Detection of ruptures of Andaman segments in the 2004 great Sumatra earthquake with co-seismic ionospheric perturbations, *J. Geophysical Res.* 111, B09313 doi:10.1029/2005, JB004202.
- [26] Kiryushkin, V.V. and Afraimovich, E.L.: Determining the parameters of ionospheric perturbation caused by earthquakes using the quasi-optimum algorithm of spatiotemporal processing of TEC measurements, *Earth Planet. Space*, 59, 267-278, 2007.
- [27] Kushwah, V., Singh, V., and Singh, B.: Ultra low frequency (ULF) mag-

- netic field observations at Agra(India) and their association with regional earthquakes, *Phys. Chem. Earth*, 34, 367-372, 2009.
- [28] Krasnov, V. M., Drobzheva, Ya. V., and Lastovika, J.,: Recent advancement and difficulties of infrasonic wave investigation in the ionosphere, *Surveys in Geophys.*, 27, 169 - 209, doi:10.1007/s10712-005-6203-4.
- [29] Krasnov, V. M., Drobzheva, Ya. V., and Chum, J.,: Infrasonic waves in the ionosphere generated by a weak earthquake, *J. Atmos. Sol. Ters. Phys.*, 73, 1930 - 1939, 2011.
- [30] Lognonné, P., Artru, J., Garcia, R., Crepson, F., Ducic, V., Jeansou, E., Occhipinti, G., Helbert J., Moreaux, G., and Godet, P.E.: Ground-based GPS imaging of ionospheric post-seismic signal, *Planet. Space Sci.*, 54, 528-540, 2006.
- [31] Liu, J.Y., Chen, Y.I., Chuo, Y.J., and Tsai, H.F., Ducic, V.: Variation of ionospheric total electron content during Chi-Chi earthquake, *Geophys. Res. Lett.*, 28, 1383-1386, 2001.
- [32] Muto, F., Yoshida M., Horie T., Hayakawa M., Parrot M., and Molchanov O.A.,: Detection of ionospheric perturbations associated with Japanese earthquakes on the basis of reception of LF transmitter signals on the satellite DEMETER, *Nat. Hazards Earth Syst. Sci.*, 8, 135-141, 2008.
- [33] Marchand, R., and Berthelier J.J.,: Simple model for post seismic ionospheric disturbances above an earthquake epicenter and along connecting magnetic field lines, *Nat. Hazards Earth Syst. Sci.*, 8, 1341-1347, 2008.
- [34] Marchand, R., and Simard, M.,: Finite Element modeling of TdeV edge and divertor with EXB drifts, *Nucl. Fusion*, 37, 1997.
- [35] Naaman, Sh.,Alspovich, L.S.,Wdowinski, Sh., Hayakama, M., and Calais, E., : Comparison of simultaneous variations of the ionospheric total elec-

- tron content and geomagnetic field associate with strong earthquakes”,
Nat. Hazards Earth Syst. Sci., 2001, 53-59.
- [36] Nemeč, F.; Santolis, O.; Parrot, M.; and Berthelier, J. J., Spacecraft observation of electromagnetic perturbations connected with seismic activity, *JGR*, **35**, 2008.
- [37] Parrot, M., Berthelier, J.J., Lebreton, J. P., et al.: Examples of unusual ionospheric observations made by the DEMETER satellite over seismic regions, *Phys . Chem. Earth*, 31, 486-495, 2006.
- [38] Rolland, M.L., Lognonné P., and Munekane, H.: Detection and modeling of Rayleigh wave induced patterns in the ionosphere, *J. Geophys. Res.*, 116, doi: 10.1029/2010, 2011.
- [39] Trigunait, A., Parrot, M., Pulinet, S., and Li, F.: Variations of the ionospheric electron density during Bhuj seismic event, *Ann. Geophys.*, 22, 4123-4131, 2004.
- [40] Telesca, L., Lapenna, V., and Hattori, K.: Investigating non-uniform scaling behaviour in Ultra Low Frequency (ULF) earthquake-related geomagnetic signals, *Earth Planet. Sci. Lett.*, 268, 219-224, 2008.
- [41] Saad, Y., and Schultz H., M.: GMRES: Generalized minimal residual algorithm for solving nonsymmetric linear system, *SIAM J. SCI. STAT. COMPUT.*, 7, 1986.
- [42] Zhang, X., Zeren, Z., Parrot, M., Balliston, R., Qian, J., Shen, X.: ULF/VLF ionospheric electric field and plasma perturbations related to Chile earthquakes, *Advanc. Space Res.*, 47, 2010.
- [43] Berthelier, J.J, Godefroy, M., Leblanc, F., Seran, E., Peschard, D., Gilbert, P. and Artru, J.; "IAP, the thermal plasma Analyzer on DEMETER", *Planet. Space Sci.*, **54**, 2006.

- [44] Daz-Cabrera, J. M., Lucena-Polonio, M. V., Palop, J. I., Crespo, R. M., Hernandez, M. A., Tejero-del-Caz, A., and Ballesteros, J. Appl. Phys., **111**, 2012.
- [45] Chen, F.F.; "Langmuir probe measurements in the intense RF field of helicon discharge", Plasma Sources Sci. Technol., **21**, 2012.
- [46] Chung, M. P., Talbot, L., Touryan, K. J.;"Electric probes in stationary and flowing Plasmas: Theory and Applications", Springer-Verlag New York Inc., **11**, 1975.
- [47] www.cubit.sandia.gov/cubitprogram.html
- [48] Engwall, E., Eriksson, A. I., Forest; "Wake formation behind positively charged spacecraft in flowing tenuous plasma", J., Phys. of Plasmas, **13**, 2006.
- [49] Eriksson, A.I., Bostrom, R., Gill, R., Ahlen, L., Jansson, S.E., Wahlund, J.E., Andre, M., Malkki, A., Holtet, J.A., Lybekk, B., Pedersen, A., Blomberg, L.G., Space Sci. Rev., **128**, 2007.
- [50] Hilgers , A., Clucas, S., Thiebault, B., Roussel, J.F.Mateo-Velez, J.C., Forest, J., Rodgers, D.; "Modelling of plasma probe interaction with a PIC code using an unstructured mesh", IEEE Trans. Plasma Sci., **36**, 2008.
- [51] Hoegy, R. W., Brace, H. L.; "Use of Langmuir probe in non Maxwellian space plasmas", Rev. Sci. Instrum., **70**, 1999.
- [52] Hutchinson, I. H.; "Principles of Plasma Diagnostics", Cambridge university press, 1987.
- [53] IGRF Model; <http://www.geomag.bgs.ac.uk/dataservice/modelscompass/igrf.html>.

- [54] Jacobsen , K.S., Pedersen, A., Moen, J.I., Bekkeng, T.A.; "A new Langmuir probe concept for rapid sampling of space plasma electron density", *Meas. Sci. Technol.*, **21**, 2010.
- [55] Laframboise, J.G., UTIAS report N 100, Institute for aerospace studies, University of Toronto, 1966.
- [56] Laframboise , J.G.; Sonmor, L.J.; "Current collection by a positively charge spacecraft: Effects of its magnetic presheath", *J. Geophys. Res.*, **98**, 1993.
- [57] Lebreton , J.P., Stverak, S., Travnicek, P., Maksimovic, M., Klinge, D., Merikallio, S., Lagoutte, D., Poirier, B., Blelly, P.L., Kozacek, Z., Salaquarda, M.; " The ISL Langmuir probe experiment processing on board DEMETER: Scientific objectives, description and first results", *Planet. Space Sci.*, **54**, 2006.
- [58] Marchand, R.,"PTetra, a tool to simulate Low Orbit satellite-plasma interaction", *IEEE Trans. Plasma Sci.*, **40**, 2012.
- [59] Merlino, R.; "Understanding Langmuir probe current-Voltage characteristics", *Am. J. Phys.*, **75**, 2007.
- [60] Meassick, S., and Chan C., *J. Geophys. Res.*, **28**, 1926.
- [61] Mott-Smith, H. M. and Langmuir I., *Phys. Rev.*, **28**, 1926.
- [62] Nagaoka, K.; Hara, K.; Ishihara, T.; Okamoto, A.; Yoshimura, S.; Tanaka, M.Y.; "Plasma flow measurement using directional Langmuir probe under weakly ion magnetized conditions", *J. Phys. Soc. Jpn.*, **70**, 2001.
- [63] Olson, J.; Brenning, N.; Wahlund, J.-E.; Gunell, H.; "On the interpretation of Langmuir probe data inside a spacecraft", *Rev. Sci. Instrum.*, **81**,2010.

- [64] Olson, S. C.; "Ion Flux Maps and Helicon Source Efficiency in the VASIMR VX-100 Experiment using a moving Langmuir probe Array", M.Sc thesis, 2009.
- [65] Piel, A.; Hirt, M.; Steigies, C. T.; "Plasma diagnostics with Langmuir probes in the equatorial ionosphere: The influence of surface contamination", *J. Phys. D.*, **17**, 2001.
- [66] Piel, A.; "Plasma Physics: An introduction to Laboratory, space and fusion plasmas"; Springer-Verlag Berlin Heidelberg, 2010.
- [67] El Saghir A., Shannon, S.; "The impact of Langmuir probe geometries on electron current collection and the integral relation for obtaining electron energy distribution functions", *Plasma Sources Sci. Technol.*, **21**, 2012.
- [68] Seran, E.; Berthelier, J. J.; Saouri, F.Z.; Lebreton, J.P; "The spherical segmented Langmuir probe in a flowing thermal plasma: numerical model of the current collection", *Ann. Geophys.*, **23**, 2005.
- [69] Zhang, J. M.; Hong, L. ; Zhi-Peng, C.; Chen, L.; Jin-Lin, X.; Tao L.; A-Di, L.; Wan-Dong L.; "Usage of displaced current in Langmuir probe measurement", *Chin. Phys. Lett.*, **29**, 2012.
- [70] Burchill, J. K., Clemmon, J. H., Knudsen, D. J., Larsen, M., Nicolls, M.J., Pfaff, R. F., Rowland, D., and Sangalli, L.; High-Latitude E region ionosphere-thermosphere coupling: A comparative study using in situ and incoherent scatter radar observations, *J. Geophys. Res.* **117**, 2012.
- [71] Carlson, C., McFadden, J., Turin, P., Curtis, D., and Magoncelli, A.: The electron and ion plasma experiment for FAST, *Space Sci. Rev.*, **98**, 33-66, 2001.
- [72] Hundhausen, A., Asbridge, J., Bame, S., Gilbert, H., and Strong, I.: High-Latitude E region ionosphere-thermosphere coupling: Vela 3 satellite ob-

- servations of solar wind ions: a preliminary report, *J. Geophys. Res.* **72**, 87-100, 1967.
- [73] Knudsen, D. J., Burchill, J. K., Berg, K., Cameron, T., Enno, G. A., Marcellus, C. G., King, E. P., Wevers, I., King, R. A.: A low-energy charged particle distribution imager with a compact sensor for space applications, *Rev. Sci. Instrum.*, **74**, 202-211, 2003.
- [74] Marchand, R.: Test-particle modeling of space Plasmas, *Commun. Comput. Phys.* **8**, 471-483, 2010.
- [75] Marchand, R., Burchill, J.K., and Knudsen, D.J.: Modeling of Electrostatic Sheath Effects on Swarm Electric Field Instrument Measurements, *Space Sci. Rev.* **156**, 73-87, 2010.
- [76] Ogilvie, K., Chornay, D., Fritzenreiter, R., Hunsaker, F., Keller, J., Lobell, J., Miller, J., Scudder, J., Sittler, J. E. C., Torbert, R., Bodet, D., Needell, G., Lazarus, A., Steinberg, J., Tappan, J., Mavretic, A., and Gergin, E.: SWE, a comprehensive plasma instrument for the wind spacecraft, *Space Sci. Rev.* **71**, 55-77, 1995.
- [77] Olson, J.; Miloch W.; Ratynskaia, S.; Yaroshenko, V.: Potential structure around Cassini spacecraft near the orbit Enceladus, *Phys. of Plasmas*, **17**,2010
- [78] Pfaff, R., Carlson, C., Watzin, J., Everett, D., and Gruner, T.: An overview of the fast auroral snapshot (FAST) satellite, *Space Sci. Rev.* **98**, 1-32, 2001.
- [79] Rehman, S., Burchill, J., Eriksson, A., and Marchand, R.: Earth magnetic field Effects on Swarm Electric Field Instrument, *Planetary and Space Sci.* **73**, 145-150, 2012.

- [80] Sangalli, L., Knudsen, D. J., Larsen, M. F., Zhan, T., Pfaff, R. F., and Rowland, D.,: Rocket-based measurements of ion velocity, neutral wind, and electric field in the collisional transition region of the auroral ionosphere, *J. Geophys. Res.* **114**, 2009.
- [81] Yang, J., Chen, X. -X., Zhou, J.; Xia, S. -H.: Investigation of the influence of wake effect on plasma sheath, *J. of Astronautics*, **31**, 531-535,2010